ADVANCING THERAPEUTICS FOR ANAPLASTIC THYROID CARCINOMA

By

Kensey Nicolle Bergdorf

Dissertation

Submitted to the Faculty of the

Graduate School of Vanderbilt University

in partial fulfillment of the requirements

for the degree of

DOCTOR OF PHILOSOPHY

In

Pharmacology

May 13, 2022

Nashville, Tennessee

Approved:

Barbara Fingleton, PhD

Jeremy Goettel, PhD

Ethan Lee, MD, PhD

Ann Richmond, PhD

Vivian Weiss, MD, PhD

To the patients.

ACKNOWLEDGEMENTS

First and foremost, I have to thank my mom. From a teen mom finishing high school top of your class, a single mother making it through college and medical school, and putting up with a difficult pre-teen in your early career years, you've shown me how to take the hard paths and make my way through. Graduate school has been my hardest path yet, and it only makes me appreciate your tenacity more. Thank you for passing it on and for teaching me how to survive. You took the road less traveled with me, and I think now we can certainly say that it's made the difference for both of us. Love you most.

To my siblings- Blake, Jacob, Raeghan, Isaac, Parker, and Ansley: I know it's not always easy being my little sibs, but you make me so proud and I can't wait to see what each of you accomplishes. Ansley-at 6 years old you kicked cancer's butt before I even had a shot. You were the first to show me what the other side of this research looks like, the patient experience and the impact of therapies beyond numbers and publications. It makes the hard days worth it and allows me to put a little more humanity into every aspect of my research, all because of you A.

Justin- thanks for reminding me not to take life so seriously. I'm so happy to know you're always in my corner and ready to offer laughs and moral support. You also kicked cancer's butt in shorter time than it took me to finish one set of experiments, and you've had some of the best outlooks and life lessons I've ever heard as a result. We managed to pull off the best father-daughter dance the world has ever seen, and yes, I'm crying again.

Josh, your patience with me knows no bounds. I know you are as excited as I am for me to wrap all of this work up. Thank you for listening to me practice random talks, dealing with me pulling all-nighters, making sure I take care of myself, and picking up the slack when I'm in over my head. I'm so happy to call you my husband and appreciate you more than I have words to express!

Nala, Dilly, and Tito: thank you for keeping me company through all-nighters, making me get up in the morning, and being the best therapy pets anyone could ever ask for.

The rest of my family-Mamaw, Papaw Porkey, Papaw Dale, Nana, Papaw Jim, Allison, Earl, and all of the aunts and uncles and cousins-thanks for cheering me on, providing emotional support snacks, and letting me ramble about science at inappropriate times. You keep me curious and push me to be better in so many ways!

Grace, Mary, Lauren, Jackie, Robert, Steven, and the squad- you have gotten me through this. I'm so thankful that COVID pushed our friend group together, and I'm forever grateful for your cheerleading and all of our shenanigans. I can't wait to see what you all do and am so, so proud of you!

My mentors: Vivian Weiss-who would have thought that when I shook your hand at a poster session in August 2018, we would end up here? I knew within two weeks of my rotation that I wouldn't find a better fit for me, and I still stand by that. I have never felt as encouraged, supported, and confident as I am under your mentorship. You are truly stellar and have brought out all of the best parts of me to help me grow as a scientist and person. You are exactly who I hope to be "when I grow up". Thank you, endlessly. Ethan Lee- thank you so much for pushing me. You pushed me into pharmacology, an excellent program that filled out my project perfectly. You pushed me to try new assays and explore side-paths that developed into exciting projects. You have motivated me to think outside of the box and go big, and it has paid off in so many ways. I appreciate you and all of your support so much.

Weiss Lab- Courtney, Matt, Megan, George, and all of the former members: thank you for your support and all of the Strong Work™. I am so eager to see where your projects go and how we can put all of these puzzle pieces together!

To my committee members- Drs. Barbara Fingleton, Jeremy Goettel, and Ann Richmond- thank you for the myriad of feedback and suggestions, the support and encouragement, and always being so responsive! I am so fortunate to have an excellent group of scientists to look up to and have in my corner.

Finally, the reasons I am in graduate school: my dad and Mamaw Gladys. They both passed away in 2015, at a point where I had my head down and was dead set on medical school. Losing them shook me to my core, and I decided to spend the rest of my life doing what made me truly happy-trying to answer questions through research. I am certain I would not be where I am today without their influence, and I miss them every single day. They motivate me to work harder, laugh louder, spread happiness, and make a difference. I hope they're out there laughing at how sappy this is.

I would also like to thank the Vanderbilt Graduate School, the IGP, the pharmacology department, and the University Counseling Center for all of the support throughout my time in graduate school.

This work was made possible by financial support from the National Institutes of Health T32GM007628-42, NCI 5F31C261060-02, NCI R01CA244188, NCI 1K08CA240901-01A1, NIGMS R35GM122516), and the K12 Vanderbilt Clinical Oncology Research Career Development Program NCI K12CA090625. Additional, funding was provided by the American Thyroid Association 2019-0000000090 and American Cancer Society 133934-CSDG-19-216-01-TBG.

TABLE OF CONTENTS

Page

LIST OF TABLES

Table Page

LIST OF FIGURES

Figure Page

General Abbreviations

AA	Activity Area, the area over the dose-response curve
ATC	Anaplastic thyroid carcinoma
BRAFV600E	A common mutation in BRAF that results in constitutive activation
CI	Confidence Interval, the estimated range that the OR falls into
CK8/18	Cytokeratin 8/18, a marker of tumor cells
DAB	Dabrafenib, a BRAFV600E-specific inhibitor
DC	Dendritic cells
FNA	Fine-needle aspiration
(FNA-)PDO	(Fine-needle aspiration) Patient-derived organoid
LN	Lymph node
MAPK	Mitogen activated protein kinase pathway
Mut	Mutant
OR	Odds Ratio, measure of association
PDOX	Patient-derived organoid xenograft
PTC	Papillary thyroid carcinoma
PYR	Pyrvinium, a CK1alpha agonist
RCC	Renal cell carcinoma
SMA	Smooth muscle actin, a marker of fibroblasts
TAMS	Tumor-associated macrophages
TG	Thyroglobulin
TRA	Trametinib, a MEK inhibitor used in combination with dabrafenib
WT	Wildtype

CHAPTER I

INTRODUCTION

1.1. The Thyroid

The thyroid is a butterfly-shaped endocrine gland located at the front of the neck near the collarbones. It is adjacent to the larynx and partially surrounds the trachea. Normally, thyrocytes form follicles that are responsible for iodine uptake via the sodium-iodide symporter (NIS) and creating thyroid hormones by incorporating that iodine into tyrosine residues on thyroglobulin (TG). These thyroid hormones are responsible for regulating metabolism. There are many conditions that affect thyroid function or require a partial or total thyroidectomy, and in those cases synthetic thyroid hormone (levothyroxine) can be used to maintain a functional metabolism.

1.2. Thyroid Cancer

Thyroid cancer is projected to become the 4th leading cancer diagnosis by 2030[1], surpassing colorectal cancer. Incidence has been steadily increasing for the past 50 years, partially due to advances in early detection[2]. Thyroid cancer is three times more likely to occur in women and is the most common cancer in women between 15 and 29[3]. Nearly 45,000 Americans will be diagnosed with thyroid cancer in 2022, and projected care costs for 2030 exceed $3.5 billion for well-differentiated thyroid cancer alone[4]. There are many different histotypes of thyroid cancer, but the focus of this project is on the most common, papillary thyroid carcinoma, and the most deadly, anaplastic thyroid carcinoma.

1.2.1. Papillary Thyroid Carcinoma (PTC)

PTC is the most common subtype of thyroid cancer, accounting for approximately 90% of all cases[2]. It typically presents in the clinic as a nodule that can be felt in the neck but is otherwise asymptomatic. These tumors can occur in patients of any age, though the mean age of diagnosis is approximately 40 years old[5]. A fine-needle aspiration (FNA) can be performed to collect a sample of cells from the mass, allowing for microscopic evaluation and diagnosis. These tumors remain well-differentiated and can range from small and non-invasive to highly aggressive metastatic disease.

1.2.1.1. PTC Pathogenesis

PTCs can arise due to a number of different factors, including radiation, kinase mutations, and as a result of chronic inflammation from Hashimoto's thyroiditis. The 1945 atomic bombing of Hiroshima and Nagasaki and the 1986 Chernobyl nuclear explosion have led radiation to be the only well-defined environmental cause of thyroid cancer[6]. Exposure to radiation above 50mGy may cause intra-chromosomal rearrangements, with RET/PTC rearrangement being the most common found in PTCs[7,8]. Multiple studies have indicated that while the pathogenesis of radiation-induced PTC differs from sporadic PTC, it does not differ in behavior or prognosis[7].

Point mutations in kinases such as the BRAF and RAS proto-oncogenes are common drivers of PTC oncogenesis. BRAFV600E mutations occur in between 30 and 80% of PTCs, depending on the study population, making it the most common driver mutation in PTC[9-11]. Other BRAFV600 mutations may be observed, though over 90% are of the V600E variant[10]. These BRAF mutations lead to constitutive activation of the mitogen-activated kinase (MAPK) pathway, leading to increased proliferation, migration/invasion, and potentially dedifferentiation. RAS mutations can also impact the MAPK pathway. However, the most common variant in PTC, NRAS, preferentially activates the AKT-PI3K pathway to drive oncogenesis, leading to altered behavior compared to MAPK-driven oncogenesis. RAS mutations occur in up to 20% of PTCs, primarily in follicular variant PTC (FVPTC)[10,12,13].

Finally, chronic inflammation from Hashimoto's thyroiditis (HT) can lead to the development of PTCs. However, these tumors tend to be smaller and less invasive than non-HT patients, likely due to the continuous presence of immune cells in the tumor microenvironment and enhanced monitoring due to the HT[14,15]. The majority of PTC are "immune-cold" tumors, making these immune-rich HT-PTCs distinct in both behaviors and outcome. Herein, we include HT-PTCs in our tumor immune microenvironments to serve as internal positive controls for computational immunogenomic studies and immune-related gene expression, but they are not included in other analyses of PTCs due to their distinct characteristics.

1.2.1.2. Treatment and Outcomes

A partial or total thyroidectomy is the recommended course of treatment for PTC, followed by radioiodine therapy (RAI) to target residual disease. These patients require lifelong thyroid hormone replacement with levothyroxine. While radioactive iodine has revolutionized the treatment of the vast majority of PTCs, between 5 and 15% will become resistant to RAI due to loss of the sodium-iodide symporter (NIS)[16]. NIS is a distinct feature of normal, functional thyrocytes, and expression of NIS can be altered by common mutations found in PTC, including BRAF and RAS mutations. When these tumors become RAI-refractory, treatment options are extremely limited and dependent on identification of druggable driver mutations.

The overall five-year survival rate of PTC patients with local and regional RAI-sensitive disease is near 100%[2]. For patients with distant disease that retains RAI-sensitivity, the five-year survival rate is approximately 76%. Finally, for the approximately 20% of patients who experience recurrence and the 10% with metastatic disease[4], both of which tend to be RAI-refractory, the five-year survival rate decreases to below 50%[16].

1.2.2. Anaplastic Thyroid Carcinoma (ATC)

ATC comprises less than 2% of all thyroid cancers, but accounts for over half of all thyroid cancer-related deaths[2]. These exceptionally aggressive tumors can arise over a matter of weeks, and patients present to the clinic with large, rapidly growing masses in their necks. Due to the critical structures adjacent to the thyroid,

patients may experience dysphagia, cough, or dyspnea due to compression. These dedifferentiated tumors are also diagnosed via FNA, and typically occur in patients over 65 years of age[17]. While PTCs are more common in women, ATCs occur at similar rates in both men and women.

1.2.2.1. ATC Pathogenesis

Very little is understood about the pathogenesis of ATC, and their development is a widely debated topic among pathologists and clinicians. Many believe that ATCs arise via one of two mechanisms: as a progression of prior thyroid disease or as *de novo* tumors. The progression model of thyroid cancers can be loosely compared to the classic Vogelgram[18] of colorectal carcinoma, with tumors acquiring stepwise mutations that drive progression to more and more aggressive subtypes, with ATC as the final form. Many believe that primary mutations in RAS and BRAF drive progression to PTC from normal thyroid, and then acquired mutations in TP53, the TERT promoter, and/or portions of the Wnt signaling pathway drive progression to poorly differentiated thyroid carcinoma (PDTC) and then to ATC[19]. This progression model has been disputed, as co-occurrence of PTC and PDTC is exceedingly rare, while there are many documented cases of PTCs with anaplastic inclusions[20]. Regardless of the presence or absence of a PDTC intermediate, it is well-established that PTC may transform into ATC, though the drivers have yet to be completely elucidated. Additionally, ATCs may arise as recurrence of prior disease over 20 years after the prior diagnosis[21]. We currently do not have any methods of determining which tumors will recur or transform, and latency periods can vary drastically. The existence of *de novo* ATC is much more controversial, as many believe it is not due to absence of prior disease, but instead a lack of detection of prior disease. PTC lesions may be microscopic for years prior to diagnosis, and it is reasonable to believe that many may never be detected prior to development of advanced disease.

Approximately 25% of ATCs harbor a BRAFV600E mutation[22] and 10% have mutated RAS[12], likely derived from a prior PTC that has transformed. Forty percent of ATCs carry a mutation in the TERT promoter that extends telomeres to allow for continued division, and between 50 and 80% have loss-of-function mutations in p53[23,24]. While these mutations are often posited as ATC-causing, they do not account for the distinction between PDTCs

and ATCs. Many studies have characterized distinctly increased Wnt/β-catenin signaling in ATCs, often attributed to activating mutations in β-catenin or loss-of-function mutations in parts of the β-catenin destruction complex, such as AXIN1[25,26]. Wnt/β-catenin signaling is associated with stemness, invasion, altered cytokine profiles that impact the tumor microenvironment, and treatment resistance across a number of cancers[27].

1.2.2.2. Treatment and Outcomes

Dabrafenib-trametinib combination therapy was approved by the FDA for ATCs that carry BRAFV600E mutations in 2018[28,29]. Dabrafenib targets the mutant BRAF, and trametinib was added to the therapy regiment to prevent paradoxical MEK activation that is seen with upstream MAPK inhibition. Median overall survival in patients treated with dabrafenib-trametinib therapy was extended to 14.5 months, though only 8% of patients exhibited a complete response to the therapy[29]. There are currently no approved targeted therapies for RAS mutant tumors, as RAS is generally regarded as an "undruggable" target. Therefore, for the ~75% of patients with BRAF-WT disease, treatment is mainly palliative. Paclitaxel, doxorubicin, and radiation may be used to prolong survival and improve quality of life[22]. Some patients are also eligible for resections, though these are not curative. Even with the most aggressive chemotherapeutic, surgical, and radiological interventions, the median survival time of ATC patients is between four and six months. The five-year survival rate is less than 5%[2]. Clinical trials for novel therapeutics in ATC are exceptionally difficult due to the rapid growth of the tumors and the relatively short life expectancy post-diagnosis.

1.2.3. REVIEW: BRAF TESTING IN CYTOPATHOLOGY

1.2.3.1. Summary

BRAF molecular testing is critical across many cancer types, as selective therapeutics are available for those harboring BRAFV600E mutations. When administered to a patient who does not have a tumor with BRAF-mutant disease, these targeted therapeutics have the potential to cause rapid disease progression.

This literature review was published in *Cancer Cytopathology* in January 2020 as a featured article, and the text below is adapted from:

Bergdorf, K., Lee, L., and Weiss, V. (2020). BRAF molecular testing in cytopathology: Implications for diagnosis, prognosis, and targeted therapeutics. *Cancer Cytopathology 128*(1):9-11.

1.2.3.2. Background and Introduction

The epidermal growth factor receptor (EGFR) is a receptor tyrosine kinase that transduces signals from the cell membrane through the mitogen-activated protein kinase (MAPK) phosphorylation cascade to promote global cellular responses including growth, proliferation, survival, and migration[30] (Figure 1.2.1.). Oncogenic activating mutations in core components of the MAPK pathway (RAS, RAF, MEK, and MAPK/ERK proteins) are frequently found in many common human tumors.

BRAF is an 84 kDa serine/threonine kinase consisting of 766 amino acids (RefSeq NM_004333). It is encoded by the v-Raf murine sarcoma viral oncogene homolog B (BRAF) gene, which contains 18 exons and is located on the long arm of chromosome 7 (at 7q34). The catalytic activity of BRAF is regulated by its N-terminal autoinhibitory domain[31]. In response to ligand, activated EGFR shifts the pool of RAS from a GDP-bound (inactive) to GTP-bound (active) state. RAS-GTP binds to the N-terminal autoinhibitory domain of BRAF, thereby freeing its catalytic domain. Activated BRAF phosphorylates MEK, which leads to MAPK/ERK activation and consequent changes in transcription.

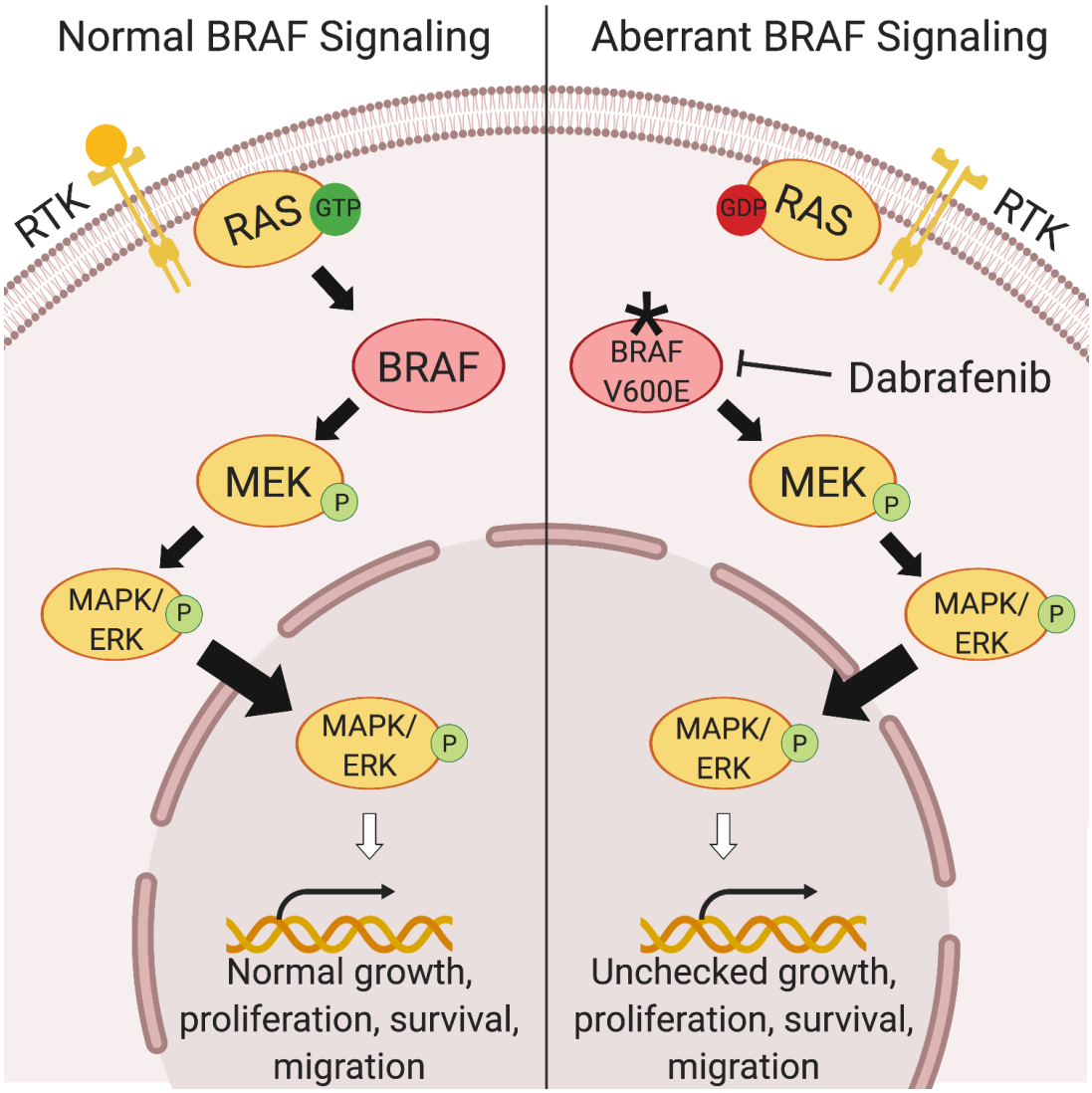

Figure 1.2.1. Schematic of normal and aberrant BRAF signaling

An estimated 80% of mutations in the BRAF gene occur in exon 15 and involve a thymine to adenine transversion at nucleotide 1799 of the BRAF DNA coding sequence (BRAF c.1799T>A)[32]. As a consequence, valine is replaced by glutamic acid at amino acid position 600 (p.Val600Glu or "V600E"). This substitution results in constitutive activation of BRAF and downstream MAPK/ERK signaling, which promotes tumor formation. Other less common BRAF mutations involving different amino acid substitutions at the V600 "hotspot" similarly lead to constitutive BRAF activation[33]. Activating BRAF mutations have been shown to be present in greater than 16% of common human tumors[34]. BRAF V600E is often detected in papillary thyroid carcinoma, with various published studies reporting a frequency between 30-80%. BRAF mutations are found in 59% of all melanomas, 18% of colorectal adenocarcinomas, 11% of gliomas, and up to 4% of non-small cell lung carcinomas[32].

While molecular testing for BRAF is most commonly performed on resection tissue, cytology specimens also represent a rich source of neoplastic cells available for testing. Recent technological advances have allowed for the analysis of increasingly smaller patient samples. Molecular testing can now be routinely performed on a variety of cytologic preparations, including cell blocks, aspirate smears, liquid-based preparations, and needle rinses. Cytology also allows for sampling of unresectable lesions or lesions in critically ill patients. Molecular testing of cytology samples can reveal a tumor's BRAF mutational status relatively early in the course of a patient's care, thereby expediting the diagnosis, prognostication, and use of appropriately targeted therapies. Given the importance of BRAF alterations in cancer, many laboratories offer BRAF molecular testing on cytology specimens, either as an inexpensive and rapid polymerase chain reaction-based assay or as part of a more comprehensive next generation sequencing panel.

1.2.3.3. ***BRAF*** **Mutations in Thyroid Cancer**

The use of molecular diagnostics has revolutionized the management of cytologically indeterminate thyroid nodules in adults. While this testing may be broad in scope (e.g., assessing the presence of mutations in several individual genes, gene fusions, changes in gene expression, copy number variation, etc.), the evaluation of *BRAF* is generally considered a universal requirement and is now a standard part of most molecular diagnostic

testing algorithms for indeterminate lesions. *BRAF* mutational assessment is of particular importance due to its high positive predictive value: the malignancy rate of a thyroid lesion carrying a BRAF mutation is >99%[35]. The vast majority (>95%) of *BRAF* alterations in thyroid lesions are *BRAF* V600E point mutations, occurring mainly in papillary thyroid carcinomas (PTCs), poorly differentiated thyroid carcinomas, and anaplastic thyroid carcinomas (ATCs). Tall cell variants of PTC almost exclusively (>90%) carry this mutation[36-38]. In fact, for malignancy assessment of thyroid lesions, some labs have used a BRAF V600E mutation-specific antibody (VE1) for the detection of mutated BRAF with varying degrees of success[39]. While studies in adults have shown that between 30-80% of PTCs carry this point mutation, pediatric studies report a lower frequency of *BRAF* V600E alterations[40]. Although beyond the scope of this article, additional point mutations and fusions of the *BRAF* gene are also increasingly recognized as being involved in the genesis of thyroid cancers[40].

While some studies suggest that *BRAF* V600E PTCs are more likely to experience disease recurrence[41], most experts agree that the prognostic significance of a *BRAF* alteration in PTC is still unclear. In addition to molecular diagnostics, *BRAF* assessment in ATC is becoming a requirement for treatment decisions. The FDA recently approved combination BRAF/MEK inhibitors (dabfrafenib+trametinib) for *BRAF* V600E ATC, the first potentially effective therapy for this devastating disease[28]. According to the current National Comprehensive Cancer Network (NCCN) guidelines, *BRAF* V600E testing is a now a recommended part of the work-up for ATCs, particularly when metastatic, to determine eligibility for BRAF/MEK inhibitor therapy[42].

1.2.3.4. ***BRAF*** **Mutations in Lung Cancer**

Of all the tumor types described, molecular testing of lung cancer specimens is likely the most widely performed in cytology. With the advent of endobronchial ultrasound guided transbronchial needle aspiration (EBUS-TBNA) and electromagnetic navigational bronchoscopy (ENB), cytology samples and core needle biopsies are becoming the main source of tissue for the initial pathologic diagnosis of lung nodules. While critical for morphologic and immunohistochemical diagnosis, these small samples also provide a rich source of tissue for molecular testing and assessment of eligibility for targeted therapeutics. The current NCCN guidelines require

molecular testing for key mutations and fusions in non-small cell lung carcinoma (NSCLC), including assessment of the *BRAF* gene[43]. Similar to the other tumors described herein, *BRAF* V600E is the most common *BRAF* alteration in NSCLC. Assessment of *BRAF* V600E in NSCLC is important for guiding selection of targeted therapeutics. There is some evidence that *BRAF* mutations may confer resistance to EGFR tyrosine kinase inhibitor therapy[44]; as an alternative, combination BRAF/MEK inhibitors have been successfully used in the treatment of *BRAF* V600E mutant NSCLC[43,45]. Some institutions have used the mutation-specific VE1 antibody for *BRAF* V600E assessment in NSCLC; however, this method is not recommended without sufficient validation[43].

1.2.3.5. *BRAF* Mutations in Melanoma

BRAF mutations are found in approximately 50% of advanced cutaneous melanomas, with 97% of those mutations occurring at the 600th codon[46]. While V600E is the most common point mutation at this position (80%), V600K (15%) and V600R/M/D/G (5%) have also been identified[32]. Although beyond the scope of this article, non-V600 *BRAF* mutations and *BRAF* fusions have also been described at lower frequencies. Of note, uveal melanomas rarely harbor *BRAF* mutations[47]. While primary cutaneous melanomas are not routinely sampled in cytology, metastatic melanoma is commonly diagnosed in dermal and other metastases. According to the current NCCN guidelines, routine testing of *BRAF* is not recommended in primary melanomas for patients without evidence of metastatic disease. However, *BRAF* testing is recommended for patients with Stage III (sentinel lymph node positive) disease who are at high risk of recurrence or Stage IV (metastatic) disease[48]. While the recommendation states that tissue is preferred over cytology for mutational analysis, some patients may not be surgical candidates. Furthermore, testing of the metastatic lesion is usually preferred over archival material, even in cases where the metastatic lesion is only accessible through cytology. BRAF VE1 immunohistochemical staining may be used as a rapid screening test for assessment of *BRAF* V600E mutational status in melanoma, but it requires validation, and confirmatory *BRAF* molecular testing is still recommended[48]. Numerous clinical trials have shown susceptibility of *BRAF* V600 mutant tumors to BRAF and/or MEK inhibitors.

Unfortunately, some patients acquire resistance to single agent BRAF inhibition that likely involves paradoxical activation of MEK[64]. Clinical trials have recently demonstrated the superiority of dabrafenib+trametinib combination treatment[49,50].

1.2.3.6. *BRAF* Mutations in Colorectal Cancer

Currently, formalin-fixed paraffin-embedded resection tissue is the preferred specimen for mutational testing in colorectal cancer (CRC). Mutational testing of cytology specimens in the context of CRC is not well-established and requires additional validation[51]. However, the utility of cytology cell pellets for molecular testing in metastatic colorectal adenocarcinoma has recently been demonstrated[52]. Whether routinely performed on resection tissue, or following validation on cytology specimens, *BRAF* mutational testing of microsatellite instability-high (MSI-H) tumors holds value in differentiating sporadic CRC from Lynch syndrome: the presence of *BRAF* V600E is more consistent with sporadic CRC and precludes the diagnosis of Lynch syndrome in the vast majority of cases[53,54]. While *BRAF* mutations in microsatellite-stable CRC are much rarer (5% vs. 50% in microsatellite-unstable tumors), they have been found to significantly correlate with poor survival (16.7% five-year survival compared to 60% in *BRAF*-wildtype microsatellite-stable CRC)[55].

1.2.3.7. Conclusion

Cytology specimens represent a robust yet often underutilized source of neoplastic cells for genetic testing. As the field of molecular cytopathology advances, an increasing array of molecular tests will be available for ordering and interpretation by cytopathologists. *BRAF* alterations will continue to be staple items on these molecular menus given their prevalence across numerous tumor types and the critical insights they provide into diagnosis, prognosis, and the appropriate use of targeted therapeutics.

1.2.4. Interest in Thyroid Cancer Research

It is apparent that understanding of thyroid cancer, particularly of ATC, is lacking when compared to similar solid tumors. This discrepancy may be attributed to broad success of RAI therapy in PTCs, the perceived

ease of a total thyroidectomy, and/or the rarity of ATC. These factors have contributed to relative obscurity for thyroid cancer research, despite its status as the most common cancer in women between 15 and 29, the second most common solid tumor in children, and the fifth most common cancer overall. This current system has left thousands of patients dependent on levothyroxine for the remainder of their life, with little to no insight into the future prognosis of their disease, likelihood of recurrence, or availability of targeted therapy or personalized medicine should their cancer return. Personalized medicine is rapidly becoming the standard in other aggressive tumors, while ATCs are rarely even sequenced beyond targeted panels to determine BRAF, RAS, TP53, and TERT promoter status.

1.2.5. Thyroid Cancer Model Systems

The lack of general interest and funding for thyroid cancer has contributed to a serious lack of model systems, especially when compared to other prominent tumor types like colorectal cancer, lung cancer, and melanoma. Current model systems for thyroid cancer, and particularly anaplastic thyroid carcinoma, are heavily dependent on cell lines, immunocompromised xenograft models, and genetically modified mice.

While cell lines grown in monolayer culture hold value for preliminary studies, they have many pitfalls. Cell lines represent a nearly homogenous cell population that have been maintained in highly artificial conditions for potentially decades. These conditions, including growth on plastic, can induce transformation of cells and lead to loss of markers that were present in original tumor from which they were derived[56]. This could induce PTC cell line dedifferentiation (i.e., loss expression of thyroglobulin and/or NIS), rendering findings from drug studies and molecular characterization less relevant to in vivo biology. Moreover, growth in monolayer fails to capture the cell-cell interactions that occur within tumors, further altering baseline signaling and potentially cell morphology and behavior.

Xenograft models, in which cancer cell lines are injected into immunocompromised mice, more closely recapitulate some features of patient tumors, but the lack of a tumor-immune microenvironment also limits the

translatability of the data. To address this, immunocompetent genetically modified mice can be used for thyroid cancer studies. These often contain targeted mutations in BRAF, TERT, TP53, and/or RAS. These models are by far the most complete, though mutations may be much more complex in patient tumors. The models are also limited due to the lack of standard sequencing practices in patients, hindering our understanding of mutations behind the most frequent drivers. All of this taken together indicated a significant need for model system development, especially those with enhanced translatability, for papillary and anaplastic thyroid carcinomas.

1.3. Specific Aims

While thyroid cancer incidence is increasing, the need for research into the drivers and therapeutic targets has become more and more apparent. The current lack of information on the pathogenesis and transformation of aggressive thyroid cancers has contributed to a dismal lack of therapeutic options, especially for patients with ATC. The overarching goal of this work is to generate model systems and data to enable the development of targeted therapeutics to improve outcomes for patients diagnosed with aggressive thyroid cancers, including ATCs. I believe that there are multiple unidentified, druggable drivers of thyroid cancer that we are uniquely suited to identify using our patient cohort and novel model systems.

1.3.1. Specific Aim 1: To define molecular and microenvironmental drivers of aggressive thyroid cancers

In order to understand the progression of thyroid cancer from PTC to ATC and what drives aggressive behavior in each, we must first define the mutational landscape, the tumor microenvironment, and the relationship between the two. In this dissertation, I detail how we defined the importance of BRAF status in tumor cell behavior in both monolayer and spheroid cultures. The relationship between BRAF and thyroid cancer cell morphology and behavior had not previously been elucidated, and our work indicates that dabrafenib treatment modifies the actin cytoskeleton to inhibit invasion and growth of BRAF-mutant K1 cells, but not in BRAF-wildtype TPC1 cells. This indicates a potential mechanism of action, which was previously unknown.

We then used computational immunogenomics to define the tumor-immune microenvironment of PTC by stage and metastasis, finding that there are distinct immune cell populations associated with aggressive variants of PTC. These findings prompted the development of two novel thyroid tumor-immune model systems, including an immune-humanized xenograft model and a spheroid-monocyte co-culture system that will be used in future studies.

Finally, using sequencing data of over 300 thyroid lesions, we delineate the presence of increased Wnt ligands driving the increased signaling in ATCs, and do not identify any of the previously described Wnt pathway mutations. This increased signaling, likely driven by both the tumor and the microenvironment, promotes dedifferentiation and may explain a critical feature of transformation between PTC and ATC.

Completion of these studies has advanced the understanding of ATC pathogenesis, PTC behavior, and treatment responses that are dependent on mutational status. They have laid the groundwork for multiple future studies, including further characterization of the thyroid tumor immune microenvironment and therapies targeting Wnt signaling.

1.3.2. Specific Aim 2: Identify targeted therapeutics for anaplastic thyroid carcinoma

As there are currently no broadly effective targeted therapeutics for BRAF-wildtype ATC, it is of great priority to identify any therapeutics that could improve outcomes for patients. To enhance the translatability of our findings, we first had to generate spheroid, organoid, and murine models of anaplastic thyroid carcinoma. We did so successfully and completed an automated high-throughput screen of 1567 drugs to identify potential therapeutic candidates using spheroids, with follow-up verification in organoids. We identified 33 drugs that hold significant promise for development in ATC and three drugs that can be rapidly moved into clinical trials. In fact, we have already been contacted by an oncologist who is proposing a clinical trial based on these data to begin as soon as this summer.

In elucidating the role and importance of Wnt signaling in ATC, we also identified a druggable pathway that could be targeted to inhibit the aggressive features of these tumors. Multiple inhibitors are available for various elements of the Wnt signaling pathway, including receptor antagonists, inhibitors of ligand trafficking, kinase activators, and transcription blockers. While we focus on the kinase agonist pyrvinium that is already FDA-approved as an orphan drug for familial adenomatous polyposis, there are multiple other drugs that hold promise for future development in the treatment of ATC.

1.4. Outline

In this Dissertation, I detail the development of spheroid and patient-derived organoid cultures of papillary and anaplastic thyroid carcinoma and their utilization. In Chapter 2, I discuss the process of developing and refining these cultures. In Chapter 3, I address Aim 1 in characterization of the tumor-immune microenvironment of papillary thyroid carcinoma and Wnt signaling in anaplastic thyroid carcinoma. In Chapter 4, I discuss an agnostic drug screen for anaplastic thyroid carcinoma. Finally, Chapter 5 presents a summary of my work thus far, limitations, and future directions.

CHAPTER II.

DEVELOPING MODEL SYSTEMS OF THYROID CARCINOMA

2.1. DEVELOPMENT OF SPHEROID MODELS OF THYROID CANCER

2.1.1. Summary and Contribution of Study

The aim of this subsection and project was to utilize current thyroid cancer cell lines, both PTC and ATC, to generate spheroid cultures. Two-dimensional (monolayer) cell culture, while accessible and affordable, does not recreate the cell-cell interactions seen in tumors. As such, signaling pathways and cell morphology are modified and study results may be less relevant to what is seen in vivo. To address this concern, we plated eight established thyroid cancer cell lines (4 PTC, 4 ATC) in varying concentrations of Matrigel in low-attachment plates. Together, these conditions allow cells to form three-dimensional structures (spheroids) of varying density, morphology, and size. We show that each spheroid line is unique, and that these cultures are amenable to immunofluorescent staining, small-scale drug studies, and high-throughput screening methodologies. We show that spheroids can respond differently to therapy than the monolayer cultures from which they are derived, indicating the potential role of these cultures in future drug screens and development.

This work was published in *Endocrine-Related Cancer* in February 2020, and text in the chapter is adapted from:

Lee, M., **Bergdorf, K.,** Phifer, C., Jones, C., Byon, S., Sawyer, L., Bauer, J., and Weiss, V. (2020). Novel three-dimensional cultures provide insights into thyroid cancer behavior. *Endocrine-Related Cancer 27*(2): 111-121.

2.1.2. Abstract

Thyroid cancer has the fastest growing incidence of any cancer in the United States, as measured by the number of new cases per year. Despite advances in tissue culture techniques, a robust model for thyroid cancer spheroid culture has yet to be developed. Using eight established thyroid cancer cell lines, we created an efficient and cost-effective 3D culture system that can enhance our understanding of in vivo treatment response. We found that all eight cell lines readily form spheroids in culture with unique morphology, size, and cytoskeletal organization. In addition, we developed a high throughput workflow that allows for drug screening of spheroids. Using this approach, we found that spheroids from K1 and TPC1 cells demonstrate significant differences in their sensitivities to dabrafenib treatment, that closely model expected patient drug response. In addition, K1 spheroids have increased sensitivity to dabrafenib when compared to monolayer K1 cultures. Our study is the first to describe the development of a robust spheroid system from established cultured thyroid cancer cell lines and adaptation to a high throughput format.

2.1.3. Introduction

The incidence of thyroid cancer is increasing at a faster rate than any other cancer in American women. Sixty percent of new cases are in women younger than 55 years of age[57]. Approximately 100 million people in the United States have thyroid nodules, though only up to 15% are estimated to be cancerous[58]. Most thyroid cancers can be successfully treated with resection and radioactive iodine, but tumors recur in 20% of patients and metastasize in approximately 10%[59,60]. For patients with distant metastases, 60% become iodide refractory during the course of their disease, leaving them with limited treatment options[57,61]. In addition, aggressive anaplastic thyroid carcinomas (ATC) can develop from well-differentiated thyroid cancers and represent a deadly disease with an ~4-month overall average survival. Our current culture methods don't account for many in vivo properties of tumors, making them relatively inefficient for developing therapeutics. It is critical to

develop novel thyroid cancer culture methods that more closely mimic patient responses in order to identify therapies that can be used in treatment-resistant disease.

The recently FDA-approved BRAF/MEK inhibitor combination therapy represents a major advancement in care for ATC patients[54]. The BRAF oncogene encodes a component of the MAPK/ERK signaling pathway, which controls growth and cell division[62]. Activating BRAF mutations are common in thyroid cancer, which makes it an attractive drug target. Unfortunately, only 30-40% of BRAF-mutant thyroid cancers respond to the BRAF inhibitor dabrafenib[63]. However, combination BRAF/MEK inhibition leads to increased treatment response in ATC patients[54], likely due to the blockade of paradoxical ERK activation[64]. This treatment is only available for patients with BRAFV600E-mutant tumors, as it may cause disease progression in tumors with wildtype BRAF. Indeed, there are few other effective treatments for aggressive thyroid cancers, despite our knowledge of the important signaling pathways (MAPK, Wnt, PI3K and others) that are critical for tumor development and progression. A near-in vivo culture method that would allow for rapid and facile drug testing across tumors with a heterogeneous mutational background would revolutionize thyroid cancer drug discovery. Significantly, treatment of patient-derived organoids has been shown to closely correspond with patient response to therapy[65]. Development of a cost-effective method for thyroid cancer organoid/spheroid culture that closely recapitulates patient responses may lead to novel therapeutic discoveries for BRAF-wildtype disease.

In this study, we show that eight thyroid cancer cell lines readily form spheroids that represent unique morphology and drug sensitivity. In addition, we find significant differences in the degree of drug sensitivity between the 2D and 3D systems. Our results suggest that 2D culture of thyroid cancer cell lines provides a useful system for uncovering mechanisms of thyroid cancer behavior, whereas the 3D system provides a more accurate platform for translational drug screening.

2.1.4. Materials and Methods

2.1.4.1. Thyroid cancer cell line maintenance

Cell lines were purchased from commercial vendors (K1, Sigma Aldrich; MDA-T32 and MDA-T68 lines, American Type Culture Collection). The TPC-1 line was obtained from Dr. Adel El- Naggar (University of Texas MD Anderson Cancer Center, Houston, Texas). THJ-11T, THJ-16T, THJ-21T, and THJ-29T were obtained from their creator, Dr. John Copland (Mayo Clinic, Jacksonville, FL).

Thyroid cancer cells were authenticated using STRS analysis and were maintained and used experimentally at <20 passages. Cell lines were grown in media containing 10% fetal bovine serum (ThermoFisher Scientific) and RPMI (VWR). Media was also supplemented with 1% penicillin-streptomycin (Sigma), 1X MEM Non-Essential Amino Acid (VWR), and 1 mM sodium pyruvate (Vanderbilt Molecular Biology Resource).

2.1.4.2. Spheroid disc culture

Cells were mixed with 75% Matrigel in complete media containing and 100-300μl drops (discs) were added to each well of a pre-warmed 6-well plate. Plates were incubated for 10 min to allow the Matrigel to solidify. Discs were then covered with warm complete media containing 10% FBS plus B27 supplement (Gibco 17504044). Media was changed every 2-3 days as needed.

2.1.4.3. Semi-solid spheroid culture

Cells were mixed with 5% Matrigel in complete media with 12% FBS. Cells were plated at 8,000 cells/well in 500□L media/Matrigel/FBS + drug in each well of a 24-well ultra-low attachment plate (Corning 3473). Fresh media complete media with 12 %FBS + 5% Matrigel was added drop-wise to the culture once per week.

2.1.4.4. Brightfield and phase contrast microscopy

Brightfield images of spheroids were acquired on a Leica DMi1 inverted microscope with a 4x objective or an EVOS FL inverted microscope with a 20x objective. Phase contrast images were acquired on a Zeiss

Axiophot using an Olympus DP72 camera attachment. The objective was a 20x plan neofluor objective (dry) with a phase 2 condenser.

2.1.4.5. H&E staining

After 8 days in culture, spheroid discs were fixed with 10% formaldehyde + 1% glutaraldehyde (to maintain Matrigel integrity). Discs were then processed and dehydrated in a standard tissue processor and paraffin-embedded. Tissue sections (4um) were stained for hematoxylin and eosin using standard protocols.

2.1.4.6. Monolayer immunofluorescence

Thyroid cancer cells were seeded onto 24-well tissue culture plates (50,000 cells per well) containing coverslips and allowed to attach for 24 hours. Cell were then fixed for 20 minutes with 4% formaldehyde in PBS. If staining for the actin cytoskeleton with phalloidin, 4% formaldehyde in cytoskeleton buffer [10 mM MES pH 6.1, 138 mM KCl, and 2 mM EGTA plus sucrose (0.114 g/ml)] was used. Cells were then washed with 0.1% TBST wash buffer [TBS (20 mM Tris Cl pH7.4 and 150 mM NaCl) containing 0.1% Triton X-100] at RT, permeabilized with 0.5% TBST (TBS containing 0.5% Triton X-100) for 10 min at RT, washed with 0.1% TBST, and incubated for 1 hour at RT in blocking buffer (0.1% TBST plus 2% BSA). Cells were then incubated with mouse anti-tubulin monoclonal antibody (1:1000; Vanderbilt Protein and Antibody Resource; 1mg/ml stock) or mouse anti-β-catenin monoclonal antibody (1:500; Vanderbilt Protein and Antibody Resource; 1mg/ml stock) in blocking buffer overnight at 4˚C. After incubation, cells were washed three times for 20 minutes per wash with 0.1% TBST and incubated with Alexa Fluor 488- or Alexa Fluor 546-conjugated secondary antibodies (Abcam; 1:300) diluted in blocking buffer for 1 hour at RT. For actin staining, Alexa Fluor 568 Phalloidin (1:1000; ThermoFisher Scientific) in PBS was used. Cells were then washed with PBS, incubated with Hoechst in TBS (1:1000; ThermoFisher Scientific) for 5 minutes, and rinsed with PBS before mounting in ProLong Gold Antifade Reagent (Invitrogen). Images were acquired using a CoolSNAP ES camera mounted on a Nikon Eclipse 80i fluorescence microscope with 40x objective.

2.1.4.7. Spheroid immunofluorescence

Spheroids were fixed in 4% formaldehyde in PBS for 30 min at 4˚C then transferred into 2.0 mL tubes, rinsed three times in 0.1% TBST, permeabilized with 0.5% TBST for 30 minutes on a rotator at RT, rinsed with 0.1% TBST, and incubated in blocking buffer for 1 hour on a rotator at RT. Spheroids were then incubated with mouse anti-β-catenin antibody (1:500, Vanderbilt Protein and Antibody Resource) or rabbit anti-E-cadherin antibody (1:200, Cell Signaling Technology) in blocking buffer overnight on a rotator at 4˚C. After incubation, spheroids were washed three times for 30 minutes per wash in 0.1% TBST and incubated 2-3 hours on a rotator at RT with Cy3-conjugated anti-mouse secondary antibody (1:500, Jackson Immune) or Cy3-conjugated anti-rabbit secondary antibody (1:500, Abcam) diluted in blocking buffer. Spheroids were rinsed in 0.1% TBST then incubated with Alexa Fluor 568 Phalloidin (1:1000; ThermoFisher Scientific) and Hoescht (1:1000) in 0.1% TBST for 20 minutes on a rotator at RT. Spheroids were rinsed 1X in 0.1% TBST. Spheroids were put into 1X PBS (Vanderbilt Molecular Biology Resource) then mounted on microscope slides with ProLong Gold Antifade Reagent (Invitrogen). Images were acquired using a Nikon Spinning Disk microscope with Andor DU-897 EMCCD camera with 561 nm and 405 nm lasers. Images were processed using ImageJ.

2.1.4.8. High throughput analysis of K1 and TPC1 cells and spheroids

Utilizing the high-throughput equipment in the Vanderbilt High-Throughput Screening (HTS) Core Facility, K1 and TPC1 cells were resuspended at a concentration of 9500 cells/mL in complete RPMI (2D culture) or complete RPMI supplemented with 2% Matrigel (3D culture). 30µL of cell suspension was plated per well in black 384-well cell culture microplates in the absence or presence of a cell-repellant surface (Greiner Bio-One). Cells were allowed to attach for 24 hours prior to treatment with dabrafenib or DMSO (vehicle) in RPMI. Following 72 hours of treatment, wells were imaged using an ImageXpress Micro XL automated high-content microscope (Molecular Devices). To assess viability, CellTiter-Glo 3D (Promega) was added to wells and mixed with the Bravo liquid handler (Velocity 11/Agilent). Per the CellTiter-Glo protocol, plates were placed on a shaker for 25 min before luminescence was quantified using a Synergy NEO (BioTek multi-mode plate reader).

2.1.4.9. Statistical analysis

Statistical analyses were performed using Fisher's exact test. A value of $p<0.05$ is considered statistically significant. Data for 384-well dabrafenib viability studies were analyzed using Prism 8 (GraphPad Software, Inc). To determine significance, a two-way ANOVA was performed and followed with a Sidak multiple comparisons test.

2.1.5. Results

2.1.5.1. Staining for microtubules, actin, and β-catenin shows distinct patterns in the different thyroid cancer cell lines.

For our studies, we chose eight thyroid cancer lines [papillary thyroid cancer (PTC) cell lines: K1, MDA-T32, MDA-T68, and TPC1; and ATC cell lines: THJ-11T, THJ-16T, THJ-21T, and THJ-29T] with known driver mutations (Table 2.1.1.). Brightfield images show that these lines exhibit varying morphology (Figure 2.1.1). For example, the K1 and THJ-16T cells grow in a flat, epitheliod pattern, while the MDA-T68 cells have an elongated, spindle-like morphology. The thyroid cell lines also vary in both overall cell size and nuclear:cytoplasmic ratios. Microtubule immunostaining revealed differences in their distribution among cell lines, with K1, TPC1, and THJ-16T having prominent Golgi-derived microtubules that fan out into the cytoplasm. In contrast, MDA-T32 and MDA-T68 cell lines show prominent microtubule bundles that traverse the length of the cells (Figure 2.1.1). Actin staining revealed two distinctive morphologies: cells with prominent actin stress fibers (TPC1, MDA-T32, MDA-T68, THJ-11T, and THJ-21T) and cells with enriched lamellipodial actin (K1, THJ-16T, THJ-29T). In addition, THJ-29T cells show actin-enriched ring structures reminiscent of podosomes, which are implicated in cell migration and invasion[66]. Thus, the differences in cytoskeleton organization between thyroid cancer cell lines may be indicative of varying capacity to migrate, form three-dimensional structures, and invade. We then immunostained for β-catenin, which is part of the E-cadherin complex and is also a critical mediator of the oncogenic Wnt pathway in the nucleus[67]. We found that all of the thyroid cancer cell lines contain cytoplasmic

β-catenin. The K1 and MDA-T32 lines, however, show significant staining for nuclear β-catenin, suggesting ongoing Wnt signaling in those cell lines.

Table 2.1.1. Thyroid cancer cell lines used in this study and associated driver mutations.

Cell Line	Driver Mutations
K1	BRAFV600E, PI3K
TPC-1	RET/PTC fusion
MDA-T32	BRAFV600E, TERT promoter
MDA-T68	RAS
THJ-11T	KRAS, TERT promoter, TP53
THJ-16T	PI3K, TERT promoter, TP53, MKRN1-BRAF fusion
THJ-21T	BRAFV600E, TERT promoter, TP53
THJ-29T	TERT promoter, TP53

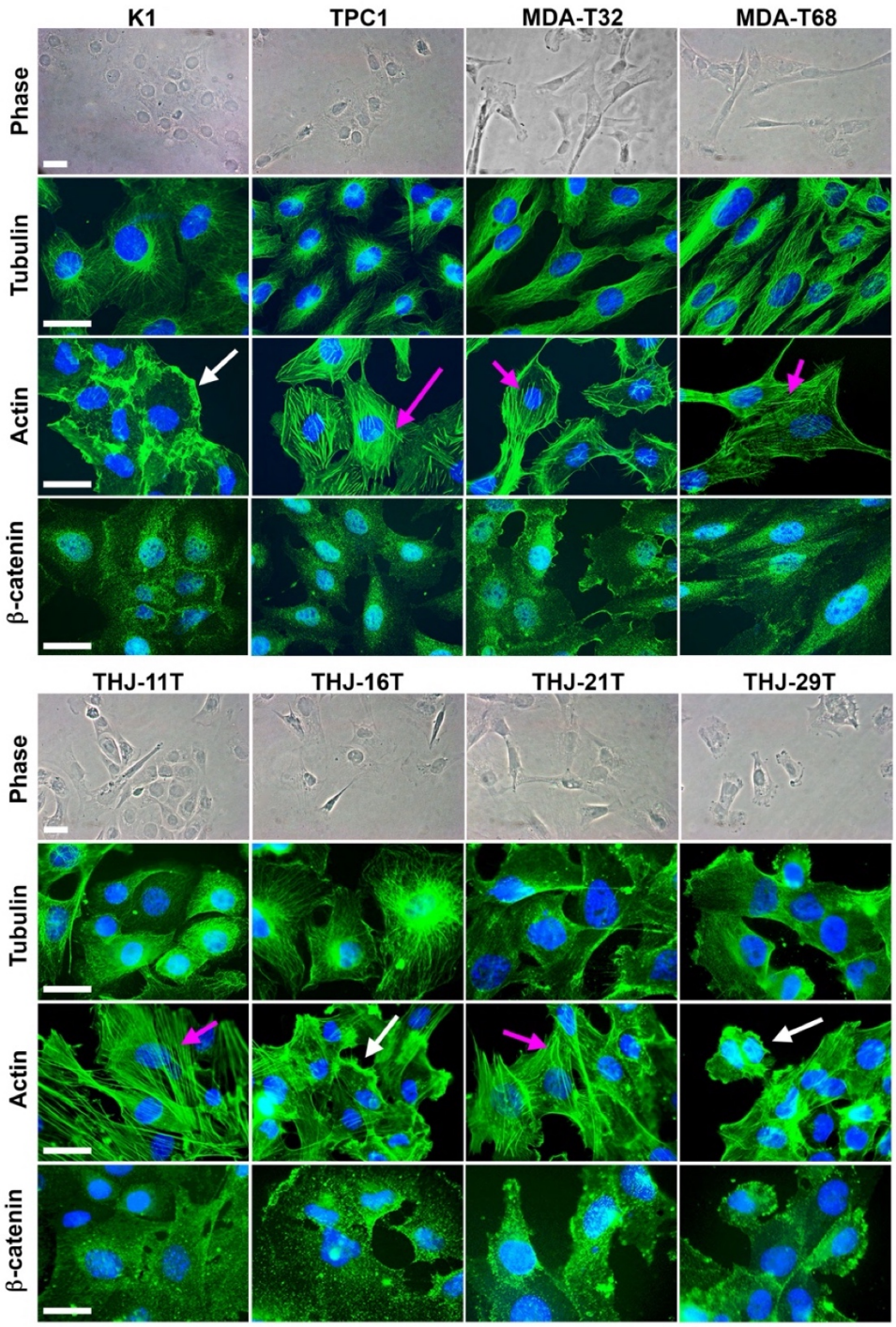

Figure 2.1.1. Characterization of eight genetically distinct thyroid cancer cell lines shows varying morphology and staining patterns for microtubules, actin, and β-catenin. Thyroid cancer cells were grown on glass coverslips, fixed, and stained with phalloidin (for filamentous actin), anti-tubulin antibody, or anti-β-catenin antibody. Top panels show phase contrast. Tubulin staining (green) shows distinct Golgi microtubules in some of the thyroid cancer lines, whereas other lines show long microtubule cables running along the length of the cells. Actin staining (green) reveals cell lines with either lamellipodial (white arrows) or stress fiber predominant patterns (pink arrows). Nuclear β-catenin (green) is observed in many cell lines, suggesting active Wnt signaling. DNA is shown by DAPI (blue). Scale bar is 20 microns.

2.1.5.2. Thyroid cancer cell lines uniformly form spheroids in culture.

Spheroids and organoids are three-dimensional, self-organizing multicellular structures that mimic the complex organization and function of tissues and organs[68]. These culture methods provide a promising new in vitro method to study cancer progression and drug sensitivity, allowing for personalized treatment approaches[69]. With the overall goal of a 3D cell culture system, we sought to grow spheroids from the eight established thyroid cancer cell lines. As these cell lines each have unique genetic features, we aimed to generate a diverse cohort of thyroid cancer spheroids to serve as the first step in drug development and screening. We found that all of the cell lines readily formed spheroids in culture (Figure 2.1.2.). Spheroid morphology and size differed dramatically between the differed thyroid cancer cell lines. Brightfield imaging and H&E staining showed that some spheroids form robust macro-follicular structures, including K1, THJ-11T, and THJ-16T. Other cell lines, such as MDA-T32 and MDA-T68, grow in a microfollicular arrangements that more closely mimic a follicular variant histologic pattern. TPC1, THJ-21T, and THJ-29T formed spheroids, but demonstrated a more invasive and loosely cohesive architecture. E-cadherin staining in the spheroids also showed varying intensity (Figure 2.1.2.). Loss of E-cadherin is a hallmark of epithelial to mesenchymal transition, which is postulated to be critical for cancer progression[44]. Increased cytoplasmic β-catenin has been associated with decreased E-cadherin expression, and may represent increased Wnt signaling, a feature of more aggressive thyroid tumors[71,72]. Alternatively, loss of E-cadherin could release associated β-catenin, thereby increasing its cytoplasmic levels. β-catenin staining in all eight spheroids confirmed that E-cadherin staining is inversely correlated with the level of β-catenin (Figure 2.1.2.). The K1, THJ-11T, and THJ-16T cells exhibited prominent E-cadherin staining but showed low levels of β-catenin. In contrast, TPC1, THJ-21T, and THJ-29T spheroids showed elevated levels of β-catenin and lower levels of E-cadherin staining throughout the spheroids, consistent with their more infiltrative morphology. Of note, the cell lines with high β-catenin levels in 2D culture showed lower levels of β-catenin when grown in a spheroid format, potentially reflecting differences between a 2D and 3D tumor microenvironment.

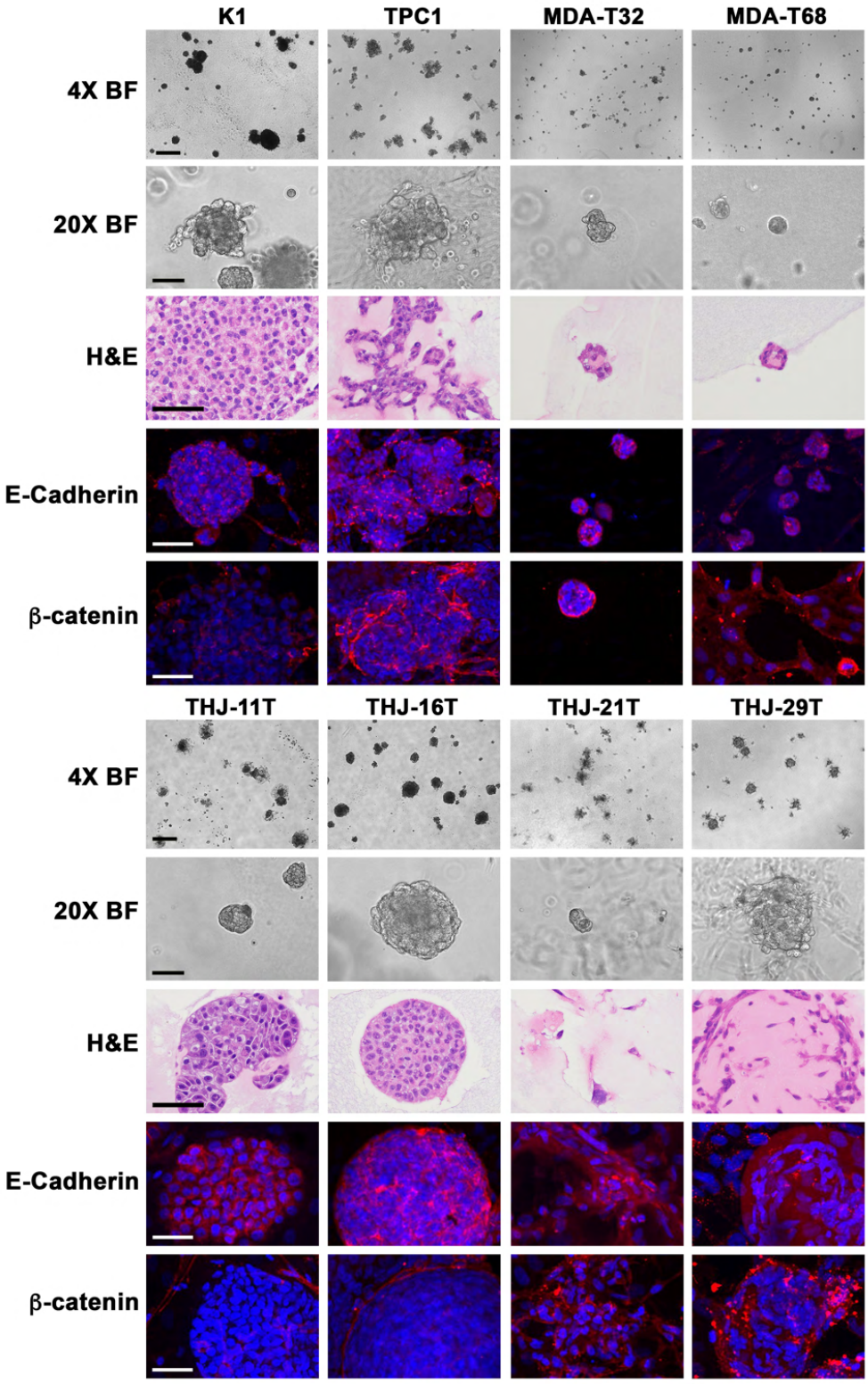

Figure 2.1.2. Thyroid cancer cell lines readily form spheroids that differ in morphology, β-catenin and E-cadherin expression. Thyroid cancer cells were grown in Matrigel discs, fixed, and stained with anti-E-cadherin antibody or anti-β-catenin antibody. Top panels show low and high magnification brightfield (BF) images. Hematoxylin and eosin (H&E) staining of organoid cultures highlights differences in spheroid morphology. For most thyroid cancer spheroid lines, E-cadherin staining intensity inversely correlated with the intensity of β-catenin staining. E-cadherin and β-catenin are red. DNA is blue. Scale bar is 100 □m except for 4X BF (400um).

2.1.5.3. Response of thyroid cancer spheroids to dabrafenib treatment mimics patient response.

The recent development of organoid and spheroid culture provides a near in vivo system that more accurately captures the behavior of a tumor in response to treatment[65,73]. We therefore assessed whether thyroid cancer spheroids respond to treatment with the BRAF inhibitor dabrafenib in a manner similar to patient responses. We first examined the effect of dabrafenib on the morphology of the BRAFV600E-mutant and BRAF-wild-type thyroid cancer spheroids. We found that 48 hour dabrafenib treatment had the most dramatic effect on spheroids from the papillary thyroid carcinoma (PTC) K1 cell line, which harbors an activating BRAFV600E mutation and a PI3K mutation (Figure 2.1.3.). K1 spheroids were much smaller when grown in the presence of dabrafenib. Of note, the more aggressive BRAFV600E-mutant PTC MDA-T32 cell line, which also carries a TERT promoter mutation, showed limited response to dabrafenib. Similarly, the aggressive BRAFV600E-mutant ATC cell line (THJ-21T), which also harbors TERT promoter and TP53 mutations, also showed limited response to dabrafenib. The remaining cell lines, which are BRAF-wildtype, did not show response to dabrafenib. It is not surprising that the more aggressive BRAFV600E-mutant thyroid cancers, with TERT promoter mutations, were less susceptible to dabrafenib therapy alone[74,75]. Clinical trials have shown limited response of aggressive BRAFV600E-mutant thyroid cancers to dabrafenib therapy alone. Prolonged treatment of K1 and TPC1 spheroids with dabrafenib furthered the robust drug effects. As shown in Figure 2.1.3, K1 spheroids exposed to dabrafenib for eight days were dramatically smaller than vehicle treated controls. In contrast, BRAF-wildtype TPC1 spheroids showed a significant increase in spheroid size. This finding is consistent with clinical findings, as BRAF-wildtype tumors often show rapid progression when treated with BRAF inhibitors. While the mechanism of this robust cancer progression following dabrafenib therapy is unknown, we observed a highly significant and robust increase in the mitotic index for TPC1 cells grown in dabrafenib for 48 hours. Evaluation of the mitotic index for K1 cells when grown for two days with dabrafenib showed only a slight increase.

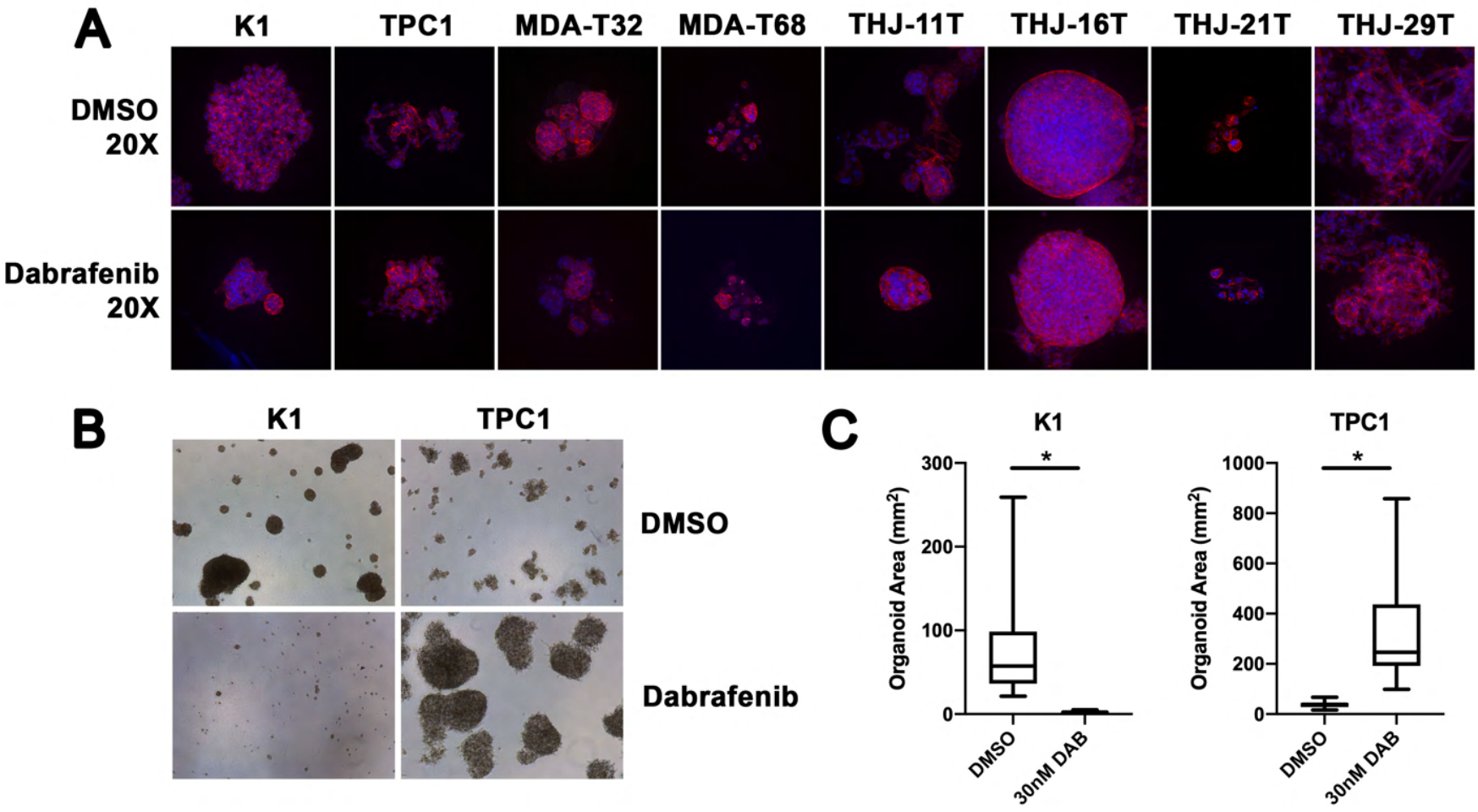

Figure 2.1.3. Effect of dabrafenib, a BRAF inhibitor, on spheroid size. A. Thyroid cancer cell spheroids were treated with 30nM dabrafenib for 48 hours, stained for actin (phalloidin), and imaged using a spinning disk confocal microscope. 20X images do not show a dramatic change in morphology or size with the exception of K1, which show a significant decrease in size. B. Brightfield images of K1 and TPC1 spheroids grown with vehicle or 30nM dabrafenib for eight days reveal long term effects on spheroid size. C. Analysis of organoid size (area in mm2) following treatment with vehicle (DMSO) or 30nM dabrafenib for 8 days demonstrates significantly decreased K1 organoid size and significantly increased TPC1 organoid size with dabrafenib (*p<0.0001).

2.1.5.4. Establishment of a high throughput thyroid cancer spheroid assay for drug screening

The advantages of screening for drug sensitivity using 2D cultures include the ability to rapidly test a large number of conditions and concentrations, the ability to use cells with defined genetic lesions, and the availability of a large number of cell lines for testing. However, cancer cells grown on a flat surface respond very differently to drugs when compared to the original tumor from which they are derived. As such, we sought to adapt 3D thyroid cancer spheroid culture methods to an automated high throughput 384-well format. High throughput screening provides the opportunity for rapid, replicable collection of data for many drugs. The use of the Agilent Bravo automated pipette allows drugs to be added to 384 wells at once, or to be stamped in for creation of replicates. To further the ability of this system, all work was done in clear-bottom plates. This enabled imaging with the ImageXpress Micro XL, an automated high-content imager, which aided in confirmation of findings from our viability assay. We were also able to observe any phenotypic changes in the spheroids following drug exposure. We found that both K1 and TPC1 spheroids could be adapted to the HTS format with minimal modifications, and we could obtain growth inhibition curves for their sensitivity to dabrafenib (Figure 2.1.4.). K1 spheroids were more sensitive to dabrafenib than monolayer K1 cells (EC50 = 0.8nM and 1.8nM, respectively). Neither TPC1 spheroids nor monolayer cells were inhibited by dabrafenib.

2.1.5.5. Dabrafenib treatment shows differential effects on the actin cytoskeleton of the BRAF and RAS mutant cells lines, K1 and TPC1

Given our findings that there are differences in the morphology and actin skeleton of various thyroid cancer lines and the variable response of thyroid cancers to dabrafenib treatment, we sought to determine whether dabrafenib sensitivity could be associated with changes in the actin cytoskeleton. Using immunostaining, we found that treatment of K1 cells with dabrafenib induces shift from a primarily lamellipodial actin phenotype to a stress fiber phenotype with no observable peripheral actin staining (Figure 2.1.5.A, B). Significantly, these changes can be readily observed within an hour of dabrafenib treatment. In untreated TPC1 cells, the majority contain prominent stress fibers with observable peripheral actin staining (mixed phenotype

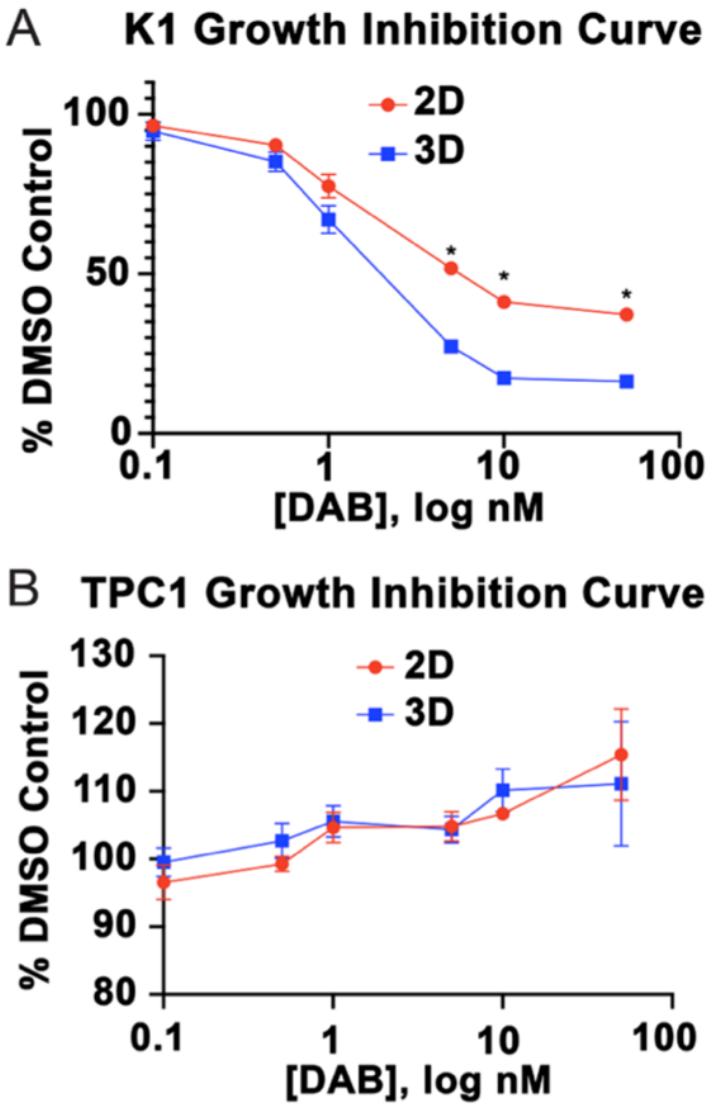

Figure 2.1.4. Thyroid cancer spheroid culture can be readily adapted for high throughput drug screening. K1 and TPC1 cells were seeded onto a 384-well plate for monolayer or spheroid culture and exposed to varying concentrations of dabrafenib. Viability was assessed after 72 hours. A. K1 spheroids were significantly more sensitive to dabrafenib treatment than monolayer K1 cells (*$p<0.0001$). B. In contrast, dabrafenib showed no significant effect on the growth of TPC1 cells in both monolayer culture and as spheroids ($p=0.8749$).

Figure 2.1.5.C, D). TPC1 cells treated with dabrafenib still primarily exhibited a mixed phenotype, but there was a significant decrease in the percent of cells staining for only stress fibers and a subsequent increase in cells staining in the lamellipodial pattern. These results suggest that the effect of dabrafenib on the actin cytoskeleton occurs rapidly, prior to alterations in gene transcription, and is therefore likely via a direct mechanism. Furthermore, the opposite effects of dabrafenib on the actin cytoskeleton of K1 cells (BRAFV600E mutant) and TPC1 cells (RET-PTC fusion) is consistent with the opposite effect of dabrafenib on thyroid cancers with mutations in BRAFV600E versus other driver alterations.

Although dabrafenib had a noticeably dramatic effect on the actin cytoskeleton of K1 and TPC1 cells grown in monolayer culture, the effect in the spheroids was much subtler (Figure 2.1.5.E). Taken together, these data indicate that the effects of dabrafenib on cell-cell interaction and organization were more readily assessed in the thyroid spheroid cultures, while the effects of dabrafenib on the individual cells within the spheroids were less obvious than in the 2D system.

2.1.5.6. Dabrafenib-induced changes in the actin cytoskeleton of K1 and TPC1 cells parallels changes in their migration rates

Because lamellipodial actin is associated with enhanced cell motility[76] we examined whether the dabrafenib-induced changes observed in the actin cytoskeleton of K1 and TPC1 cells affected their ability to migrate. An in vitro scratch assay is a well-established, straightforward method to measure cell migration on a flat surface[77]. We found that treatment of K1 cells with dabrafenib significantly reduced their migratory rates (Figure 2.1.6.A, B). In contrast, dabrafenib promoted the migration of TPC1 cells into the scratched area. These results are consistent with our actin staining data, as dabrafenib induces the a less migratory stress fiber phenotype in K1 cells and a more motile lamellipodial phenotype for TPC1 cells.

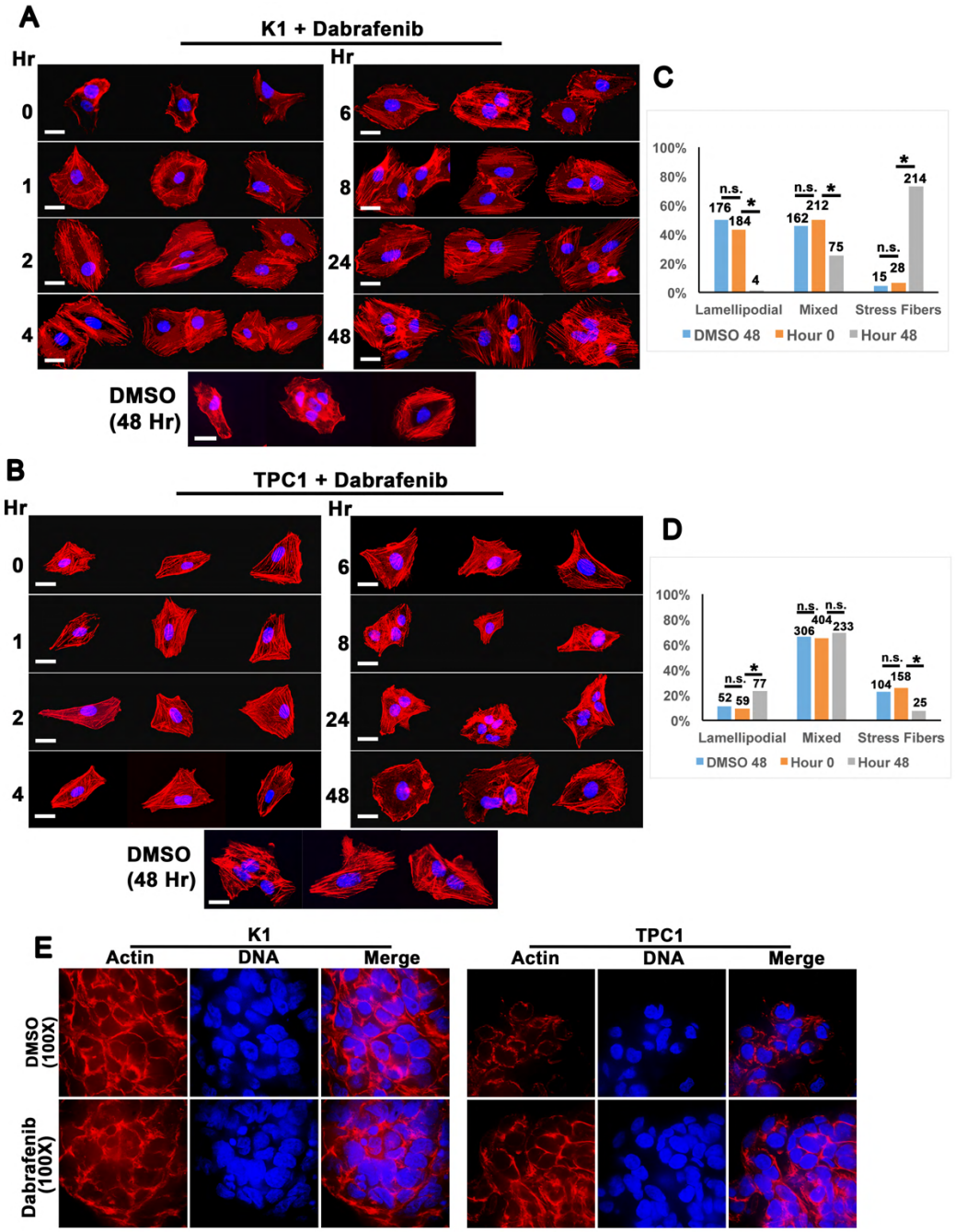

Figure 2.1.5. BRAF inhibition induces changes in actin phenotype of two thyroid cancer lines. A. K1 ($BRAF^{V600E}$ mutant) cells were treated with 30 nM dabrafenib, fixed at the indicated time, and stained for actin (red) and DNA (DAPI; blue). Cells show a predominantly lamellipodial phenotype, with actin enriched in the leading edge of the cell in the absence of dabrafenib. Following dabrafenib treatment, the actin cytoskeleton is converted to a primarily stress fiber phenotype that exhibits little to no observable peripheral actin. B. TPC1 (RET-PTC fusion) cells in the absence of dabrafenib show a predominantly mixed phenotype with both stress fibers and peripheral actin. The percentage of cells with predominantly lamellipodial actin increases with dabrafenib treatment. Each panel contains three representative cell images from three independent replicates. Scale bar is 20 μm. C,D. Quantification of the number of K1 and TPC1 cells with predominantly lamellipodial, mixed, or predominantly stress fiber phenotypes prior to and after 48 hour dabrafenib treatment. The number of cells scored is indicated for each phenotype and condition. N.s. non-significant, *$p<0.0001$. E. Confocal imaging reveals a subtle effect of dabrafenib on the actin cytoskeleton of K1 and TPC1 cells, even at 100X magnification.

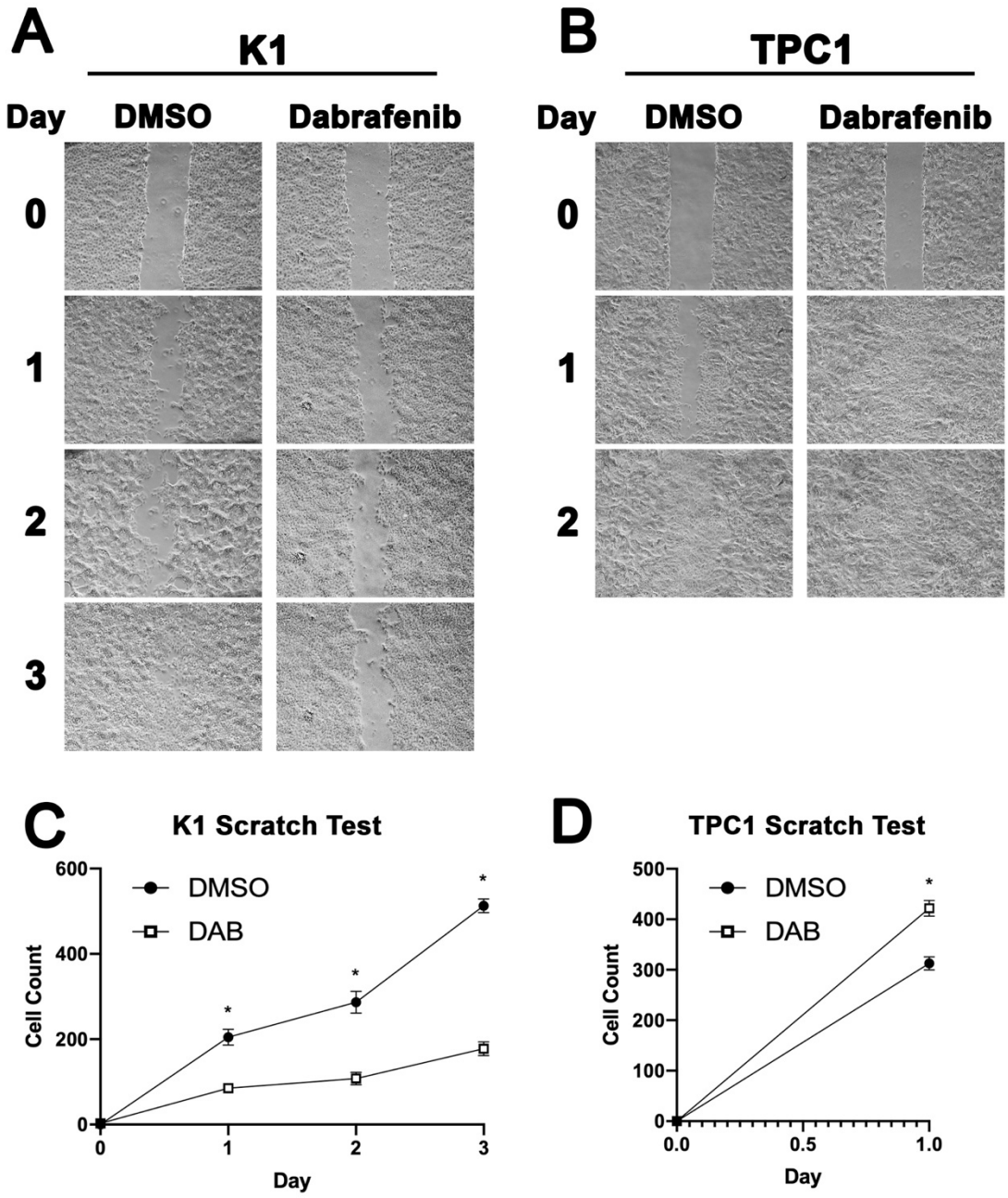

Figure 2.1.6. Changes in the capacity of K1 and TPC1 cells to migrate in a scratch assay upon BRAF inhibitor treatment parallel changes in their actin cytoskeleton. Scratches were made across the bottom of dishes of confluent A,C. K1 and B,D. TPC1 cells treated with vehicle (DMSO) or 30nMdabrafenib, and brightfield images of the scratch were obtained at the indicated times. Quantification of cell migration was performed by counting the number of cells migrated into the gap at each timepoint. Representative images from three independent replicates are shown.

2.1.6. Discussion

This study represents a detailed molecular characterization of eight thyroid cancer cell lines with distinct genetic profiles and derived spheroids. We show that the thyroid cancer lines differ dramatically in their morphologies and size as evidenced by differences in microtubule and actin staining patterns. In addition, many of the cell lines show nuclear β-catenin staining, suggesting some level of oncogenic Wnt signaling that may play an important role in pathogenesis[72,78]. Differences in actin staining may suggest differences in migratory behavior or invasiveness. Intriguingly, the K1 (BRAFV600E-mutant) cell line undergoes rapid and dramatic changes in actin staining when treated with dabrafenib, shifting to the less invasive stress fiber actin phenotype. The RET-PTC fusion cell line TPC1 exhibited the opposite effect when treated with dabrafenib, shifting to more invasive lamellipodial actin phenotype. These actin changes were correlated with long term changes in spheroid growth, as well as functional changes in cellular capacity to migrate in the scratch assay. Overall, these actin changes may represent a major mechanism by which dabrafenib mediate its effects in vivo.

Organoids and spheroids have been shown to be better models for studying drug sensitivity than cells grown as a monolayer[79]. Here, we demonstrate that we are able to grow spheroids from all eight thyroid cancer cell lines tested. These spheroids have distinct morphologies, sizes, and staining patterns for E-cadherin and β-catenin, likely reflecting differences in their original histologic subtype and tumorigenic potential. Our work shows that two spheroid cultures derived from K1 and TPC1 cell lines accurately recapitulate the in vivo response of tumors with similar genetic composition. The BRAF-mutant K1 spheroids were significantly more sensitive to dabrafenib treatment than monolayer counterparts, while the RET-PTC fusion TPC1 spheroids demonstrated increased growth following dabrafenib treatment. In the clinic, dabrafenib is contraindicated for individuals with BRAF-wildtype thyroid cancer, as it may promote tumor growth. In addition, we found that dabrafenib increases the number of mitotic TPC1 cells in the 2D system. Thus, it is possible that dabrafenib stimulates TPC1 cell division in addition to increasing their migratory behavior.

In order to facilitate efficient drug screening for thyroid cancer, we report the first adaptation of a thyroid cancer spheroid system to a high throughput 384-well format. There are numerous advantages to studying thyroid cancer in this 3D, 384-well format. First, as 3D culture better recapitulates physiologic disease, drug screening results in 3D may provide more accurate response information than 2D to predict in vivo testing. Therefore, less false positives would be expected in 3D drug screens than in 2D drug screens and may accelerate discoveries. Second, miniaturizing the 3D spheroids to 384-well plates allows for a wider range of drugs/compounds to be tested, increasing the number of gene targets. Using high-throughput assays and automation also provides the ability to screen many cell lines/spheroids to generate "drug profiles" that can be correlated with genetic information and/or biomarkers of disease. Third, drug/compound library screening in 3D models could lead to acceleration in validating drug response/resistance mechanisms in these models that may allow for the identification of drug repurposing, drug combinations (e.g., dabrafenib + Wnt or PI3K inhibitor), or novel drug targets for the disease. Finally, 3D models in multi-well plates can allow for further studies of biology using functional genomics screening (CRISPRi or CRISPRa), for co-culturing tumor and stromal cells to study microenvironments, or co-culturing spheroids and activated immune cells to test immune modulating agents.

3D culture is an attractive, innovative method that will allow for novel research and testing of large compound libraries for thyroid cancer drug discovery. However, we also present herein the importance of traditional monolayer culture for deciphering mechanisms of disease progression. Monolayer culture is inexpensive, efficient, and can be highly useful for single-cell mechanistic studies. Our current work shows that the 2D and 3D systems represent complementary approaches for uncovering mechanisms of both intrinsic and extrinsic changes in response to drug treatment.

2.2. DEVELOPMENT OF FINE-NEEDLE ASPIRATION-DERIVED ORGANOID CULTURES

2.2.1. Summary of Project and Contribution of Study

In this subsection, I detail a project that focused on created organoid models of many different cancers, including thyroid cancer. Fine-needle aspiration (FNA) is a minimally invasive procedure that can be performed in both inpatient and outpatient settings, and it is typically used in cytopathology for diagnoses. Traditional methods for generating organoids use core needle biopsies or resected tissues, which bias cultures toward tumors that are able to be resected. Additionally, core needle biopsies contain fibrotic tissue that may hinder downstream applications and often require harsh mechanical or enzymatic dissociation prior to plating. FNA-based cell collection requires no digestion, and selectively collects cohesive cell clusters and discohesive cells such as immune cells, while leaving behind sclerotic stromal matrix. These cultures can be used for downstream flow cytometry, immunofluorescence, low- and high-throughput drug screening, and murine xenograft models. We also demonstrate that these organoids recapitulate patient tumor morphology, and others have previously described how organoids more accurately recreate patient tumor responses to therapeutics.

This work was published in *iScience* in August 2020. The text in this subsection is adapted from:

Vilgelm, A., **Bergdorf, K.,** Wolf, M., Bharti, V., Shattuck-Brandt, R., Blevins, A., Jones, C., Phifer, C., Lee, M., Lowe, C., Hongo, R., Boyd, K., Netterville, J., Rohde, S., Idrees, K., Bauer, J., Westover, D., Reinfeld, B., Baregamian, N., Richmond, A., Rathmell, WK., Lee, E., McDonald, O., and Weiss, V. (2020). Fine-needle aspiration-based patient-derived cancer organoids. *iScience 23*(8):101408.

2.2.2. Summary and Graphical Abstract

Patient-derived cancer organoids hold great potential to accurately model and predict therapeutic responses. Efficient organoid isolation methods that minimize post-collection manipulation of tissues would improve adaptability, accuracy, and applicability to both experimental and real-time clinical settings. Here we present a simple and novel fine-needle aspiration (FNA)-based organoid culture technique that is minimally

invasive and requires no further tissue processing. This method can isolate organoids directly from patients at the bedside or from resected primary and metastatic tissues, preserving the histologic growth patterns and infiltrating immune cells. Finally, we illustrate diverse downstream applications of this technique including in vitro high-throughput chemotherapeutic screens, in situ immune cell characterization, and in vivo patient-derived xenografts. Thus, routine FNA-based collection techniques currently used in the clinic represent an unappreciated substantial source of material that can be exploited to generate tumor organoids from a variety of tumor types for both discovery and clinical applications.

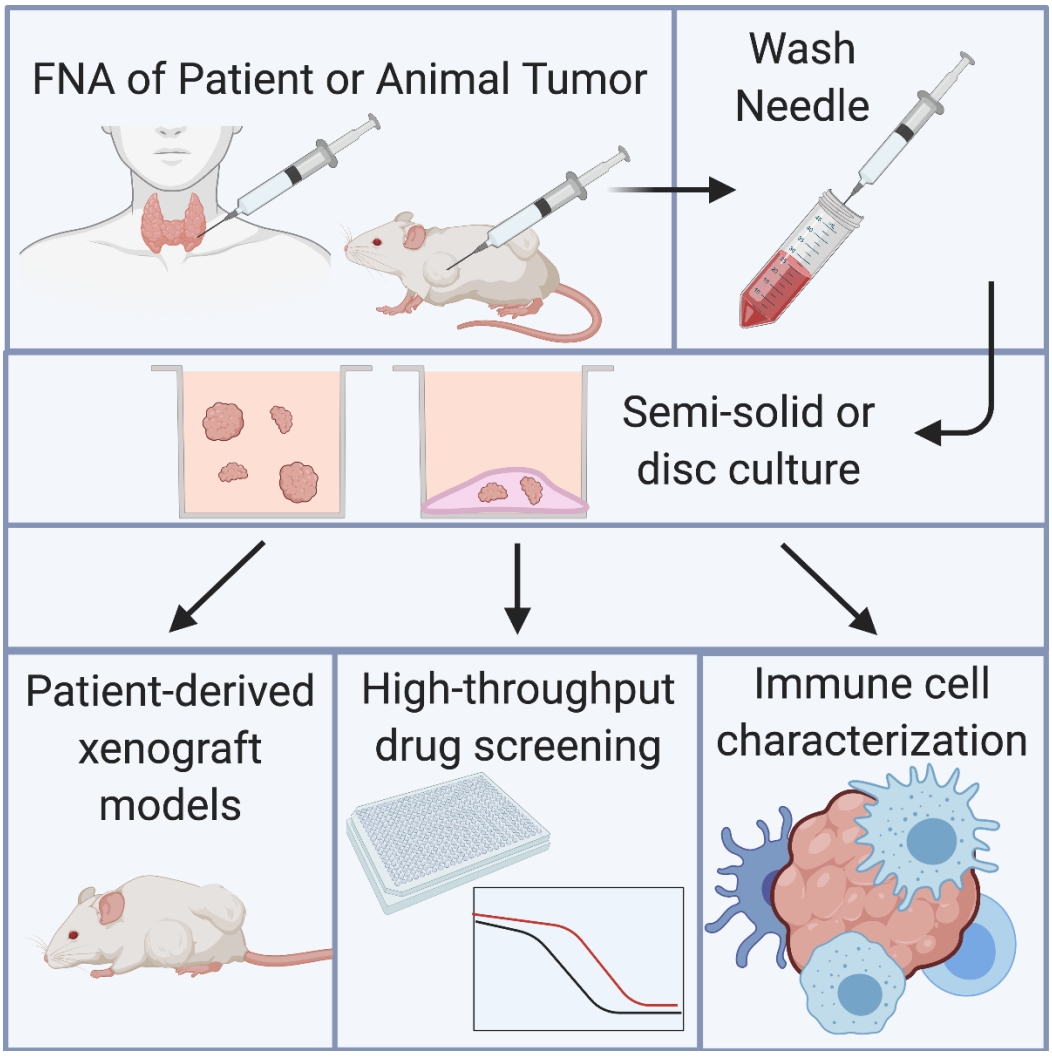

Figure 2.2.1. Graphical abstract

2.2.3. Introduction

Patient-derived tumor organoids hold great promise for biomedical science and clinical applications including personalized medicine[65,73,79,80]. However, current methods that isolate tumor organoids from patients require tissue(s) of at least 1cm^3, which are collected from surgical resection specimens or core needle biopsies. After collection, tissues must then be mechanically or enzymatically dissociated for successful isolation and plating of intact tumor organoids into Matrigel discs. Like 2D cultures, many post-isolation organoid culturing methods also rely on trypsinization of intact organoids into single cells for passaging and plating into downstream experimental formats. As such, organoid isolation is restricted to patients with surgically accessible tumors and current digestion methods disrupt native 3D growth architectures with loss of tumor infiltrating immune cells.

Fine-needle aspiration (FNA) is a minimally invasive technique that is widely used in both inpatient and outpatient settings as a first line procedure for sampling and diagnosing tumor tissues. It is often clinically preferred over core needle biopsy because of its ability to rapidly and gently extract and separate tumor from stroma, unlike core needle biopsies, while simultaneously preserving growth architectures for gold standard pathologic diagnosis[81-86]. For palpable lesions, the sample can be obtained from patients at the bedside with minimal discomfort and limited, if any, use of local anesthetic. For deeper lesions, the technique can be combined with ultrasound[87] or performed under CT guidance to precisely target the lesion of interest. FNA can also be performed directly on resected or biopsied tumor tissues immediately after surgery. Applying this technique to isolate tumor organoids could allow for a simple, minimally invasive approach that is especially suited for preservation of intact tumor organoids and their corresponding tumor infiltrating immune cells.

FNA is distinct from larger core needle biopsies, the latter of which have been widely applied to organoid isolation[88-93]. Unlike core needle biopsies, which remove intact tumor tissue including fibrotic stroma, FNA utilizes a fine needle with a bevel that is particularly adept at extracting both single cells and cell clusters out of the surrounding stroma by simply applying a rapid gentle cutting or sawing motion. FNA therefore preferentially

enriches for both cohesive units of cells (such as epithelial glands) and discohesive cells (such as immune cells), while leaving behind much of the sclerotic stromal matrix that must be removed for successful downstream applications including isolation of organoids[94]. The gentle mechanical dislodging of cells with FNA requires no tissue digestion or processing, and important 3D architectures such as solid or glandular tumor growth patterns are often faithfully preserved. The gentle FNA extraction method and lack of further processing also greatly improves cell viability (compared to core biopsy), and FNA material can also be plated into culture or submitted for ancillary studies such as flow cytometry directly out of the needle[95]. As such, FNA biopsies provide a simple, low risk clinical procedure for tumor cell isolation that is ideally suited for downstream research applications at minimal time and reagent costs.

Because of the ease and extraction advantages, we hypothesized that FNA could be harnessed as an efficient organoid isolation procedure that would improve take rates while simplifying the organoid collection and culturing process as a whole. In the current study, we provide evidence that FNA can be used in a patient-derived organoid culture method that is rapid, efficient, and closely recapitulates the wide array of native histologic architecture and biological properties of the patient's original tissue. We demonstrate the effective use of this culture technique for high throughput drug testing, patient-derived organoid xenograft models, and analysis of the tumor immune microenvironment.

2.2.4. Materials and Methods

2.2.4.1. Fine-needle aspiration technique for tumors

Fine-needle aspiration was performed on patient tumors using a sterile 25-gauge beveled needle attached to a sterile 10ml syringe with a syringe holder used for gentle aspiration. The target was immobilized with one hand with the syringe holder held in the other. The procedure can be performed without the use of a syringe holder, allowing for the sample to be drawn into the needle through capillary action. However, the concentration of tumor cells in the sample may be higher with the use of aspiration from a syringe holder. Of

note, for highly vascular or bloody lesions, a higher gauge needle and capillary action may yield a more concentrated sample. The target was immobilized with one hand and the needle was inserted perpendicular to the mass. Once the needle was within the lesion, backward pressure was applied on the syringe using the syringe holder. The needle was then quickly agitated within the lesion using long needle excursions at a rate of 2-3 strokes per second, for a total of 10-20 excursions. This rapid cutting motion was essential for the collection of a generous sample. Once cellular material was identified in the hub of the needle, the syringe holder suction was released and the needle was removed from the patient or specimen. One to three needle passes were collected from each tumor. During each aspiration, the excursions were performed in a fan-shape to ensure a larger region of sampling. In addition, particularly for larger lesions, each needle pass was performed in a separate area of the tumor for the most heterogeneous and cellular tissue collection. Insertion of the needle in along the same path as a prior pass led to increased blood collection and a more dilute sample. Following each needle pass, the needle was rinsed in either sterile RPMI 1640 or DMEM. The FNA-acquired cells were then centrifuged and immediately plated for FNA-PDO culture or stained for flow cytometry. All FNA training for this study was carried out by an experienced cytopathologist (VW).

2.2.4.2. Semi-solid FNA-PDO culture

FNAs were collected from patient tumors (1 needle pass) and rinsed in 20ml of DMEM. FNA-collected cells were then mixed with ice-cold complete media containing DMEM/Hams F12/MCDB105 (2:1:1 ratio), 12% FBS (Gibco), B27-supplement (Gibco), and 5% Matrigel (Corning). Cells were then immediately plated into 12 wells of a 24-well ultra-low attachment plate (Corning 3473). 200µl of 5% Matrigel in complete media was added dropwise to each well weekly to compensate for volume loss through evaporation.

2.2.4.3. Disc FNA-PDO culture

FNAs were collected from patient tumors (1 needle pass) and rinsed in 20ml DMEM. FNA-collected cells were then gently mixed with ice-cold complete media containing DMEM/Hams F12/MCDB105 (2:1:1 ratio), 10% FBS, B27-supplement, and 75% Matrigel. The ice-cold Matrigel and cells were then plated in 50µl discs in the

bottom of each well (3 discs per well) of pre-warmed 6-well tissue culture plate and placed in the incubator for 10 min to allow the Matrigel to solidify. Once solidified, the Matrigel discs were covered with pre-warmed complete media containing 10% FBS plus B27 supplement and this media was changed every other day.

2.2.4.4. H&E and Immunohistochemical staining of FNA-PDOs

FNAs were collected from patient tumors and plated in disc FNA-PDO culture as described above. Following FNA-PDO growth (1-2 weeks in culture), organoids were centrifuged 1200rpm for 10 minutes. Media was aspirated, and the organoids were resuspended in 10% neutral buffered formalin (NBF) for 30 minutes. The organoids were then centrifuged at 1200rpm for 10 minutes. The NBF was aspirated and the organoids were resuspended in 70% alcohol for 15 minutes three times, organoids were centrifuged at 1200rpm for 10 minutes between each alcohol wash. After the final alcohol wash cells were resuspended in 1.5% heated UltraPure™ Agarose Invitrogen/Thermo (# 16500100) and transferred to a cryomold for 30 minutes. The agarose-organoid block was processed and embedded in paraffin using a two-hour processing run.

2.2.4.5. Immunofluorescent staining of FNA-PDOs

Organoids were fixed in 4% formaldehyde prior to permeabilization with 0.5% TBST. Following a 0.1% TBST rinse, organoids were rotated in Abdil (0.1% TBST, 2% BSA) for 1 hour at RT. Organoids were stained with anti-smooth muscle actin (rabbit anti-SMA, 1:250, Abcam) and anti-cytokeratin 8/18 (guinea pig anti-CK8/18, 1:250, Abcam) in blocking buffer overnight at 4˚C. After incubation, organoids were washed in 0.1% TBST and secondary stained with AlexaFluor488-conjugated anti-guinea pig antibody and Alexa-Fluor647-conjugated anti-rabbit antibody (both 1:250, Abcam) for 2-3 hours at RT. Organoids were stained with Hoechst (Abcam) washed with 0.1% TBST, resuspended in PBS, and mounted onto glass slides with 50µl ProLong Gold Antifade Reagent (Invitrogen). After a 15-minute covered incubation at RT, coverslips were sealed with nail polish. Images were acquired using a Nikon Spinning Disk microscope with Andor DU-897 EMCCD camera and 647nm, 488nm, and 405nm lasers. Images were processed using ImageJ (Fiji, Build: 269a0ad53f).

2.2.4.6. FNA-PDO MTT assay

Gastric signet ring organoids were harvested from a 6-well plate (one 200µL Matrigel disc per plate with near confluent organoids) in ice-cold PBS, subjected to partial mechanical dissociation by pipetting up and down approximately 10 times with a glass Pasteur pipette and then centrifuged for 10 min at 8,000rpm at 4°C. Residual Matrigel was removed with a pipette, and pelleted organoids were resuspended in fresh Matrigel. 50µL of Matrigel containing FNA-PDOs were plated into a black 96-well plate, ensuring that the bottom of each well was covered. Organoids were fed with 100µL of media (Advanced DMEM, Gibco) containing 5% FBS (Gibco), 1X B-27 (Gibco), 100mg/ml EGF (Life Technologies), 10mg/ml FGF (Life Technologies), 1X Insulin-Transferrin-Ascorbic Acid (Life Technologies) every 3-4 days. Organoids were allowed to grow for approximately 2 weeks and drugs then administered in triplicate or quadruplicate every 3-4 days for an additional 2 weeks. Drug concentrations were calculated for 150µL (100µL media+50µL Matrigel). At the end of the trial, 20µL CellTiter-96 (Promega) was added to 100µL of fresh media and the absorbance (492nm) measured on a microplate reader (Molecular Devices). Background readings (Matrigel + media without organoids) were subtracted from each measurement, and data normalized by dividing each measurement by the largest value obtained on the plate.

2.2.4.7. FNA-PDO fluorescent viability assay

Cell suspensions were prepared from organoids by trypsinization. Cells were seeded in semisolid media containing 5% Matrigel (Corning) supplemented with 15% FBS, penicillin/streptomycin (Corning; 1X) and B27 (Thermo Fisher Scientific) at 40,000 cells per well in an ultra-low attachment 6-well plate. Plates were monitored daily for organoid development. The timing of organoid growth varied between different organoids, but typically organoids were observed within 1-2 weeks. Once multicellular organoids formed, drugs were added directly to culture wells for therapeutic testing. Forty-eight hours after drug dosing, propidium iodide was added to the wells at a final concentration of 8.3µg/ml. Following another 24 hours of culturing, Hoechst 33342 and Calcein AM (Thermo Fisher Sceintific) were added to the wells with organoids at final concentration of 10µg/ml and 4µg/ml, respectively. After that, organoids were incubated in standard cell culture conditions at 37°C with 5% CO_2 cultured for two hours and imaged in culture wells with an inverted fluorescent microscope.

2.2.4.8. High-throughput 384-well FNA-PDO assay

Organoids were washed and resuspended in 5ml TrypLE for dissociation. Organoids were incubated at 37°C for 30 min, with vigorous pipetting every 10 min to prevent clumping. Cells were spun down and resuspended in complete DMEM + 2% Matrigel at a concentration of 9500 cells/ml. 30µl of cell suspension was plated per well in black 384-well cell culture microplates with a cell-repellant surface (Greiner Bio-One #781976). Organoids were allowed to form for 24 hours prior to treatment with doxorubicin (25-10,000nM) or vehicle (DMSO) as a control. Following 72 hours of treatment, wells were imaged using an ImageXpress Micro XL automated high-content microscope (Molecular Devices) in the Vanderbilt High-throughput Screening (VHTS) core facility. To assess viability, CellTiter-Glo 3D (Promega) was added in equivalent volume to wells and mixed with the Bravo automated pipette liquid transfer system (Velocity 11/Agilent). Per the CellTiter-Glo 3D protocol, plates were placed on a shaker for 25 min before luminescence was quantified using a Synergy NEO (BioTek), in the VHTS core.

2.2.4.9. Disc implantation for FNA-PDOX generation

Organoids were grown in solid 75% Matrigel disc cultures. When organoid confluency in the disc reached approximately 20-40%, disks were lifted with cell scraper and gently rinsed with 1X PBS. Female Foxn1/nu mice (Jackson Laboratories) mice were anesthetized with isoflurane and small skin incision is made on the mouse flank. The disk was then lifted with a spoon-shaped microspatula and inserted subcutaneously at the incision site. The skin incision was then closed with a surgical clip. Mice were monitored weekly for tumor development and tumor volume is estimated as $V=0.5*(\text{length} \times \text{width}^2)$ based on weekly measurements of tumor dimensions with digital calipers.

2.2.4.10. Organoid injection for FNA-PDOX generation

FNA-derived organoids were expanded to confluency in 12 wells of semi-solid culture in a low-attachment 24-well plate. Organoids were spun down, washed, and resuspended in 400µl of PBS. Per IACUC-approved protocol, female NOD.Prkdc^{scid}Il2rg$^{-/-}$ (NSG) mice received 150µl of organoid suspension

subcutaneously in each flank using a 1ml Sub-Q syringe and 22 gauge needle. On average, 1,000 organoids were injected per site (range 800-1,400 organoids) with an average organoid area of 15mm2 (range 10-30mm2 area per organoid, varying based on tumor type and patient sample). Tumor growth was monitored and volume measured every other day until an endpoint of tumor size $1cm^3$. At this time, mice were euthanized and tumors removed. Fine-needle aspiration was performed on the excised tumor using a 25 gauge needle and collected cells were washed and cultured in complete DMEM to create a stable PDOX line.

2.2.4.11. Analysis of the FNA-PDO tumor microenvironment

Organoid disc cultures were generated following FNA extraction using the method described above. At the time of FNA, a portion of the sample was briefly incubated for 5 min with collagenase (Sigma C2674-1G) and DNAse (Sigma D5025-150kU) at 37°C prior to evaluation of immune cell presence and viability by flow cytometry using a MacsQuant Analyzer 10 (Miltenyi Biotec). Following FNA, the tumor was digested according to our previously published standard digestion protocol[96]. Approximately 100,000 cells were plated from either FNA or digested tumor samples in each 300µL Matrigel disc according to the methods described above. Wnt3A-enriched media was created as previously described by Neal et al.[80]. Briefly, L-WRN cells (ATCC CRL-3276) were grown to confluence prior to collection of Wnt3A, R-spondin 3, and Noggin conditioned media. Cells were removed using centrifugation, and the supernatant was frozen to ensure no L-WRN cell contaminant. Wnt3A-enriched culture media was subsequently composed of DMEM supplemented with 50% L-WRN conditioned media, 10% FBS, 1mM HEPES (Sigma), 10mM nicotinamide (Sigma), 1mM N-acetylcysteine (Sigma), 50ng/mL EGF (Thermofisher), B-27 without vitamin A (Fisher Scientific), L-glutamine (VWR), and 1X penicillin-streptomycin (Sigma). Recombinant human IL-2 (TECIN (Teceleukin) Bulk Ro 23-6019) was added (100IU/mL) to some discs and was provided by the National Cancer Institute (NCI). Following 2 weeks in disc culture, organoids were released from Matrigel using Cell Recovery Solution (BD Biosciences) per manufacturer's protocol. Once isolated, organoids were enzymatically digested using collagenase (Sigma C2674-1G) and DNAse (Sigma D5025-150kU) at 37°C for 5 minutes, and passed through a 70µm strainer to ensure cells stained were in single cell

suspension. Recovered single cells were then washed with FACS buffer (2% FBS in PBS) and transferred into a 96-well round bottom plate for immune profiling by flow cytometry on the MacsQuant Analyzer 10. Immune cell evaluation was performed following staining with the following antibodies: Human BD fc Block (BD Biosciences), anti-human CD3 (BioLegend, clone UCHT1), anti-human CD45 (BioLegend, clone HI30), anti-human CD8a (BioLegend, clone RPA-T8), anti-human CD19 (BioLegend, clone SJ25C1), anti-human CD11b, BioLegend, clone ICRF44), anti-human CD14 (BioLegend, clone M5E2), anti-human HLA-DR (BioLegend, clone L243), anti-human CD163 (BioLegend, clone GHI/61), and anti-human CD4 (BioLegend, clone OKT4).

2.2.5. Results

2.2.5.1. Fine-needle aspiration-based patient-derived organoid culture technique

FNAs utilize beveled 25-gauge needles with a 10ml syringe and syringe holder to provide gentle aspiration using 1-3 needle passes for collection. It is well documented that this technique, with its fine beveled needle and rapid cutting motion, enriches for tumor cell clusters and discohesive cells with minimal stromal extraction[71]. FNA biopsy material from patients yields intact epithelial cell aggregates and single cells that are largely free of stromal contamination, as compared to core biopsies that retain acellular matrix (Figure 2.2.2.). As such, FNA contents were plated into organoid culture directly out of the needle without any digestion or processing steps. Because FNA enriches for intact cell clusters without digestion or trypsinization, performing cell counts after FNA at the outset of the procedure is not possible for routine isolations. To approximate yields, cell counts were acquired for a representative subset of tumors to estimate the minimal tumor cellularity obtained (averaging ~1 million cells per needle pass) by FNA. As expected, the highest numbers of tumor cells were isolated from melanomas, which typically grow as solid sheets of discohesive cells. Renal cell carcinomas (RCCs) yielded nearly an order of magnitude fewer carcinoma cells, perhaps because tumor cells are embedded within a richly vascularized stroma. Despite the lower numbers, the cellularity was still more than sufficient for organoid culture. We note that these counts likely underestimate the true cellularity following FNA. Although

not included in this study, lymph nodes likely represent the upper limits of cellularity for FNA sampling with yields up to 9.6 million cells per needle pass[98].

To assess a range of tumor types for this study, FNA was performed ex-vivo on surgical specimens from both human and xenografted tumors including melanomas, papillary and anaplastic thyroid carcinomas, clear cell renal carcinomas, colorectal adenocarcinomas, gastric signet ring adenocarcinomas, pancreatic adenocarcinomas, a cholangiocarcinoma, and a low grade appendiceal mucinous tumor (Figure 2.2.3).

FNA based-Patient Derived Organoids (FNA-PDOs) were collected and cultured with equal success on human and xenograft mouse tumors. Unsampled tissue from the intact tumors were also processed for histopathology in parallel for in situ histomorphologic comparison with the FNA-PDO cultures. FNA-PDOs were then plated directly out of the needle into either semi-solid or disc Matrigel formats in order to assess the suitability of both downstream culture conditions for growth and passaging (Figure 2.2.3). Following FNA needle passes, the needles were rinsed in DMEM and centrifuged. Cell pellets were then resuspended in simplified DMEM media and Matrigel without commonly used supplements (for example, noggin, gastrin, R-spondin, Wnt3A) in order to grow organoids and ensure selection of malignant cells over resident non-neoplastic epithelial cells. The initial take-rate was 98% (44/45) for thyroid cancer FNA-PDOs; 79% (19/24) for melanoma xenograft FNA-PDOs; 94% (16/17) for gastrointestinal FNA-PDOs including 8 colorectal carcinomas, 5 pancreatic carcinomas, 1 cholangiocarcinoma, 2 gastric carcinomas, and one appendiceal carcinoma; and 80% (12/15) for RCC FNA-PDOs. This initial take-rate included cancer organoid growth in culture over 3 weeks and included both primary and metastatic lesions. Metastases, aggressive poorly differentiated primary tumors, and well-differentiated primary tumors all formed organoids with similar take rates. Successful long-term propagation for ≥5 passages following cryopreservation was achieved with a rate of 54% (13/24) for melanoma xenograft FNA-PDOs, 100% (12/12) for thyroid cancer FNA-PDOs, and 100% (4/4) for GI FNA-PDOs that have been evaluated. Renal cell carcinoma FNA-PDOs and some of the other samples were used only for short-term studies and were not cryopreserved for evaluation of long-term propagation. Despite the lack of supplements, most cancer organoid

types grew well in the simplified media without overgrowth of non-malignant cells (as confirmed by two experienced pathologists, VW and OM) and the cost of culture and subsequent experimental studies was significantly decreased. The lone exception was RCC, which required enriched media containing noggin, R-spondin, and Wnt3A. Organoids from normal renal epithelium could also be successfully grown in this enriched media with an initial take rate of 80% (4/5). Normal epithelium from thyroid, skin, and liver FNAs failed to grow in simplified media.

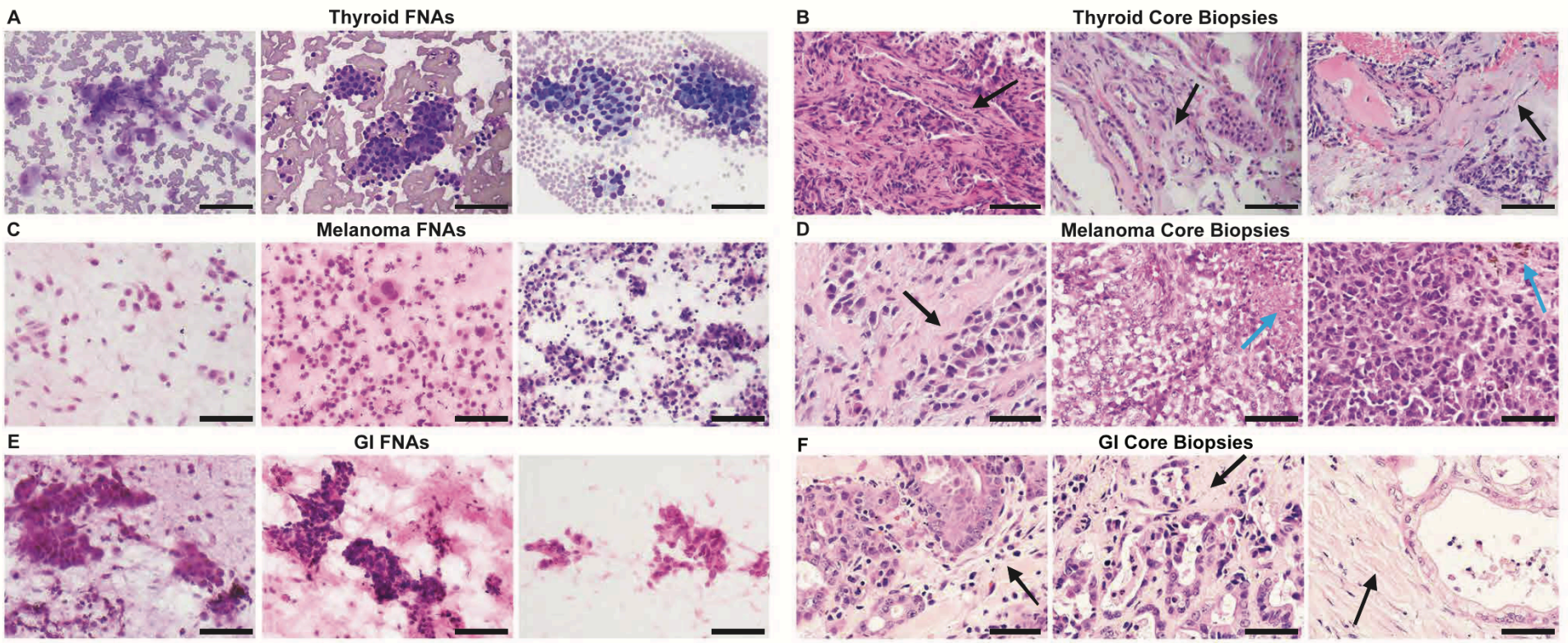

Figure 2.2.2. FNA Versus Core Biopsy Tissue. A. FNA smears of thyroid cancer (Diff-Quik stain). Left panel demonstrates predominantly discohesive tumor and immune cells aspirated from an anaplastic thyroid carcinoma. Middle and right panels demonstrate clusters of tumors cells isolated from well-differentiated papillary thyroid carcinomas. B. Core biopsy specimens (hematoxylin and eosin, H&E stain) of thyroid carcinoma from two lung metastases (left and middle panels) and one bone metastasis (right panel). Black arrow indicates fibrous stroma in core biopsies. C. FNA smears of three melanomas (H&E stain) demonstrate largely discohesive, single malignant cells. D. Core biopsy specimens (H&E stain) demonstrate numerous malignant cells with surrounding stroma (black arrow) and necrosis (red arrows). E. FNAs from gastrointestinal cancers (H&E stain) demonstrate clusters of malignant epithelial cells in colorectal adenocarcinoma (left panel), gastric adenocarcinoma (middle panel), and pancreatic adenocarcinoma (right panel). F. Core biopsy specimens (H&E stain) demonstrate malignant glands with intervening stroma in colorectal adenocarcinoma (left panel), gastric adenocarcinoma (middle panel), and the classic dense desmoplastic stroma of pancreatic adenocarcinoma (right panel). Black arrow indicates fibrous stroma in core biopsies. All images taken at 20X magnification, 50µm scale bar.

2.2.5.2. Organoids recapitulate patient tumor morphology and immunophenotype in culture

A representative subset of FNA-PDOs from both disc and semi-solid cultures were fixed and embedded in paraffin to assess tumor morphology (by H&E) side-by-side with the formalin fixed tumor tissues collected in parallel from the patients. In all cases assessed, FNA-PDO morphology faithfully replicated the tumor morphology observed in the matched patient tissues across a range of tumor histologies (Figure 2.2.3). This included spindled melanomas with vacuoles (patient 1642), pleomorphic melanomas with bizarre giant cells (patient 1826) or necrosis (patient 0431), signet ring gastric carcinomas with discohesive cells and intracytoplasmic mucin droplets (patient V50), colorectal adenocarcinomas with papillary glands and "dirty" necrosis (patient V80), appendiceal mucinous tumors with small clusters of malignant cells embedded in mucin (patient V12A), thyroid carcinomas with microfollicular (patient VWLT8), solid (patient VWLT12), psammomatous (patient VWLT14) and papillary architectures (patients VWLT13 and VWLT33), and clear cell RCCs with the classical clear cell morphology and nested growth patterns (Figure 2.2.3). In addition to the morphologies observed by H&E stains, characteristic immunohistochemical staining (IHC) was also preserved across a panel of organoids (Figure 2.2.3.). Melanoma FNA-PDOs strongly expressed S-100 protein with Ki-67 labeling (a proliferation marker), as seen in the matched tissue samples. Carcinomas retained their characteristic strong cytokeratin (AE1/AE3) expression. Nuclear TTF-1 expression was retained in thyroid FNA-PDOs. Thus, malignant cells isolated by FNA-PDO retained key histologic and immunophenotypic properties of the patient tumors from which they were derived.

Resident stromal cells were also isolated and maintained in the 3D FNA-PDO cultures in many cases. For example, fibroblasts were clearly identified in two thyroid FNA-PDOs, as illustrated by immunofluorescence labeling of carcinoma cells (green, CK8/18 positive) surrounded by supporting cancer-associated fibroblasts (red, SMA positive, Figure 2.2.4.). In particular, the disc plating method was most conducive to maintaining

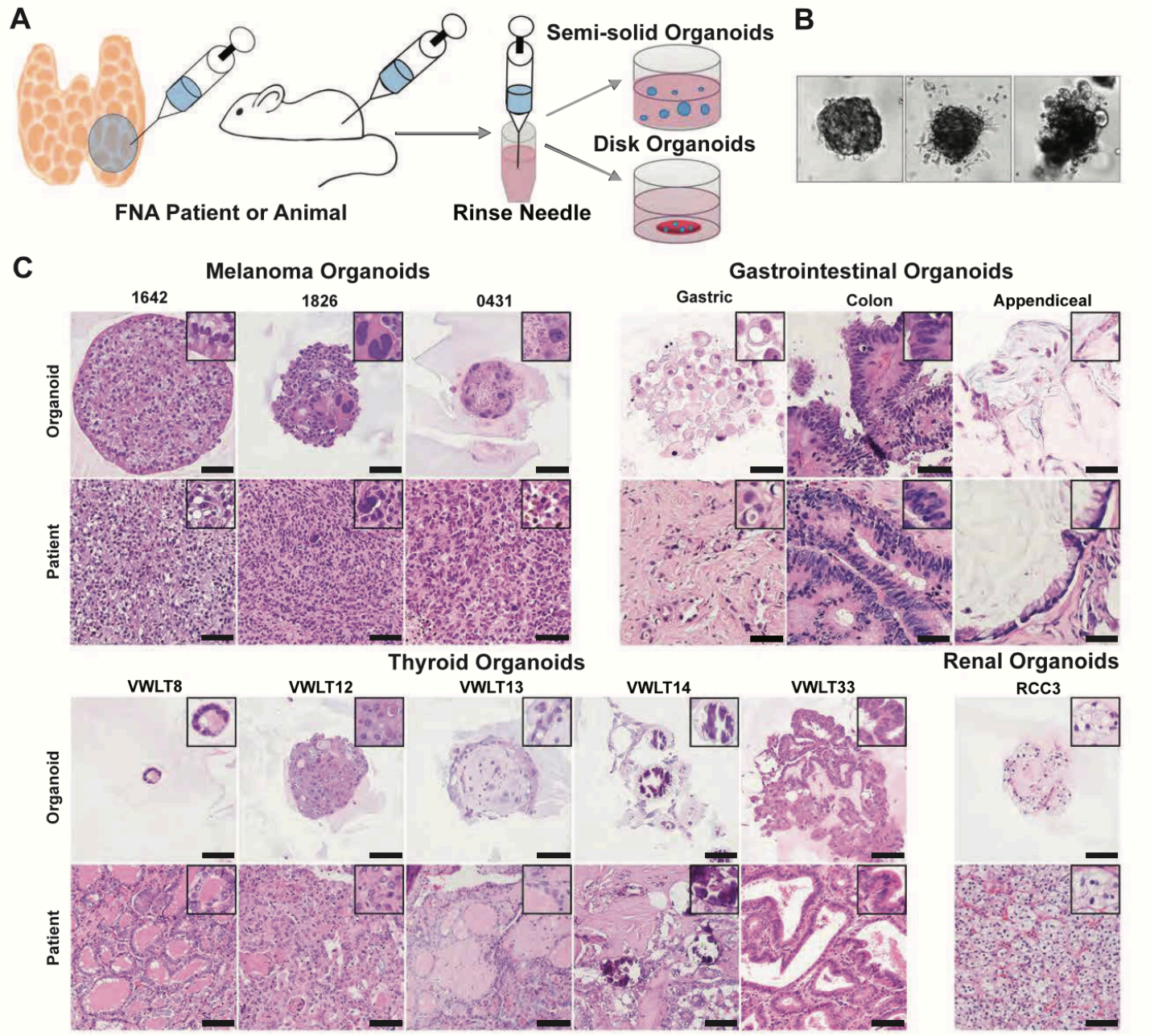

Figure 2.2.3. FNA-Based Patient-Derived Organoid Model. A. Fine-needle aspiration can be performed on patients, surgical specimens, or animals. One to three needle passes are typically collected, and the needle is rinsed in RPMI 1640 or DMEM. Following this rinse, the cells can be directly plated in either a semisolid or disc organoid format. B. Organoids begin to form within 1 week of plating and have morphologies unique to each individual patient. Three melanoma organoids shown have distinct morphology on 20× bright-field imaging. C. Organoids can also be embedded in paraffin blocks for morphologic evaluation using H&E staining, images taken at 20× magnification (scale bar, 50 µm). Organoid morphology, as seen on H&E stain, closely recapitulates the primary patient tumor morphology across multiple tumor types including melanoma, gastrointestinal carcinomas, thyroid carcinomas, and renal cell carcinoma.

cancer-associated fibroblasts. In these formats, a population of spindled fibroblasts often migrated out of the discs onto the plastic during the first few rounds of passaging, typically within 1-2 weeks of initial plating. These cells then grew exclusively as 2D cultures, as illustrated by a melanoma FNA-PDO at days 4 and 6 of culture (Figure 2.2.4.). These 2D fibroblast cultures propagated out of most FNA-PDO melanomas and thyroid carcinomas, with more variability in gastrointestinal carcinomas and RCCs. The percentage of fibroblasts migrating into 2D cultures varied between tumors and increased over time with each subsequent passage (tumor cells labeled in green with CK8/18 and fibroblasts labeled in red with SMA, Figure 2.2.4.). 2D fibroblast cultures were not observed in semi-solid organoid culture formats, presumably due to the ultra-low attachment surfaces of the plates. However, fibroblasts were identified in semi-solid culture within the organoids surrounding the malignant cells.

2.2.5.3. FNA-PDOs model therapeutic responses

We next tested whether our FNA-PDO culture method could be applied to downstream in vitro therapeutic modeling applications (Figure 2.2.5.). We first tested drug responsive organoid growth within the semi-solid format. Thyroid FNA-PDOs were treated with the BRAF-inhibitor dabrafenib at clinically relevant concentrations (30nM) for 20 days in semi-solid culture. Unlike control (wild type) thyroid carcinomas, which were insensitive to dabrafenib as expected, the BRAFV600E-mutant FNA-PDO demonstrated a partial response to therapy (Figure 2.2.5.). This is similar to the partial response rate that is observed in patients with BRAF-mutant thyroid carcinoma[63].

We next tested drug responses of organoids grown in discs plated within standard 96-well plate formats, using conventional MTT signals as a readout of organoid viability. Following 2 weeks of growth to allow mature organoid formation, a gastric signet ring FNA-PDO was treated with various chemotherapies over a subsequent period of two weeks. Standard of care palliative combination chemotherapy (5-fluorouracil: 5FU and cisplatin) demonstrated therapeutic efficacy in a concentration-dependent manner. We note that 5-FU alone was as efficacious against the FNA-PDOs as 5FU combined with cisplatin, and that FNA-PDOs also responded to

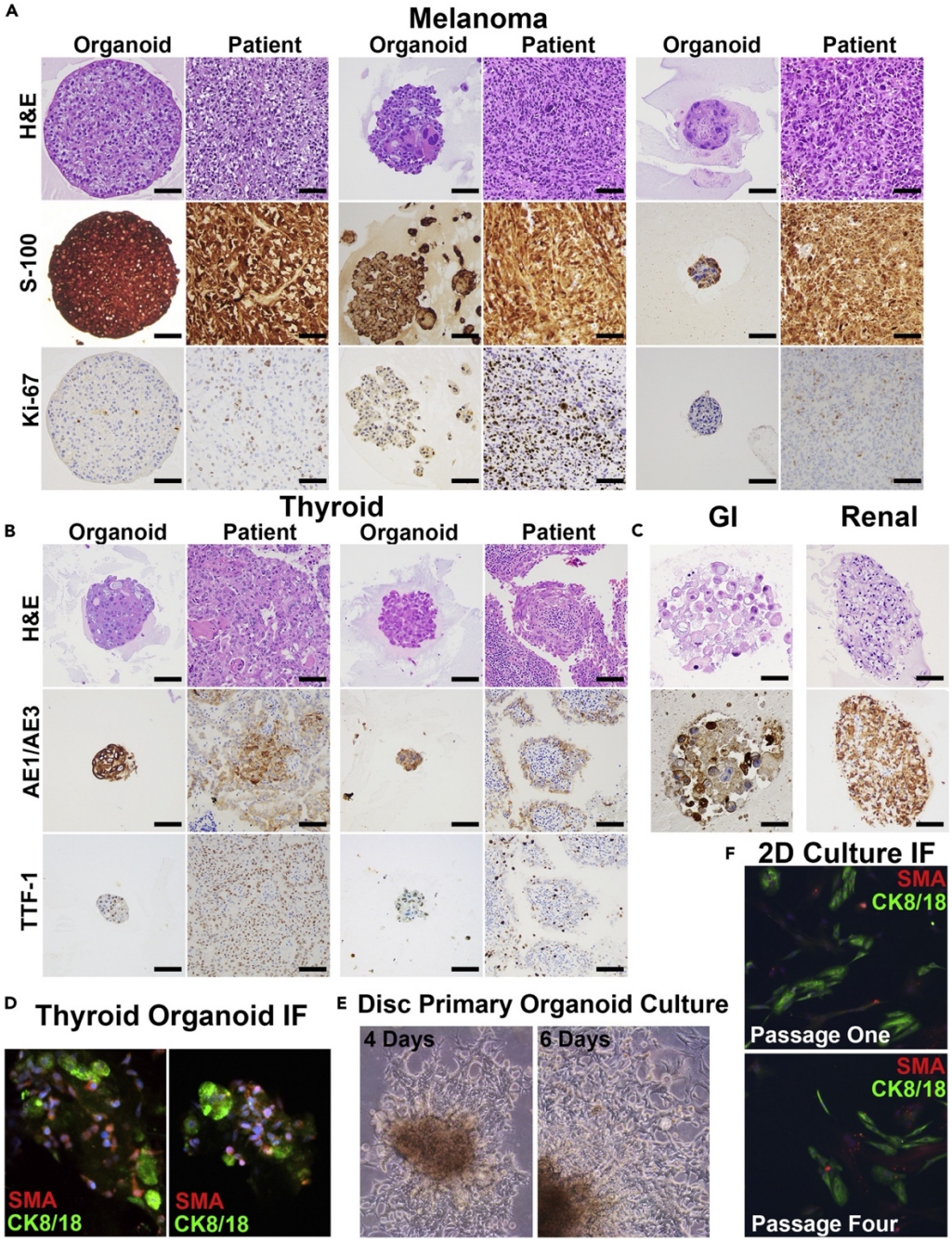

Figure 2.2.4. Patient-Derived Organoids Maintain Identical Patient Morphology and Immunophenotype in Culture. A. Three distinct FNA patient-derived organoids (FNA-PDOs) for melanoma. These organoids also maintain S-100 and Ki-67 immunohistochemical (IHC) staining similar to the patient tumor (20× magnification; scale bar, 50 µm). **B**. Two distinct FNA-PDOs for thyroid cancer maintain expression of markers indicative of thyroid differentiation, AE1/AE3 and TTF-1, on IHC (20× magnification; scale bar, 50 µm). C. Gastrointestinal and renal FNA-PDOs demonstrate preserved AE1/AE3 expression (20× magnification; scale bar, 50 µm). D. Immunofluorescence staining of the two thyroid cancer FNA-PDOs (shown in B) highlights both a population of tumor cells (green, CK8/18 positive staining) as well as a supportive population of cancer-associated fibroblasts (CAFs, red, SMA; DNA in blue; 20× magnification; scale bar, 100 µm).E. Disc organoid cultures for numerous tumor types tested demonstrate 2D cultures that extend from organoids and grow along the bottom of the plate. Bright-field images of melanoma FNA-PDO taken at 4 and 6 days of culture showing rapid growth of the 2D population (10× magnification; scale bar, 100 µm).F. Immunofluorescence of these 2D cultures (thyroid FNA-PDO shown) demonstrates both cancer epithelial cells (CK8/18, green) and cancer-associated fibroblasts (CAFs, SMA, red; 10× magnification; scale bar, 100 µm).

doxorubicin monotherapy by these assays (Figure 2.2.5). FNA-PDOs were further tested for drug response using fluorescence-based viability assays. Melanoma FNA-PDOs obtained from xenograft mice were treated with combination MEK inhibitor (0.1µM trametinib) and BRAF inhibitor (10µM dabrafenib), which are standard of care therapeutics for patients with BRAF-mutant melanoma. Viability was assessed by staining with Calcein AM (stains live cells) and propidium iodide (stains dead cells). Bisbenzimide (Hoechst 33342), a cell-permeable DNA stain, was used to visualize cell nuclei. While trametinib/dabrafenib-treated FNA-organoids remained largely intact with smaller size, fluorescent imaging revealed widespread cell death after 72 hours of trametinib plus dabrafenib exposure (Figure 2.2.5.)

Results indicate that the intact organoids obtained by FNA retain intrinsic chemotherapeutic sensitivities in vitro. Because other techniques trypsinize organoids into single cells during passaging a plating, we evaluated whether FNA-PDOs could be successfully trypsinized into single cells and regrown into organoids for drug sensitivity testing in 384 well plates. To this end, FNA-PDOs were dissociation into single cells with trypsin, plated into semisolid formats, incubated for 24-72 hours to allow organoids to reform, and assessed for drug sensitivity with both ATP measurement (CellTiter-Glo 3D) and automated high-content imaging. As shown in Figure 2.2.5., organoids formed efficiently in 384-well plates and concentration-response curves were generated during treatment of anaplastic thyroid carcinoma FNA-PDOs with doxorubicin.

.

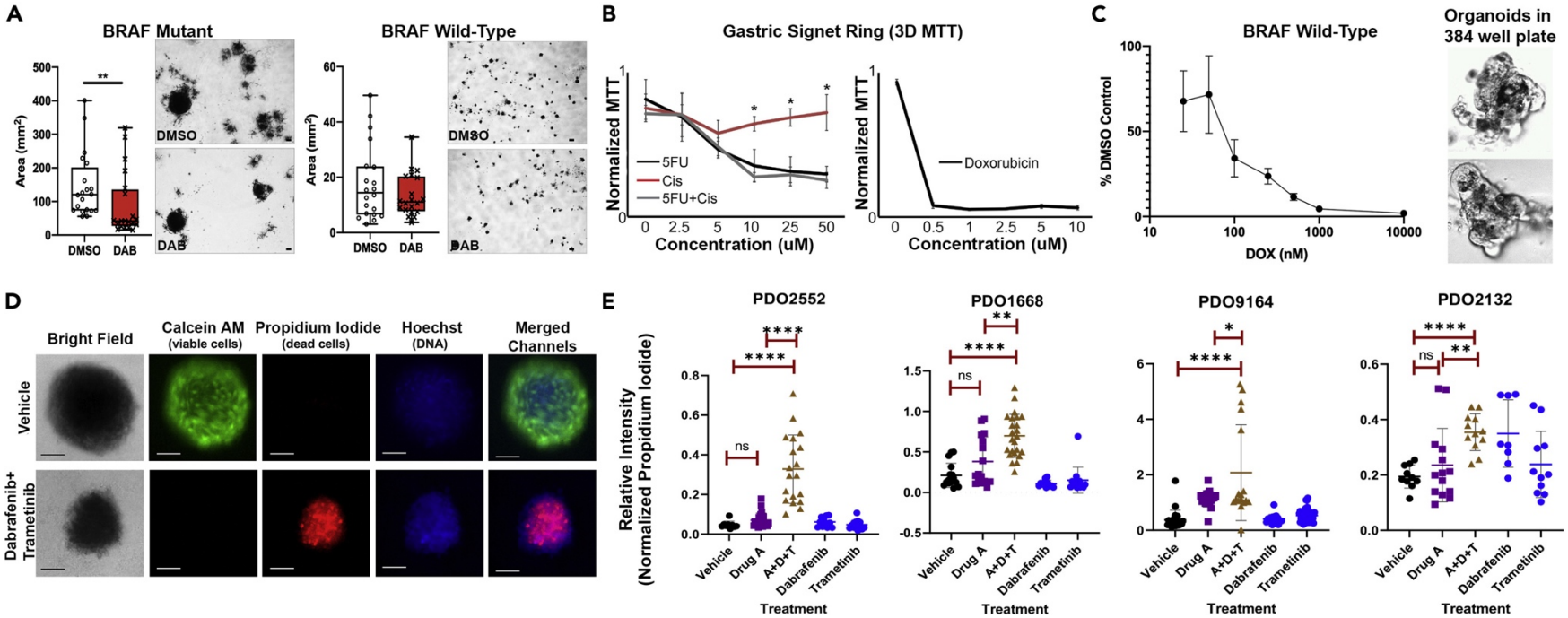

Figure 2.2.5. FNA-Based Patient-Derived Organoids are Readily Adapted to High-throughput Screening. A. FNAs directly plated in semisolid organoid culture can be tested for drug sensitivity. BRAFV600E-mutant (left) and BRAF-wild-type (right) thyroid cancer organoids were treated with dabrafenib, a BRAF inhibitor (30nM), for 20 days. BRAFV600E-mutant organoids show decreased organoid size and number following treatment. As expected, BRAF-wild-type organoids show no observable response. Images representative of three replicates. $**p < 0.05$, Mann Whitney test. B. FNA-based patient-derived gastric signet ring organoids were assayed for drug sensitivity using disc-organoid MTT assay in 96-well plates. Error bars represent standard deviation. $* = p < 0.05$ C. FNA-PDOs from aggressive anaplastic thyroid cancer were assessed for viability following doxorubicin treatment using an automated high-throughput 384-well assay. The thyroid cancer FNA-PDOs showed response to doxorubicin. Automated high content imaging also confirms organoid growth in the 384-well format, as seen in these untreated melanoma FNA-PDOs. Images representative of three replicates; error bars represent standard error of the mean (SEM). D. Using a high-throughput fluorescent assay, patient-derived melanoma organoids were labeled with Calcein AM (green fluorescence, labels live cells) and propidium iodide (red fluorescence, labels dead cells). DNA was stained with Hoechst 33342. Although the overall organoid structure remained intact, the organoid decreased in size and cells in the organoids were killed following 3 days of treatment with MEK inhibitor, trametinib (0.1 µM), and BRAF inhibitor, dabrafenib (10µm). This is in agreement with clinical data showing that dabrafenib and trametinib combination is effective for treatment of BRAF V600E melanoma[106]. Scale bar, 100 µm. E. Organoids from indicated human melanoma tumors were generated using FNA of corresponding PDX tumors grown in BALB/c nu/nu mice. Organoids were plated in semisolid media into 96-well low-attachment plates and treated with 5µM AMG-232, 1µM dabrafenib, 0.1µM trametinib, or combination of three drugs for 3 days. Calcein AM/Propidium Iodide viability assay was performed as shown in C. The ratio of the intensity of red (dead cells) and green (live cells) fluorescent signal in individual organoids was plotted. Each dot represents an individual organoid. Error bars represent standard deviation.

2.2.5.4. Xenograft studies using FNA-PDOs show aggressive tumor growth

We next tested whether FNA-PDOs could efficiently xenograft into immunodeficient mice. To this end, FNA-based patient-derived organoid xenograft models (FNA-PDOX) were successfully generated by either subcutaneous implantation of FNA-PDO cultured within discs or direct injection of FNA-PDOs harvested from semi solid cultures (Figure 2.2.6.). Although both approaches generated FNA-PDOXs, disc implantation was more preferred for aggressive tumor types, especially melanomas. Palpable flank tumors formed between 10-50 days of implantation using either method and the histomorphology of the FNA-PDOX tumor was identical to both the in vitro FNA-PDO cultures and in vivo patient tumor tissues (Figure 2.2.6). As expected, FNA-PDOX growth rates varied across tumor types and individual patient samples. However, FNA-PDOX growth closely matched growth of conventional PDXs derived from the same patient tumor(s). Despite prior in vitro passaging and generally lower cellularity of implanted FNA-PDO discs, some FNA-PDOXs also grew unexpectedly robustly, reaching 1000mm^3 within 35 days of implantation (Figure 2.2.6.). FNA-PDOXs were also generated in a similar time using less aggressive tumors (such as thyroid tumors) harvested from semi solid cultures (data not shown). These data demonstrate two methods for generating robust growth of FNA-PDOs in immune compromised mice.

2.2.5.5. Immune cell capture from FNA-PDOs

The use of human organoid models for the study of tumor immunology has been a promising area of research[99-104] that requires the successful co-culture of both tumor epithelial cells and infiltrating immune cells. We asked if tumor-infiltrating immune cells could be isolated by FNA and co-cultured with tumor cells in our FNA-PDO model, since FNA is a highly efficient method for extracting discohesive cell populations. Because RCCs are highly vascular tumors that are often enriched with well-defined populations of immune cells, we more thoroughly examined the immune capture efficiency of FNA-PDO using RCC as a model system (Figure 2.2.7).

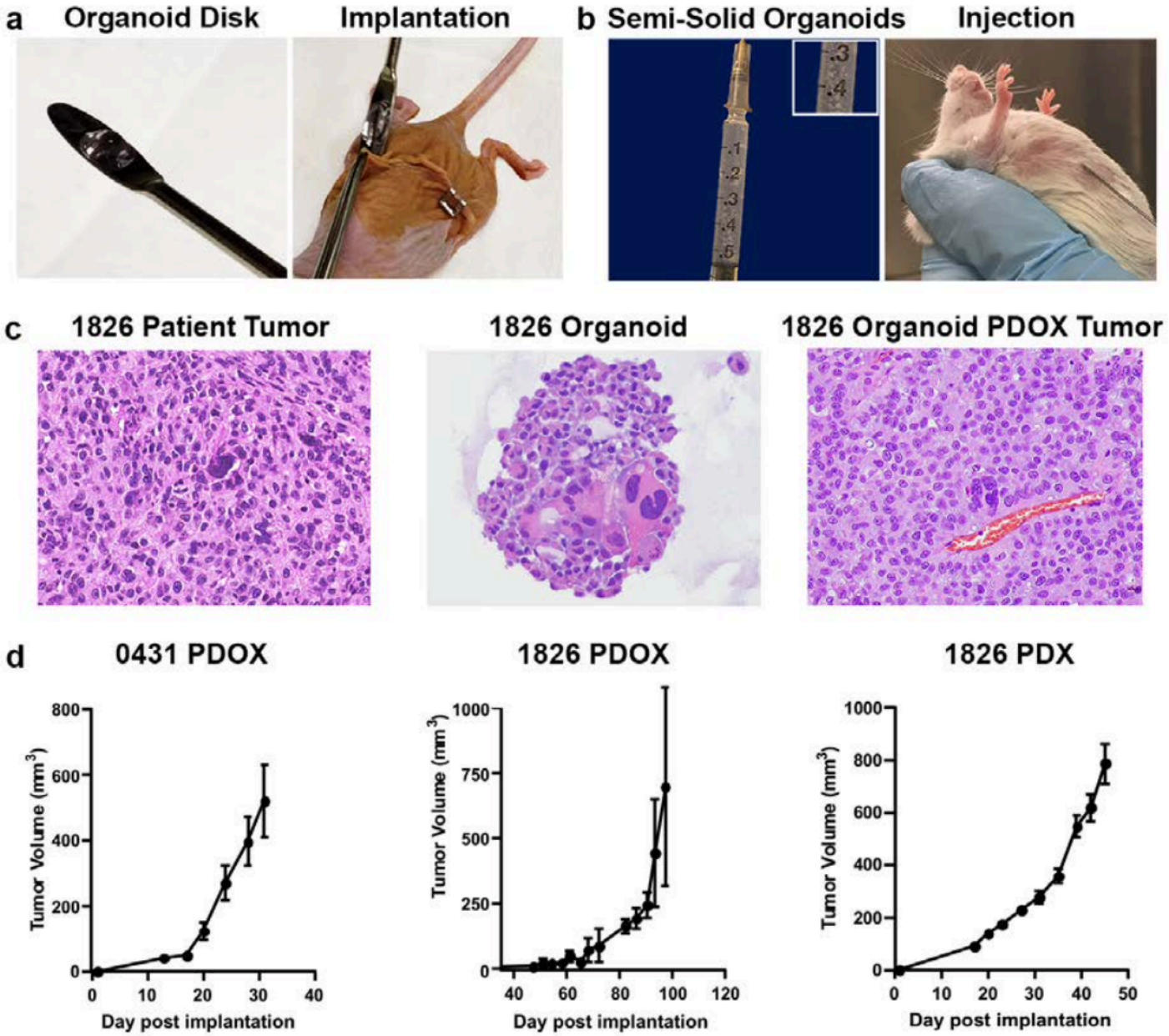

Figure 2.2.6. FNA-based Patient-derived Organoids Readily Grow in Xenograft (PDOX) Models. A. FNA-based patient-derived organoid disc cultures can be surgically implanted into immune compromised mice for creation of an FNA-PDOX model. B. For slower-growing tumors, organoids can be cultured in the semi-solid format using enriched media and then injected into immune compromised mice. C. FNA-PDOX tumors from melanomas display morphology similar to both the original patient tumor and the organoid culture. D. PDOX tumors grow robustly in both nude and NSG mice with similar tumor growth characteristics to a standard PDX model follow disc implantation. Images representative of 3 replicates; error bars represent standard deviation.

Overall, viability and initial lymphocyte and myeloid subtype yields of the captured immune cells appeared equivalent between FNA and conventional digestion methods (Figure 2.2.7.b-d). As expected, absolute immune cell counts (CD45+ cells) at collection were higher for large tumor fragments as compared to FNA, approximately 8 x10^5 for FNA (9 needle passes) vs. 6 x 10^6 for whole tumor digestion (1cm^3, Figure 2.2.7.e). However, immune cell survival was significantly higher in FNA-PDOs, likely due to the gentler extraction technique. After plating the same number of cells per organoid disc (100,000 total cells per 300µL organoid disc), the immune cell survival in FNA-PDOs was significantly higher than digestion-based PDOs at 2 weeks of culture for both complete media and Wnt-enriched media ($p<0.05$, Figure 2.2.7.f). The culture protocols for immune-containing organoids in the literature are quite complex and often recommend Wnt3A-containing or cytokine supplemented media[100-105]. We next assessed whether IL-2 supplementation and media enriched with Wnt3A, noggin, and R-spondin enhanced immune subset survival within our FNA-PDO model. Enriched media enhanced CD45+ immune cell survival with significant enhancement of CD3+ T cell and CD14+CD11b+ myeloid cell survival at 2 weeks in FNA-PDO culture (Figure 2.2.7.f-i). IL-2 supplementation further enhanced survival of CD3+ T cells subsets at 2 weeks in FNA-PDO culture (Figure 2.2.7.h). Further studies will be required to investigate various tumor types and long-term culture beyond the proof-of-principle experiments reported here. However, based on these studies, we conclude that FNA-PDO is superior to standard digestion-based PDOs in capturing resident immune cell populations from the sampled tumor microenvironment, as well as providing improved immune cell survival.

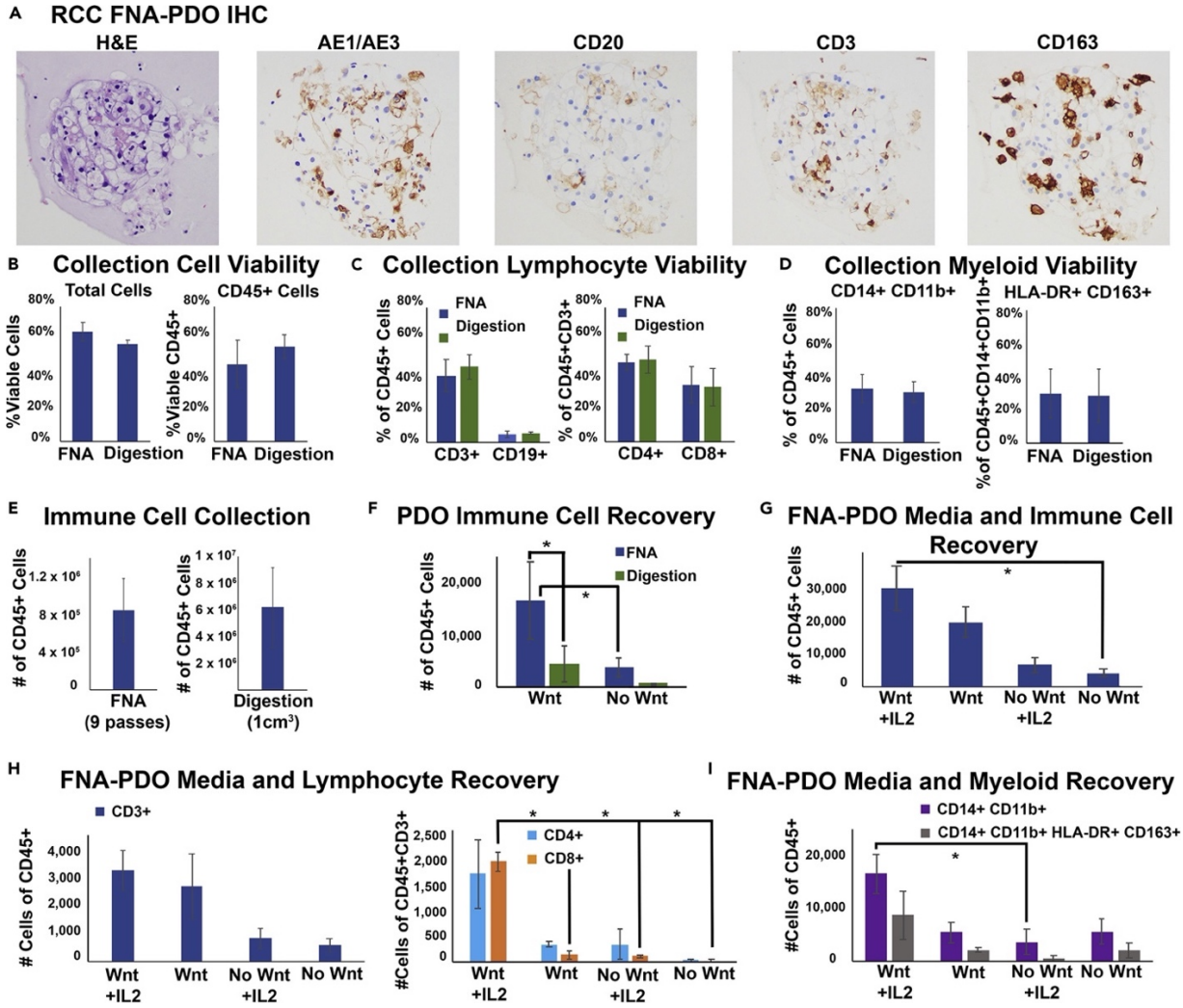

Figure 2.2.7. FNA-Based Patient-Derived RCC Organoids Contain Immune Cells from the Tumor Microenvironment. A. Immune cells are extracted and plated during FNA-PDO collection and generation. This representative RCC FNA-PDO demonstrates classic morphology by H&E with positive cytokeratin staining (AE1/AE3) and infiltration of B cells (CD20), T cells (CD3), and macrophages (CD163) by immunohistochemistry (IHC). B. Cell viability at collection was assessed using flow cytometry on fresh FNA material collected from RCCs versus fresh material following tumor digestion of RCCs, showing similar overall viability and CD45+ viability between FNA and digestion extraction methods (n = 4 tumors). Error bars represent standard error of the mean (SEM). C. Both FNA and digestion methods have similar lymphoid subset viability at collection (n = 4 tumors, error bars represent SEM). D. Both FNA and digestion methods have similar myeloid subset viability at collection (n = 4 tumors, error bars represent SEM). E. Absolute immune cell counts at collection for FNA (nine needle passes per tumor) and digestion (1 cm^3 tissue per tumor completely digested, n = 4 tumors, error bars represent SEM). F. RCC FNA-PDO and digestion-PDO immune cell recovery counts at 2 weeks of disc culture demonstrate significantly improved survival of CD45+ cells from FNA-PDOs as compared with digestion-PDOs in both Wnt3A-enriched and non-Wnt-enriched complete media (n = 4 tumors, error bars represent SEM, $*p < 0.05$). G. FNA-PDO CD45+ cell recovery counts at 2 weeks in culture demonstrates improved CD45+ cell survival with both Wnt-enriched media and 100 IU/mL IL-2 supplementation (n = 2 tumors, error bars represent SEM, $*p < 0.05$). H. FNA-PDO lymphocyte recovery counts at 2 weeks in culture demonstrates CD3+ lymphocyte survival in all conditions and improved CD8+ lymphocyte survival with Wnt-enriched media and IL-2 supplementation (n = 2 tumors, error bars represent SEM, $*p < 0.05$). I. FNA-PDO myeloid recovery counts at 2 weeks in culture demonstrates improved survival of CD14+CD11b+ myeloid cells when cultured with Wnt-enriched media (n = 2 tumors, error bars represent SEM, $*p=<0.05$).

2.2.6. Discussion and Conclusions

FNA-PDO is a simple method that can be used to isolate tumor organoids directly from patients at the bedside or from harvested tumor tissues, including biopsied tissues as small as $2mm^3$ (in our experience). Our methodology requires minimal sample processing without digestion of tissues or trypsinization of cell clusters and faithfully preserves native tumor histology. It enriches for cellular aspects of the tumor microenvironment at the expense of acellular elements, even for cancers with a highly fibrotic stroma. FNA-PDOs can be cultured and passaged without trypsinization in solid or semi-solid formats, and either format is amenable to in vitro experiments including drug screens and in vivo experiments including xenograft studies. Of note, we found that the standard media used to collect FNA samples at the bedside clinically (RPMI 1640 or DMEM) can be used here for organoid culture. Finally, FNA-PDOs allow co-isolation of tumor-infiltrating immune cell populations with enhanced immune cell survival as compared to standard digestion methods. Because of its simplicity, wide applicability, and preservation of the cellular aspects of the native tumor, FNA-PDO represents an important technical advance over conventional organoid isolation methods. With the widespread clinical use of FNA, this technique can be extensively utilized across medical centers to create organoid cultures and organoid tissue banks for precision medicine and research.

We speculate that FNA-based organoid culture holds broad potential for clinical care and basic research. Like conventional organoids, FNA-PDOs could be particularly valuable for personalized therapy, since drug responses can be assessed in vitro from the same cancer over time, including before and after treatment or surgery. FNA-PDOs could be used in combination with other assays (for example, flow cytometry) to monitor patient immune responses, tumor-immune infiltration, PD-L1 expression, tumor differentiation and viability, and drug sensitivity over the course of disease and therapy. Because FNA is widely used in the clinic and FNA-PDOs require no additional processing, we anticipate that this technique could be efficiently incorporated into current clinical workflows. Generation of FNA-PDOs requires only 1-3 weeks on average, indicating that drug sensitivity testing or other ancillary studies could be completed on a similar timeline as diagnostic molecular

testing. In the experimental setting, FNA-PDOs could be especially useful for serial samplings of tumors from xenografts or genetically engineered mice to determine treatment responses or immune infiltration patterns over time.

Finally, FNA-PDOs can be used to isolated tumor organoids and immune cells from patients or surgically removed patient specimens for general experimental purposes. Our current studies suggest that FNA-PDO represents a powerful new tool for use in personalized therapeutic drug testing, high-throughput drug discovery, xenograft generation, and tumor-immune microenvironment studies. When widely adapted, we anticipate that FNA-PDOs will provide the scientific community with a simple and cost-effective approach to directly interrogate key aspects of the tumor microenvironment in vitro more efficiently than traditional organoid cultures and more rapidly than traditional mouse models.

2.3. METHOD: OBTAINING PATIENT-DERIVED ORGANOIDS VIA FNA

2.3.1. Summary of Project and Contribution of Method

This detailed methodology accompanies the Vilgelm et al. paper above. It includes performance of the FNA, culture and maintenance, and freezing and thawing of organoid cultures. While the methods contained within that publication are sufficient to describe the process, this protocol provides specific directions to recreate the findings of the paper.

This method was published in *STAR Protocols* in January 2021, and the text contained in this subsection is adapted from:

Phifer, C., **Bergdorf, K.,** Bechard, M., Vilgelm, A., Baregamian, N., McDonald, O., Lee, E., and Weiss, V. (2021). Obtaining patient-derived cancer organoids via fine-needle aspiration. *STAR Protocols 2*:100220.

2.3.2. Summary and Graphical Abstract

Patient-derived tumor organoid cultures are an essential and innovative methodology for translational research. However, current techniques to establish these cultures are cumbersome, expensive, and often require irreplaceable clinical tissue from surgery or core biopsies. Fine-needle aspiration (FNA) provides a minimally invasive biopsy technique commonly performed in clinical settings, and we have found that it provides a cost-effective, rapid, and streamlined method of tissue acquisition for cancer organoid culture.

For complete details on the use and execution of this protocol, please refer to Lee et al. (2.1) and Vilgelm et al. (2.2).

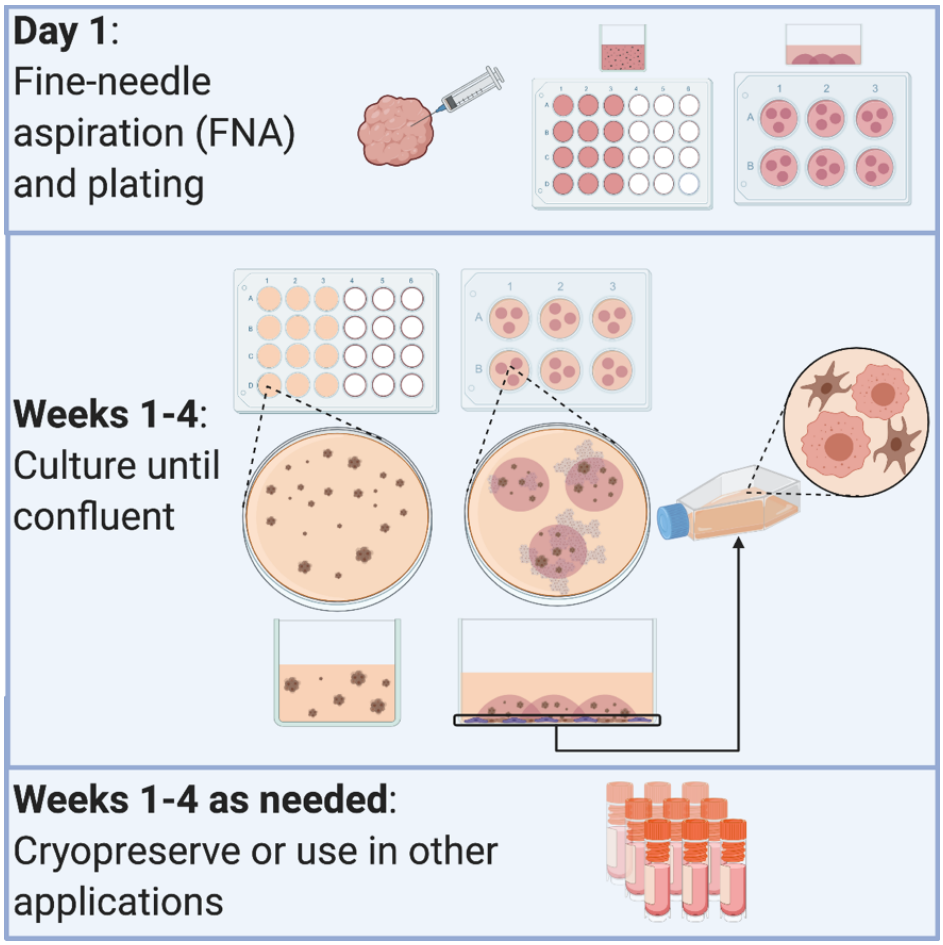

Figure 2.3.1. Graphical Abstract

2.3.3. Preparation

2.3.3.1. Matrigel Preparation

Remove stock bottle of Matrigel from -20°C storage and thaw at 4°C for 6-8 hours. Place stock bottle of Matrigel on ice in a sterile environment, as it will be used for tissue culture. Aliquot 1mL of Matrigel into labeled microcentrifuge tubes and immediately place aliquots on ice. Store aliquots at -20°C for long-term storage. Aliquots can be thawed at 4°C and we have kept aliquots at 4°C for up to a week to prevent additional freeze-thaw or waste.

2.3.3.2. Media Preparation

2.3.3.2.1. Media Component Aliquot Preparation

Aliquot Fetal Bovine Serum (FBS). Thaw 500mL bottle at 4°C, then aliquot 45mL into labeled 50mL conical tubes.

Aliquot L-glutamine. Thaw bottle of L-glutamine at 4°C for 12-24 hours for next-day aliquoting or quickly in 37°C water bath. Aliquot 6 mL of L-glutamine into labeled 15mL conical tubes.

Aliquot penicillin-streptomycin (pen/strep). Thaw bottle of pen/strep at 4°C for 12-24 hours for next day aliquoting or quickly in a 37°C water bath. Aliquot 6 mL of pen/strep into labeled 15mL conical tubes.

Store all aliquots at -20°C.

Once prepared, aliquots can be thawed for 12-24 hours at 4°C for next-day use, or in a 37°C water bath for immediate use.

2.3.3.2.2. Prepare Complete DMEM and Complete Media.

Complete DMEM: 44% DMEM, 22% Ham's F12, 22% MCDB, 10% FBS, 0.9% L-glutamine, 0.9% penicillin-streptomycin, 0.2% Normocin

Complete Media: 98% Complete DMEM with 2% B-27 Supplement

2.3.3.3. Pre-warm Plate and Complete Media

Place a 6-well plate in the incubator to warm for at least 20 minutes before use.

Aliquot 20mL of Complete Media and place in a 37°C water bath for at least 20 minutes before use.

2.3.4. Detailed Methods

2.3.4.1. Fine-Needle Aspiration (FNA)

Fine-needle aspiration is a technique commonly used in a clinical setting to obtain cells for cytopathology and genetic testing. Here, we apply it to a research setting to obtain cells and cell clumps that will generate organoid cultures. FNA is advantageous over traditional digestion methods because it is much more gentle, allowing for increased cell survival.

The specimen and FNA-setup must be sterile for tissue culture. If performing the FNA on a specimen, obtain the tissue in a sterile fashion from surgery. If obtaining tissue from surgical pathology, ensure that sterile ink is used to mark the margins prior to FNA, as the ink in surgical pathology grossing rooms is often not sterile. If obtaining the specimen from an animal, ensure sterile technique when performing in vivo FNAs or when performing surgery on animals.

Attach a sterile 25-gauge beveled needle to a sterile 10 mL luer-lock syringe and insert into a syringe holder. If using surgical tissue, transfer specimen to a sterile petri dish within a laminar flow biosafety cabinet. If performing FNA in vivo, perform in a procedure room with sterile technique. Immobilize the specimen/nodule with sterile-gloved fingers or sterile forceps and using your other hand, insert the needle with the syringe holder perpendicular to the specimen/nodule. Apply backward pressure to the syringe using the syringe holder, while rapidly agitating back and forth in a “saw-like” motion within the specimen at a rate of 2-3 strokes per second. This motion loosens tumor and other cells from the stromal matrix. One “needle pass” typically involves 10-20 forward strokes (excursions). For optimal tumor sampling, reangle the needle slightly with each excursion so that sampling occurs in a fan shape. The needle should not come out of the specimen/nodule until the 10-20

excursions have been completed and material is visible in the needle hub. The needle should not protrude from the opposite side of the specimen at any point. The speed of the agitation/strokes/excursions is critical for cellular yield. If your yield is low, check that your stroke rate is at least 2-3 strokes per second and that needle is not passing through the tissue. Once material is visible in the hub of the needle, release suction and remove the needle from the specimen. Suction should always be released prior to removing the needle from the specimen.

Traditionally, FNA is performed on patients when the nodule is 1cm or greater in greatest dimension. However, ex vivo FNA has been successfully performed on specimens as small as 2mm with adequate yield for organoid culture, including heavily fibrotic tumors.

Following this process (a “needle pass”), rinse the needle in 20mL of sterile, pre-warmed RPMI or DMEM in a 50mL conical tube. Expel needle contents into the conical tube and rinse needle 2-3 times. Extensive rinsing (more than 3-4 times) will lead to increased cell shearing and lower yields. Repeat needle passes and washes 3-5 times and dispose of syringe and needle in appropriate sharps container.

FNA yield is directly correlated with the experience of the person performing the technique. We recommend extensive practice on fruit or store-bought meat prior to attempting FNA on animals or critical specimens. In addition, different tumors may have different yields. Tumors with extensive necrosis or fibrosis may give lower viable cell yields.

2.3.4.2. Cell Growth Protocol

Once you have obtained the cells from the FNA, they can be immediately plated using one of two culture methods. Semi-solid culture is useful for longer culture periods and free movement of cells. Disc culture can be beneficial for more compact organoid growth and allows for generation and propagation of two-dimensional cultures. We recommend using both semi-solid and disc culture methods for new organoid cultures, as the growth needs vary from culture to culture.

Centrifuge the FNA material in the conical tube at 340 x g for 5 minutes at 20-25°C. Aspirate the supernatant and resuspend the pellet in Complete Media.

If using only one plating method, we recommend resuspending the FNA material in 300µL. If both plating methods are to be used, we recommend resuspending the FNA material in 600µL and dividing into two 300µL aliquots. Cells can be plated in semi-solid culture to obtain organoids, or in disc culture to obtain both organoids and 2D cell cultures.

2.3.4.2.1. Semi-solid culture

Pipet and mix 300µL of the FNA cell suspension with 5% Matrigel in complete media with an additional 2% FBS. Pipet 550µL cell suspension in a 24-well low attachment plate following a figure 8 motion while gently expelling cell suspension. Place the cells in the incubator.

Replenish 200µL per well of fresh complete media, 5% Matrigel, and 2% FBS dropwise weekly. Passage cells as needed. In this type of culture, the low percentage of Matrigel makes the matrix fragile and is more susceptible to media evaporation.

2.3.4.2.2. Disc culture

Pipet and mix 300µL of the FNA cell suspension with 75% Matrigel and 25% complete media. Add three 50µL drops (disc) to each well of a pre-warmed 6-well plate. Alternatively, you can plate a single 150-200µL disc per well of the 6-well plate. Place the plate in a tissue culture incubator for 10 minutes to allow the Matrigel to solidify. Cover cells with warmed complete media by slowly pipetting the media down the side of the well until the discs are completely covered (~2.5mL). Place cells back in the incubator. Replace media every 2-3 days by aspirating off the old media and replacing it with prewarmed complete media.

2.3.4.2.2. Two-dimensional (2D) cell culture

Follow the disc culture protocol until 2D cells have undermined the disc. Freeze the disc down following the freezing cells protocol. Add 2mL of 20-25°C complete media to each well after removing disc. Make

sure media is either 4°C or 20-25°C, as 37°C media could shock the cells. While in a 6-well plate, replace media with fresh, pre-warmed media every 2-3 days. Once cells are confluent, passage them from the 6-well plate to a T75 flask following the passaging cells protocol. In the T75, replace three-fourths (~11mL) of complete media with fresh complete media weekly. Passage cells as needed. If 2D culture is not desired, plate in a low-attachment plate in the semi-solid format. Low-attachment plates prevent the matrix disrupting 2D cells from growing underneath the organoids.

2.3.4.3. Passaging Cells

Cells should be passaged when media needs replaced or replenished more often than twice a week or when organoids are harvested for experimental use.

2.3.4.3.1. Semi-solid culture

Pipet the organoid suspension with a P1000. In order to break up the Matrigel/organoids, draw a small amount of organoid suspension up into the pipet and then expel it slowly while moving the pipet in a circular motion in the plate. Repeat this 2-4 times. Transfer the cell suspension to a 50mL conical tube. Centrifuge the cell suspension at 340 x g for 5 minutes at 20-25°C and aspirate off the supernatant. Resuspend the pelleted cells in complete media. Pipet out the desired amount of the cell suspension and replate following the cell growth protocol. Either discard the remaining cell suspension or save for other uses (e.g. freezing, plating for experiments)

2.3.4.3.2. Disc culture

Remove media and add 1mL ice-cold PBS to each well. Scrape discs gently off of the plate with a cell scraper. Pipet ice-cold PBS to break apart discs and collect into a 1.5mL microfuge tube. Centrifuge cells at 340 x g for 5 minutes at 20-25°C then remove PBS and Matrigel overlying the pellet. Wash pellet gently with 1mL 4°C PBS and centrifuge 340 x g for 5 minutes at 20-25°C. Remove PBS and resuspend cell pellet in 3X Matrigel (for a 1:3 split), then plate in pre-warmed 6-well plate.

2.3.4.3.3. 2D cell culture

Aspirate off all the media and add 1mL of trypsin to each well. Incubate at 37°C for 3 minutes. Pipet trypsinized cells from each well into a conical tube with 20mL of DMEM or RPMI. Centrifuge the cell suspension at 340 x g for 5 minutes at 20-25°C and aspirate off the supernatant. Resuspend cell pellets in 1 mL of complete media then transferred to a T75 containing 14mL of complete media. Rock the T75 back and forth until the bottom is covered with cell suspension and place in the incubator.

2.3.4.4. Freezing Cells

As these cultures come from ex vivo tissue, they are not easily replaceable or replicable. We recommend freezing down multiple vials of any organoid cultures before beginning experiments, as these cultures can be fragile and do change over time. Freeze downs enable preservation of the cultures should there be a contamination or error in propagation.

2.3.4.4.1. Obtaining Cells

2.3.4.4.1.1. Semi-solid cultures

Follow the passaging cells protocol in 2.3.4.3.1. and save the remaining cell suspension. Plan to freeze approximately 2 wells per cryovial.

2.3.4.4.1.2. Disc Culture

Aspirate off media and pipet 1mL of 4˚C PBS directly on to the disc in each well. Use a cell scraper to gently scrape off any remaining disc. Pipet cell suspension into a 1.5mL microfuge tube. Pipet up and down several times to dissolve the Matrigel. Plan to freeze approximately 2 wells per cryovial.

2.3.4.4.1.3. 2D culture

Follow the passaging cells protocol in 2.3.4.3.3. and save the remaining cell suspension. Count the cells in your preferred method. Centrifuge the cell suspension at 340 x g for 5 minutes. Aspirate off the supernatant and resuspend in complete DMEM. Freeze 300,000-1,000,000 cells per cryovial.

2.3.4.4.2. Freezing Cells

Pipet 700µL of cell suspension, 200µL of FBS, and 100µL DMSO into each appropriately labeled cryovial. Screw the cap on tightly and invert 2-3 times. Place directly into a Mr. Frosty. Tighten the lid on the Mr. Frosty and place directly into a -80˚C freezer. Keep cells in Mr. Frosty for at least 24 hours and then they can be transferred to a box prior to transfer to liquid nitrogen for long term storage. After a week in the -80˚C freezer, transfer cells to a liquid nitrogen freezer at or below -130˚C for longer storage.

2.3.4.5. Thawing Cells

Cultures must be properly thawed to give the cells the best chance of recovery. Growth may not immediately match that of the culture prior to being frozen but should pick up within a week or two after thawing.

Preheat water bath to 37˚C. Pipet 20 mL of media into a 50 mL conical tube warm to ~24˚C and obtain cryovial with cells. If thawing more than one or two cryovials at a time, store the other cryovials on dry ice until ready to thaw. Place cryovial in water bath. Incubate for 1 minute then check to see if it has thawed. If not, check in 15-30 second intervals until thawed. Once thawed, pipet contents from cryovial into the media from step 2. Rinse the cryovial with 1000µL of room temperature media and pipet it back into the conical tube.Screw the conical tube lid tightly and invert to ensure adequate mixing and dilution of the DMSO. Centrifuge at 340 x g for 5 minutes and aspirate off the supernatant. Resuspend in media and plate as desired.

2.3.5. Discussion and Limitations

This protocol describes an effective and minimally invasive method to establish patient-derived cell lines and three-dimensional growth of these cells. Between one to three weeks of culture, single cells and small clusters obtained from FNA grow to create small organoids. Initial organoid culture success rates and long-term propagation rates following cryopreservation can be found in Vilgelm et al., 2020[107].

Not all tumors robustly produce organoids, although most tumors we assessed grow with this method including thyroid, colon, pancreas, gastric, renal, and melanoma. We recommend utilizing both culture methods

when a sample is collected (semi-solid and disc), as some samples will preferentially grow in the semi-solid culture, while others will preferentially grow as discs. In addition, not all tumor types will generate a robust population of 2D cells. Two-dimensional cultures are typically composed of both fibroblasts and tumor cells, with the fibroblast percentage increasing with each passage. In our hands, thyroid and melanoma grow the most robust 2-D cultures, with gastrointestinal and renal tumors having fewer or no 2D cells.

It is vital to obtain the sample directly from surgery or as soon as it reaches surgical pathology. This is to make sure the samples are sterile. If the sample is not obtained during these times, the grossing/dissection in surgical pathology can cause contamination or cell death (i.e. ink, formalin, etc.).

2.4. METHOD: IMMUNOFLUORESCENT STAINING OF SPHEROIDS AND ORGANOIDS

2.4.1. Summary of Project and Contribution of Method

Prior to this work, the majority of immunofluorescent staining of three-dimensional cultures required specialized materials and equipment, as well as many expensive reagents. Here, we present an accessible method for identification of fibroblasts and cancer cells within organoids, as well as basic immunofluorescent staining of spheroids.

This method was published in *STAR Protocols* in June 2021 and the text contained in this subsection is adapted from:

Bergdorf, K., Phifer, C., Bechard, M., Lee, M., McDonald, O., Lee, E., and Weiss, V. (2021). Immunofluorescent staining of cancer spheroids and fine-needle aspiration-derived organoids. *STAR Protocols 2*:100578.

2.4.2. Summary and Graphical Abstract

Our organoid generation technique has allowed for the development of downstream organoid applications. Here, we detail an accessible, straight-forward protocol for immunofluorescent staining and imaging of thyroid

cancer organoids, particularly those with tumor de-differentiation. Immunofluorescence is a powerful tool to help understand the localization of cell types within organoids and determine the interactions between those cells. As organoids have been shown to recapitulate patient tumor morphology, immunofluorescent staining and imaging of organoids allows for enhanced understanding of near-in vivo structures. For complete details on the use and execution of this protocol, please refer to Lee et al. (2.1) and Vilgelm et al. (2.2).

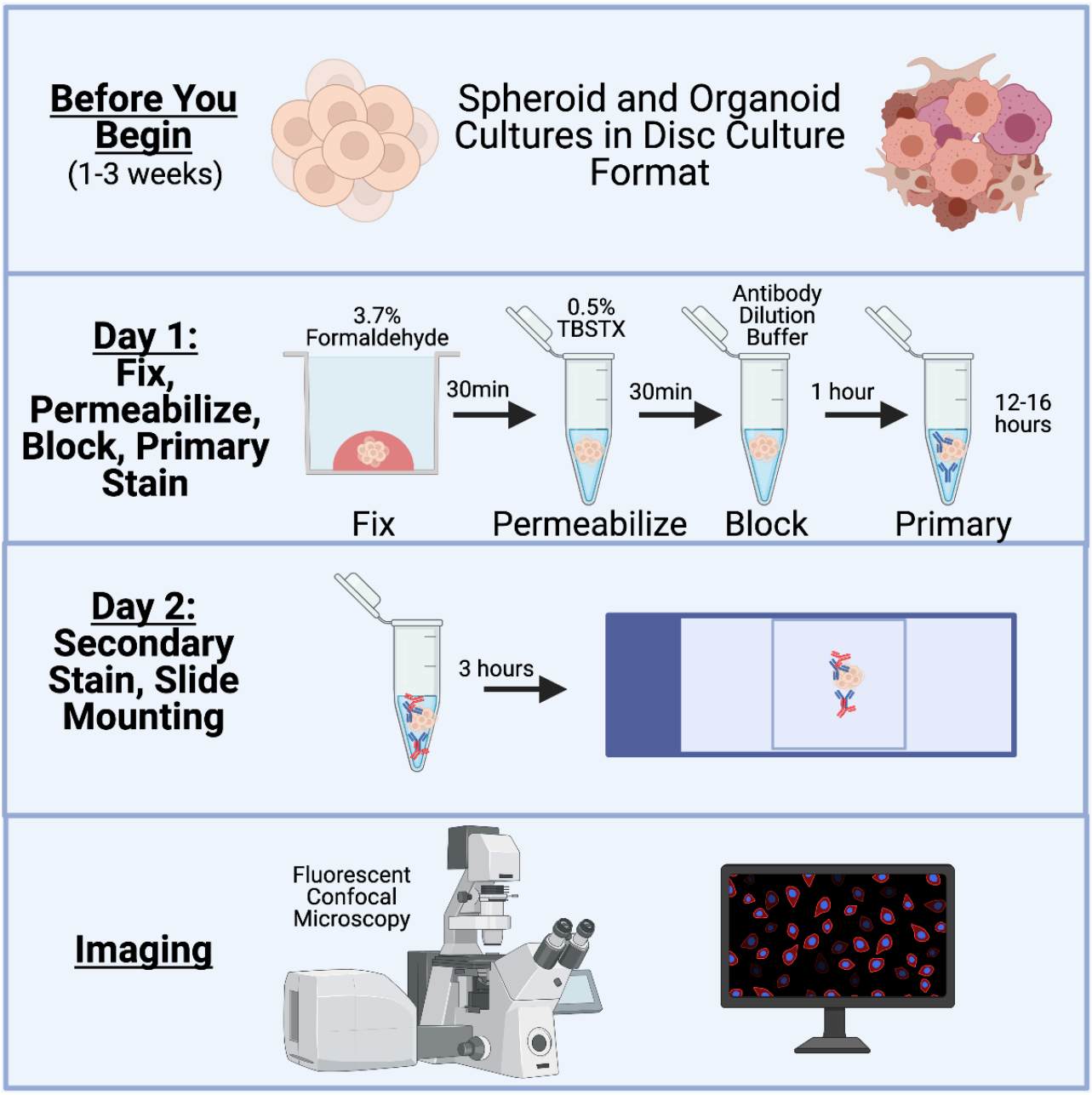

Figure 2.4.1. Graphical Abstract

2.4.3. Preparation

2.4.3.1. Reagent Preparation

Prepare cytoskeleton buffer, 0.1% TBSTX, 0.5% TBSTX, and Antibody Dilution Buffer.

Cytoskeleton buffer: 10mM MES pH 6.1, 138mM KCl, 3mM $MgCL_2$, 1.25mM EGTA pH 7.1 in MilliQ water.

0.1% TBSTX: 0.1% Triton X-100 in 1X Tris buffered saline

0.5% TBSTX: 0.5% Triton X-100 in 1X Tris buffered saline

Antibody dilution buffer: 2% bovine serum albumin in 0.1% TBSTX

Store 0.1% TBSTX, 0.5% TBSTX, and Antibody Dilution Buffer at 4°C. Cytoskeleton buffer must be prepared fresh.

2.4.3.2. Spheroid or Organoid Growth

Spheroids/organoids should be grown in 75% Matrigel disc cultures as described in 2.3.

Spheroid/organoid size will vary drastically between cultures, so there is no recommended size or density to have prior to immunofluorescent staining. However, we generally recommend that there be more than one organoid to be stained, due to the potential for loss. This protocol may also work using the semi-solid culture method, but we find the disc method preferable for downstream immunofluorescent staining.

This protocol is effective for baseline characterization of cultures in addition to analyzing treatment effects. Drugs or supplements can be added to the media surrounding the Matrigel discs prior to performing this protocol.

Many published organoid/spheroid immunofluorescence protocols grow their cultures and stain in sterile chamber slides. We found that this method complicated long-term culture of some slow-growing organoids, as it made media changes more cumbersome and frequently led to disc detachment. Additionally, because we could not centrifuge the chamber slides easily, extra time was needed for organoids/spheroids to settle to the bottom of the chamber between each step. This greatly increased the length of the staining protocol and loss of cultures. For these reasons, we recommend growing the cultures in normal disc-culture conditions and performing all staining and fixation in microcentrifuge tubes prior to transferring to a slide.

2.4.4. Detailed Methods

2.4.4.1. Fixing and Permeabilization

Organoids must be fixed prior to staining to preserve protein localization and structure, and to prevent degradation. Permeabilization disrupts the cell membrane to allow for intracellular staining.

2.4.4.1.1. Fix the organoids.

Aspirate media from the wells of disc culture, leaving only the Matrigel discs containing the spheroids/organoids.

Put 2 mL of fixative in each well and incubate plate at 4°C for 15 minutes. After 15 minutes, swirl the plate by hand and place back at 4°C for another 15 minutes.

Pipette to break up the Matrigel and transfer into a labeled 2 mL microcentrifuge tube.

Unless otherwise stated, all steps that involve mixing of organoids will use a P1000 tip with the tip cut off at the end. This is done to prevent mechanical disruption of the organoids.

2.4.4.1.2. Wash and permeabilization

Wash: Centrifuge the organoids at 2300 x g for 5 minutes in a microcentrifuge. Aspirate off the supernatant, paying careful attention to not disrupt the pellet. Resuspend the pellet in 1mL of 0.1% TBSTX with a P1000 and repeat centrifugation and aspiration.

Resuspend each pellet in 1mL 0.5% TBSTX and place tubes on rotator at room temperature (20-22°C) to permeabilize for 30 minutes.

2.4.4.2. Blocking and Staining

Blocking prevents non-specific staining before any antibodies are added. The primary antibody will detect the protein of interest, and the secondary antibody will detect the primary antibody and allow for fluorescent imaging.

2.4.4.2.1. Blocking and primary immunostaining

Repeat wash step in 2.4.4.1.2. and resuspend pellets in 1mL Antibody Dilution Buffer.

Place on rotator for 1hr at room temperature (20-22°C) to block.

Organoids can be left in the Antibody Dilution Buffer for blocking overnight (12-16 hours).

For fibroblast/tumor cell staining: add both the anti-smooth muscle actin antibody and the anti-cytokeratin 8/18 antibody at a dilution of 1:250 each, directly to the Antibody Dilution Buffer.

For β-catenin staining: add the anti-β-catenin antibody to a final dilution of 1:500 directly to the Antibody Dilution Buffer. Place on rotator at 4°C for 12-16 hours.

Staining can be done for shorter time periods at room temperature (20-22°C) or 37°C, but this will need to be optimized for each antibody and may increase background staining.

2.4.4.2.2. Secondary immunostaining

Remove from rotator and repeat wash step in 2.2.4.1.2. Resuspend pellets in 1mL Antibody Dilution Buffer. For fibroblast/tumor cell staining: Add anti-guinea pig and anti-rabbit secondary antibodies, each at a dilution of 1:250, directly to the Antibody Dilution Buffer/organoid suspension. For β-catenin staining: Add anti-mouse secondary antibody to a final dilution of 1:500 in Antibody Dilution Buffer. Place on rotator in the dark at room temperature (20-22°C) for 3 hours.

2.4.4.3. Slide Preparation and Imaging

Slide preparation is the final step that must be done before slides can be stored indefinitely. Imaging and analysis can occur days or weeks after the slides have been prepared and sealed.

2.4.4.3.1. Wash and mount on slide

Repeat wash step in 2.4.4.1.2.

You may resuspend pellet in 0.1% TBSTX and add Hoechst at a 1:1000 dilution, then rotate for 20 minutes at room temperature (20-22°C) in the dark and repeat wash step in 2.2.4.1.2.

You can also resuspend the pellet in 0.1% TBSTX with phalloidin at a 1:100 dilution, then rotate for 20 minutes at room temperature (20-22°C) in the dark and repeat wash step in 2.2.4.1.2.

Remove as much of the supernatant as possible without disturbing the pellet.

Resuspend organoids in 50µL PBS with a P200 with the end of the tip cut off and pipette the organoid suspension onto a labeled slide. Allow the organoids to settle. Tip the slide slightly so that the PBS pools in one spot, leaving the majority of the organoids in place. Aspirate the PBS, taking care not to disturb the organoids. Pipette 50µL Prolong Gold Antifade onto the slide.

If using Hoescht, use Prolong Gold without DAPI. If not using Hoescht, use Prolong Gold with DAPI. Prolong Gold enables long-term storage of slides prior to imaging, as long as the slides are sealed and properly stored.

Place a coverslip over the slide without creating bubbles. Seal the edges with clear nail polish and allow to cure in the dark for 5-10 minutes.

At this point, slides can be stored in a dark box at 4°C until ready to image.

2.4.4.4. Image

On the confocal microscope, use the focusing adjustment knobs to adjust the z-plane down to the bottom of the organoid of interest and select it as “bottom.” Adjust the z-plane up to the top of the organoid and select it as “top.” the recommended step size (typically 1-2um.Select “create Z-stack.” Once finished, save file. If imaging multiple color channels, make sure to image from the longest wavelength to the shortest wavelength (i.e. image 561nm then 488nm then 405nm) to prevent bleaching. Samples will bleach faster at higher magnifications, so always start with low magnifications before going to higher magnifications.

Perform analysis of your choice.

2.4.5. Expected Outcomes

Expected outcomes are demonstrated in Figure 2.4.2.

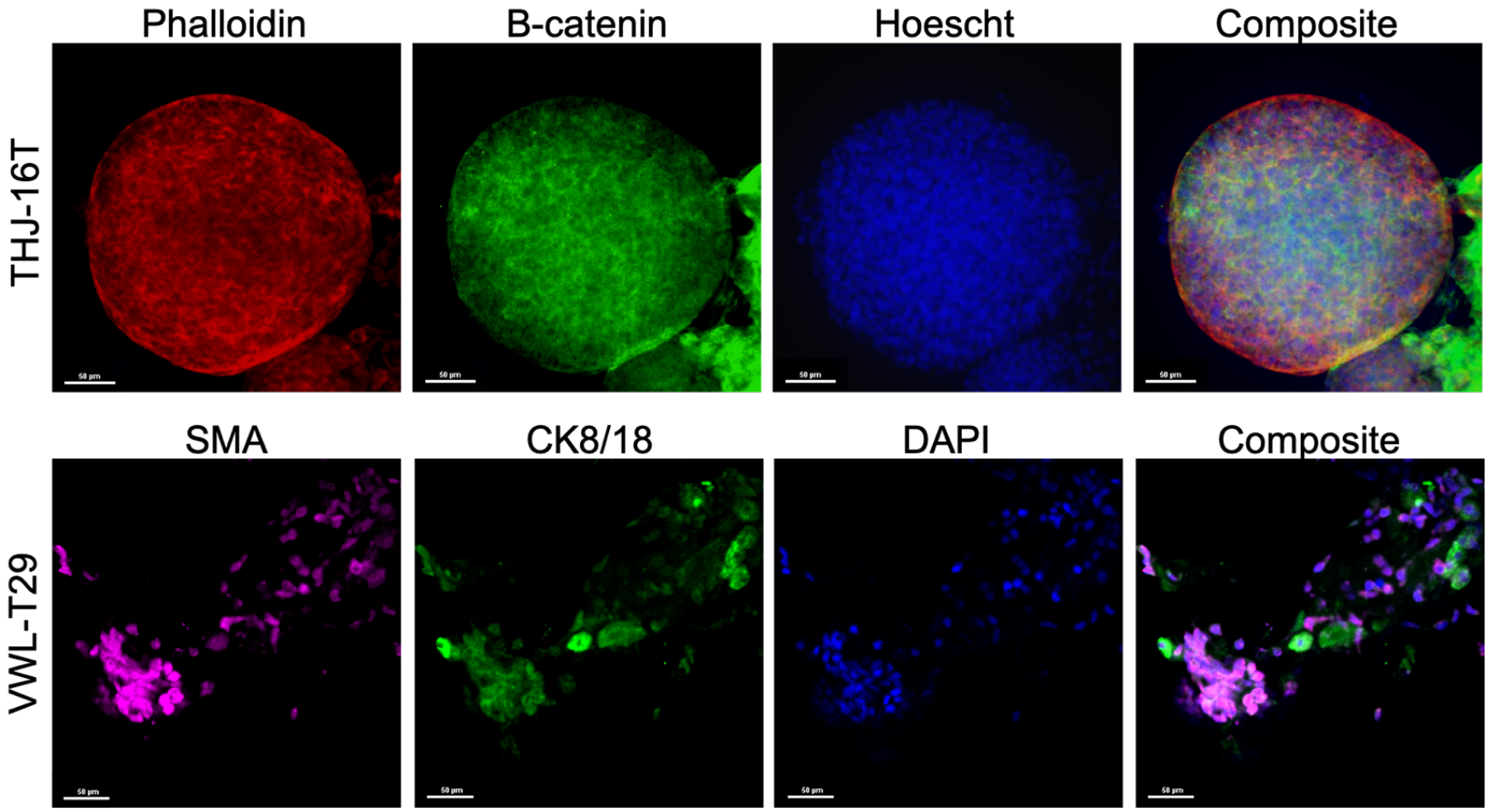

Figure 2.4.2. Example of results. THJ-16T, a thyroid cancer cell line, was grown in spheroid format then stained with phalloidin (actin filaments-red), β-catenin (green), and Hoechst (nuclei-blue), reprinted with permission from Lee, et al., 2020. VWL-T29 is a primary patient organoid obtained as described in Phifer et al., 2.3. This line was stained for smooth muscle actin (SMA, fibroblasts, magenta), cytokeratin 8/18 (CK8/18, tumor cells, green), and DAPI (blue), reprinted with permission from Vilgelm et al., 2020. Scale bars are 50um.

2.4.6. Discussion and Limitations

While we have had great success in staining thyroid cancer organoids for smooth muscle actin, cytokeratin 8/18, α-tubulin, and β-catenin, these methods may not work for all antibodies in all organoid types. Some organoids have a dense extracellular matrix that will retain antibodies and cause high levels of background staining, while preventing the antibody from reaching the specific target within the cells. Additionally, due to the frequent centrifugation and aspiration, it is expected that some cell/organoid loss will occur. We recommend performing this protocol with robust cultures (many organoids or large organoids) to ensure that many organoids are available for imaging.

Organoids are certainly more difficult to stain and image consistently due to the range of cell types, where spheroid cultures will only contain one cell type. Tumors collected by fine needle aspiration may also demonstrate a range of de-differentiation, particularly those from unresectable, widely metastatic, or advanced disease. Indeed, this is one of the clear benefits of FNA, that more aggressive lesions can be sampled than those that undergo surgical resection, However, de-differentiation or sarcomatoid transformation of the tumor can make distinction of tumor cells from fibroblasts more challenging. To help identify de-differentiated or sarcomatoid tumor cells, this protocol utilizes a stain for cytokeratin 8/18. In contrast to conventional AE1/3 staining, which detects both high- and low-molecular weight keratins, cytokeratin 8/18 staining is only for low-molecular weight keratins. Multiple studies suggest that cytokeratin 8/18 provides more sensitive detection of epithelial origin, and thus improved detection of more undifferentiated or spindled tumors[108-110]. However, a remaining limitation is that some highly spindled carcinomas and some myofibroblasts from bladder biopsies may still express low levels of smooth muscle actin and cytokeratin 8/18[111]. Fortunately, primary bladder FNAs are uncommon in clinical practice and are unlikely to be performed for research tissue acquisition.

2.5. METHOD: HIGH THROUGHPUT DRUG SCREENING OF FINE-NEEDLE ASPIRATION-DERIVED CANCER ORGANOIDS

2.5.1. Summary of Project and Contribution of Method

In generating our fine-needle aspiration-derived organoid model system, we had to adapt previously used methodologies to be amenable to these new cultures. This protocol presents a straightforward way to adapt organoids to 384-well plate formats for high-throughput imaging and viability measurement.

This work was published in *STAR Protocols* in December 2020, and the text contained in this subsection is adapted from:

Bergdorf, K., Phifer, C., Bharti, V., Westover, D., Bauer, J., Vilgelm, A., Lee, E., and Weiss, V. (2020). High-throughput drug screening of fine-needle aspiration-derived cancer organoids. STAR *Protocols 1*(3):100212.

2.5.2. Summary and Graphical Abstract

Generation of fine-needle aspiration (FNA)-derived cancer organoids has allowed us to develop a number of downstream applications. In this protocol, we start with organoids cultured in a semi-solid format. We dissociate organoids into single cells and then plate in a 384-well format for high-throughput drug screening. While this method must be fine-tuned for each individual organoid culture, it offers a format well-suited for rapidly screening medium sized drug/compound libraries (500-5,000 molecules) and generating dose-response curves to measure relative efficacy. For complete details on the use and execution of this protocol, please refer to Lee et al. (2.1) and Vilgelm et al. (2.2).

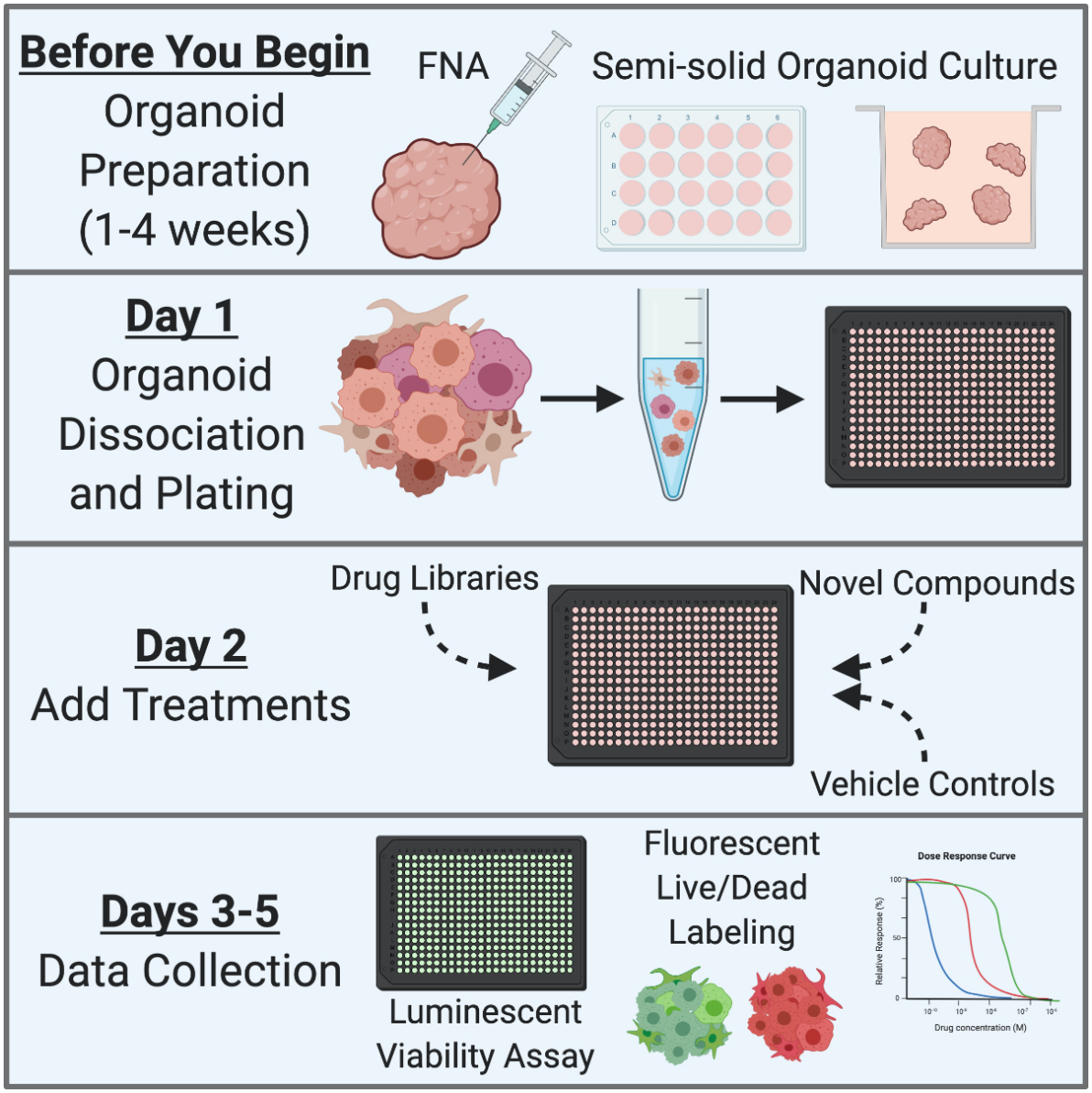

Figure 2.5.1. Graphical Abstract.

2.5.3. Preparation

2.5.3.1. Organoid Preparation

Fine-needle aspiration should be performed on the tumor tissue of interest per standard protocols and grown in a semi-solid format consisting of complete organoid media plus 5% Matrigel as described in Vilgelm et al. (2.2) and Phifer et al. (2.3). The number of cells needed is dependent on the growth rate of the organoids over 5 days. Slow-growing organoids will require more cells to be plated initially to preserve the time course of the experiment. We have found that for most cell lines, 12 wells of semi-solid organoid culture (3-10 organoids/well depending on organoid size) are sufficient to plate one 384-well plate.

2.5.4. Detailed Methods

2.5.4.1. Organoid Dissociation

While it would be optimal to plate intact organoids, issues with size inconsistency and fragility currently make this unrealistic to do in high-throughput. With dissociation into single cells, patient-derived cancer organoids can be easily plated and allowed to reform in each well of a 384-well plate.

2.5.4.1.1. Collect and wash organoids.

With a P1000 tip, pipette semi-solid cultures repetitively in a circular motion to break up the Matrigel. Transfer cultures to a 15mL conical tube. Centrifuge at 340 x g for 5 minutes at 20-25°C and aspirate media. This will be the standard centrifugation step for the remainder of the organoid dissociation. Wash pelleted organoids with 10mL cold PBS to remove any residual Matrigel or media, centrifuge, and aspirate as much PBS as possible without disturbing the pellet.

2.5.4.1.2. Dissociate organoids in TrypLE

Resuspend organoids in 5mL TrypLE and incubate at 37°C for 30 minutes, with vigorous pipetting every 10 minutes to break up cell clumps. If the organoids are large, you may need to pipette with a P1000 tip

every 5 minutes to enhance dissociation. When close to single cell suspension or small clumps, centrifuge as in 2.5.4.1.1. Aspirate TrypLE, then wash in warm modified DMEM media and centrifuge again.

2.5.4.2. Plating Organoids in a 384-well Format

Once dissociated, these cells can be plated with established cell suspension plating methods. We utilize two formats of plating, depending on the number of plates needed for the given experiment. The first, which involves plating by hand, is for a small number of plates (≤ 3) or for those who do not have access to high-throughput plating equipment. The other is automated and can be used for large-scale, high-throughput experiments.

2.5.4.2.1. Count cells and prepare media

Count cells and resuspend to a concentration of 9500cells/mL in complete DMEM + 2% Matrigel in a 50mL conical tube. We have successfully used 5% Matrigel as well but find that 2% is sufficient for our cultures and purpose. Using higher percentages of Matrigel, in combination with the optional centrifugation step following plating, may allow for enhanced downstream imaging. Although this is a low concentration of Matrigel, the cell suspension will still solidify at ambient temperature within minutes, if not kept on ice. The Matrigel should not be added until right before plating, and the cell suspension should be kept on ice prior to and while plating the cell suspension.

We have found that 285 cells per well is an ideal starting concentration for the majority of our organoids. However, for particularly slow-growing cultures, we have increased the number up to 1000 cells per well. We have not had to decrease the number of initial cells below 285/well for any of our cultures to date.

2.5.4.2.2. Plate cells

2.5.4.2.2.1. Large-scale plating

Equip BioTek EL406 peristaltic pump with a 10µL wide-bore tip cassette and set to low speed. Dead volume is the excess volume required by a liquid handling instrument. It can be an unusable portion (e.g., residual volume in labware that is not accessible to the instrument) or a used portion that is not

transferred to the assay container, such as the volume needed to prime tubing/tips. To decrease dead volume, reduce pre-dispense volume as much as possible. To decrease cross-well dispensing, minimize the height of the tips to the carrier to as low as 1mm. Dispense from tips should appear as a drop rather than a stream. Swirl the tube of cells prior to priming the tubing and before each plate to ensure equal suspension dispensing. Be careful not to introduce air bubbles. Dispense 30uL cell suspension per well into the cell-repellent microplates.

2.5.4.2.2.2. Smaller-scale experiments

Cells can be plated using a manual or electronic (repeating) multi-channel P200 pipette. Transfer the cell suspension + Matrigel to an appropriately sized reservoir for the volume size. If possible, place the reservoir on ice to prevent solidification. Avoid introducing bubbles into the media when pipetting.

Following cell plating, centrifuge the plate(s) at 220 x g for 1 minute to allow cells to be pushed toward the bottom of the well. This helps to bring the cells and clusters (along with the Matrigel) into similar z-planes, which helps to stabilize the cultures for both downstream applications of microscopy and/or refreshing media or adding reagents to the wells. Allow organoids to form for at least 24 hours in a 37°C, 5% CO2 incubator

2.5.4.2.3. Drug Screening

Once the organoids are plated, they can be used for a number of different screens. We have used this format for primary screening of a large drug library and collection of dose-effect data for multiple drugs in a single experiment. Likewise, this could be modified for functional genomics screens (eg, CRISPR, siRNA, etc.), phenotypic screening (eg, high-content imaging), or other cellular read outs or functional assays.

2.5.4.2.3.1. Adding compounds.

Dispense 10µL of treatment at 4X the desired concentration (bringing total well volume to 40µL) to wells of each plate, including replicates and appropriate vehicle controls. If using DMSO, maximum DMSO

concentration should be determined empirically for any organoid lines prior to drug screening. For all organoids we have screened to date, our DMSO concentrations do not exceed 0.1%.

For large screens, drug libraries may be “stamped” into organoid plates utilizing a Bravo automated pipette liquid transfer system, which holds a 384-well tip head to simultaneously dispense reagents from a drug source plate to each organoid plate within seconds. Drugs may also be added using a multi-channel pipette if necessary.

Incubate plates at 37°C, 5% CO2 for the desired treatment time (24-96 hours).

2.5.4.2.3.2. Data collection and analysis

Either method below can be used, however we do not recommend using both methods on the same cultures.

2.5.4.2.3.2.1. Fluorescent Imaging of Live/Dead Cells

24 hours prior to the end of drug treatment, add propidium iodide to a final concentration of 5ug/mL to the wells. Incubate at 37°C for 24 hours. Add Hoechst to the wells at a final concentration of 10ug/mL to the wells. Incubate at 37°C for 2 hours. Add Calcein AM to the wells at a final concentration of 5uM. Incubate for 1 hour and image with a fluorescence microscope.

2.5.4.2.3.2.2. CellTiter-Glo 3D

If desired, image organoids before adding CellTiter-Glo 3D. Using the Bravo liquid handler or a multichannel pipette, add 40µL CellTiter-Glo 3D to the wells and mix vigorously to break up and lyse organoids. Check the wells under a microscope following this step to ensure that all organoids have been broken up. Repeat vigorous pipetting as necessary until none remain.

Make sure not to introduce bubbles when mixing, as it will impact the readout from the plate reader and introduce errors in the data. Place plates on a plate shaker for 25 minutes (up to 800 RPM). Centrifuge the plates to eliminate any bubbles and to draw all liquid to the bottom of the well. Quantify luminescence with a plate reader.Determine drug effect by subtracting the control

luminescence from the treatment luminescence, then plot against drug concentration for each treatment using Excel or GraphPad Prism.

2.5.5. Discussion and Limitations

While this protocol has worked very well for the thyroid and melanoma organoid lines we have used, it may not work for every organoid line. Very large organoids are difficult to dissociate, due to low penetration of the TrypLE in 30 minutes. While the TrypLE can be left on longer, it may also cause cell death after prolonged exposure. This can also be an issue for organoids which are not facile; the TrypLE incubation may be too damaging for the cells to reform organoids and grow once plated. While we have not had any survival issues with our lines, a small sample of the culture should be tested with this protocol prior to plating an experiment to ensure that the cells can recover from dissociation.

As discussed in the protocol, the cell numbers listed herein are not concrete for every line. Some slow-growing lines need more cells initially to grow within the allotted experiment time. If you plan on doing a large screen with a line, we recommend plating one trial plate to observe the growth over the treatment period (3-5 days) with multiple initial cell numbers so that the experiment can be optimized for the individual line you are screening.

CHAPTER III

CHARACTERIZING DRIVERS OF THYROID CARCINOMA

3.1. CHARACTERIZING THE TUMOR-IMMUNE MICROENVIRONMENT IN PTC

3.1.1. Summary of Project and Contribution of Study

Prior to these studies, the drivers of papillary to anaplastic thyroid carcinoma transformation have been poorly defined. This is partially due to a lack of understanding of both PTC and ATC beyond mutational status. In this project, we used data from The Cancer Genome Atlas and immune deconvolution programs to define the immune landscape of thyroid tumors. Unfortunately, none of the tumors available via TCGA are ATCs. However, there is a spectrum of PTCs, from indolent to the aggressive tall cell variant. We also characterize the association of immunophenotypes to mutational status and tumor and lymph node staging. This work has already contributed to multiple follow-up studies, including characterization of the immune landscape in our in-house cohort of over 300 thyroid cancer patients. This cohort includes many histotypes, including ATC.

This work was published in *Endocrine-Related Cancer* in June 2019, and this subsection is adapted from:

Bergdorf, K., Ferguson, D., Mehrad, M., Ely, K., Stricker, T., and Weiss, V. (2019). Papillary thyroid carcinoma behavior: clues in the tumor microenvironment. *Endocrine-Related Cancer 26*(6): 601-614.

3.1.2. Abstract

The prevalence of thyroid carcinoma is increasing and represents the most common endocrine malignancy, with papillary thyroid carcinoma (PTC) being the most frequent subtype. The genetic alterations identified in PTCs fail to distinguish tumors with different clinical behaviors, such as extra-thyroidal extension

and lymph node metastasis. We hypothesize that the immune microenvironment may play a critical role in tumor invasion and metastasis. Computational immunogenomic analysis was performed on 568 PTC samples in The Cancer Genome Atlas using both CIBERSORT and TIMER deconvolution analytic tools for characterizing immune cell composition. Immune cell infiltrates were correlated with histologic type, mutational type, tumor pathologic T stage, and lymph node N stage. Dendritic cells (DCs) are highly associated with more locally advanced tumor T stage [T3/T4, Odds Ratio (OR)=2.6, Confidence Interval (CI)=1.4-4.5, p=5.4 x 10-4]. Increased dendritic cells (OR=3.4, CI=1.9-6.3, p=5.5 x 10-5) and neutrophils (OR=10.5, CI=2.7-43, p=8.7 x 10-4) significantly correlate with lymph node metastasis. In addition, dendritic cells positively correlate with tall cell morphology (OR=4.5, CI=1.6-12, p=4.9 x10-3) and neutrophils negatively correlate with follicular morphology (OR=0.0013, CI=5.3 x 10-5-0.031, p=4.1 x 10-5). TIDE analysis indicates an immune-exclusive phenotype that may be mediated by increased galectin-3 found in PTCs. Thus, characterization of the PTC immune microenvironment using two computational immunogenomic platforms shows that specific immune cells correlate with mutational type, histologic type, local tumor extent, and presence of lymph node metastasis. Immunologic evaluation of PTCs may provide a better indication of biologic behavior, resulting in improvement in the diagnosis and treatment of thyroid cancer.

3.1.3. Introduction

Morphologic assessment and mutational analysis of the primary thyroid cancer fails to predict the likelihood of metastatic or recurrent disease. The behavior of many tumors is impacted by the tumor immune microenvironment. The thyroid tumor immune microenvironment may play an important role in tumor behavior and may be able to provide clues for improved treatments.

Current studies on the immune microenvironment of thyroid tumors are often contradictory. Generally, tumor infiltrating lymphocytes are known to enhance tumor immunity. However, studies in thyroid cancer have shown variable prognostic significance Dendritic cells (DCs) are also traditionally thought to have an important

role in antigen presentation and tumor-immunity. However, there exist subsets of DCs that are immunosuppressive and enhance tumor growth[112-117]. In the thyroid, DCs are increased in papillary thyroid carcinomas (PTCs) over benign parenchyma[116,118,119]. However, it is unclear whether these DCs are beneficial in the tumor microenvironment. Tumor associated macrophages (TAMs) are generally thought to be tumor enhancing, which is supported in thyroid studies that suggest they are present in more aggressive tumors[115,116,120-122]. Finally, neutrophils have recently been shown to enhance metastatic disease[123-125]. Currently, it is unknown whether they play a role in thyroid cancer.

The development of The Cancer Genome Atlas (TCGA) in 2006 provided the scientific community with a unique view into many aspects of tumor biology, including the patient immune response. Recent TCGA evaluation of the thyroid immune microenvironment suggests that certain subsets of aggressive tumors are immunologically distinct[126,127]. In this paper, we present the first evaluation of a large thyroid tumor cohort of 568 PTCs from TCGA that defines the key immune cell infiltrates within the tumor microenvironment that may be involved in aggressive tumor behavior. Identification of the specific infiltrates associated with aggressive features will lead to improved and targeted immunotherapy for the treatment of aggressive thyroid carcinomas.

3.1.4. Materials and Methods

3.1.4.1. TCGA Computational Analysis

The results presented here are based upon data generated by the TCGA Research Network (http://cancergenome.nih.gov/). Computational immunogenomic analysis was performed on RNA sequencing data from 568 PTCs in TCGA. Mutational data was available for 502 PTCs in TCGA. Patient characteristics are presented in Table 3.2.1. The CIBERSORT deconvolution analytic tool for characterizing cellular composition[128] calculates immunologic cell fractions for 22 hematopoietic cell types such that all of the individual fractions for each immune cell type sum to 1 (https://cibersort.stanford.edu/). For each tumor, CIBERSORT calculated a global p-value for the immune cell fraction result based on the statistical probability of the presence of immune

cells in the sample. All samples, regardless of the p value, were included in this analysis. Even those samples with p-value >0.05 may be important, as they may represent samples with low immune cell infiltrate. Of note, the CIBERSORT program normalized the data in relative space, so that the immune cell fractions combined were equal to 1. CIBERSORT has a default recommend 100 permutations and quantile normalization for RNA sequencing data was disabled as recommended. The second analytic tool used was the Tumor Immune Estimation Resource, TIMER, which is another deconvolution analytic tool that calculates the abundance of 6 immune cell types (B cells, CD4+ T cells, CD8+ T cells, neutrophils, macrophages, and dendritic cells; https://cistrome.shinyapps.io/timer/)[129,130]. All 568 TCGA PTCs were included in this analysis. TIMER has built in normalization and permutations, and thyroid cancer was the selected tumor type. Finally, the TIDE (Tumor Immune Dysfunction and Exclusion) analytic tool was used for analysis of responsiveness to checkpoint inhibitor therapies, as well as T cell exclusion and T cell dysfunction analysis (http:// http://tide.dfci.harvard.edu/)[131]. TIDE requires that each gene be normalized prior to upload. This normalization was performed on the data per TIDE's documentation recommendations.

Clinicopathologic characteristics evaluated for these patients include age at diagnosis, histologic subtype, tumor pathologic T stage, lymph node (LN) N stage, and mutational analysis. Staging was based on the American Joint Committee on Cancer 7th Edition. The mutations evaluated include some of the most commonly mutated genes in the TCGA data (502 PTCs); however, only BRAF and RAS mutations were frequent enough in this study to perform downstream analysis of that mutational subgroup (Table 3.2.1).

GEPIA, the Gene Expression Profiling Interactive Analysis tool, was used to generate boxplots of LGALS3 expression from the THCA dataset compared to TCGA data from normal (non-tumor) TCGA and GTEx data. The |Log2FC| cutoff was set at 1 and the p-value cutoff was 0.01.

Table 3.1.1. Summary of patient characteristics.

	With Mutation Data (N=502)	Without Mutation Data (N=568)
Patient Characteristics	**Number of Patients (%)**	**Number of Patients (%)**
Average age	47	47
Age range	15-89	15-89
Number male	129 (26%)	149 (26%)
Number female	352 (70%)	396 (70%)
Gender unknown	21 (4%)	23 (4%)
Morphologic Type	**Number of Tumors**	**Number of Tumors**
Classical histotype	339 (68%)	393 (69%)
Follicular histotype	98 (19%)	105 (18%)
Tall cell histotype	35 (7%)	38 (7%)
Other/Unknown histotype	30 (6%)	32 (6%)
Mutational Status	**Number of Tumors**	**Number of Tumors**
BRAF	291 (58%)	N/A
RAS	45 (9%)	N/A
Neither	169 (33%)	N/A
Tumor Stage	**Number of Tumors**	**Number of Tumors**
T1/2	293 (58%)	314 (55%)
T3/4	186 (37%)	229 (40%)
Unknown	23 (5%)	25 (5%)
Lymph Node Stage	**Number of Tumors**	**Number of Tumors**
No LN involvement	223 (44%)	243 (43%)
LN involvement	212 (42%)	251 (44%)
Unknown	67 (14%)	74 (13%)
Distant Metastases	11	14
Patients Deceased	14	18

3.1.4.2. Statistical Analysis

Logistic regression was conducted to analyze associations between the immune cell fractions with mutational status, tumor pathologic T stage and lymph node N stage. For all TIMER analyses, all 6 immune cell types (dendritic cells, CD8 T cells, CD4 T cells, macrophages, B cells, and neutrophils) were included as co-variates. For CIBERSORT, 15/22 immune cell types (naïve B cells, memory B cells, plasma cells, CD8 T cells, resting CD4 memory T cells, activated CD4 memory T cells, follicular helper T cells, regulatory T cells, gamma delta T cells, M0 macrophages, M1 macrophages, M2 macrophages, resting dendritic cells, activated dendritic cells, and neutrophils) were included as co-variates corresponding to the major immune cells types identified in TIMER. Naïve CD4 T cells were excluded from CIBERSORT analyses because the value was 0 for all 568 PTCs. Mast cells, eosinophils, monocytes, and NK cells were excluded from CIBERSORT analyses since these infiltrates could not be confirmed using the TIMER deconvolution tool. The CIBERSORT immune cell fractions were converted to percentages prior to analysis. For each immune cell type we performed a multivariate logistic regression with the infiltrates as continuous variables. No adjustments were made for multiple statistical testing. The odds ratio is presented as a 1% increase in immune cell fraction for CIBERSORT and a one-unit increase in the infiltration level for TIMER. Morphologic subtype was also included as a co-variate for mutational analyses and stage analyses and is presented in the supplemental data.

For the dependent variables, pathologic tumor T stage was divided into low (T1 and T2) and high (T3 and T4) stage and was treated as a dichotomous variable. This distinction was made based on tumor size >4cm and/or the presence of extra-thyroidal extension (T3 and T4) versus smaller size with the absence of extra-thyroidal extension (T1 and T2). For the LN stage, this category was classified as no metastasis (N0) or presence of LN metastasis (>N0) and treated as a dichotomous variable.

Multinomial logistic regression was used for analysis of morphologic subtypes, as histologic types are not a binary classification. This analysis used classical PTC histology as the baseline category. The same immunologic covariates were used for this analysis.

Downstream analysis of the activated dendritic cell high and activated dendritic cell low cohorts were performed using a subset of samples with CIBERSORT p-value value <0.05, as these represent samples with absolute immune infiltration that is not close to zero (131 samples). Genes with a mean expression of less than log2 FPKM = 2.5 were removed. Surrogate Variable Analysis was performed on the resulting gene expression matrix, and then surrogate variables were regressed from the gene expression matrix. Differential gene expression was then determined using a gene by gene linear model of the form y~DC_status+BRAF_status, where DC_status = high or low DC as a factor, and BRAF_status = mutated or non-mutated as a factor. False discovery rate was controlled by FDR using the qvalue package in R. Pathway analysis was performed using DAVID (https://david.ncifcrf.gov/) and ensembl gene names. Heatmaps were produced in R using heatmap.2.

3.1.4.3. Institutional Patient Selection and Analysis for Immunohistochemistry

An additional cohort of patients was collected from Vanderbilt University Medical Center archives to confirm the TCGA computational analysis. In this Institutional Review Board approved study, files from 2008-2017 containing diagnoses of papillary thyroid carcinoma (PTC, N=20), follicular variant of PTC (FVTPC, N=12), and non-invasive follicular thyroid neoplasm with papillary-like nuclear features (NIFTP, N=11) resection diagnoses were identified. H&E sections from surgical resection specimens were reviewed by three pathologists with head and neck expertise (KE, MM, VW) to confirm the histopathologic diagnoses. Some historic encapsulated FVPTC cases were re-classified as NIFTP based on the criteria proposed by Nikiforov et al[132]. Only lesions that were entirely submitted for histologic evaluation were included. When there was disagreement among the pathologists, a fourth head and neck specialist was consulted.

3.1.4.4. Immunohistochemistry

Four micron sections from 11 NIFTPs and 12 FVPTCs were evaluated by hematoxylin and eosin (H&E) and immunohistochemistry (IHC) for expression of Galectin-3 (GAL3, sc-23938, Santa Cruz Biotechnology, 1:1000 dilution). Four micron sections from 20 classical PTCs were evaluated by hematoxylin and eosin (H&E) and immunohistochemistry (IHC) for expression of FoxP3 (236A/E7, eBioscience, Inc., 1:100 dilution), CD8

(MM39-10, StatLab), and CD4 (PA0427, Leica). IHC staining was performed according to manufacturer's protocols. Unstained slides were first deparaffinized by routine methods. For antigen retrieval, slides were heated in citrate buffer (pH 6.0) at 100˚C for 20 minutes or in EDTA (pH 9.0) at 98ºC for 20 minutes, followed by a 10-minute cool down to room temperature. All slides were then quenched with 0.03% (v/v) H2O2 with NaN3 for 5 minutes. Slides were blocked for 20 minutes with serum-free protein block (Dako, Carpinteria, CA), followed by application of primary antibodies. Slides were then incubated with Evision+HRP-labeled polymer (Dako) for 30 minutes, followed by 5 minute incubation with DAB (Dako). Immunohistochemical stains were evaluated and scored on a scale of 0-3 for maximum intensity of staining. The pattern of GAL3 staining was categorized as subcapsular or diffuse, and analysis was performed using 2 x 3 Fisher's Exact Tests. The pattern of CD8, CD4, and FoxP3 was categorized as intra-tumoral or peripheral.

3.1.5. Results

3.1.5.1. Immunologic cell fraction characterization and correlation with histology and mutational status

We hypothesized that different PTC histopathologic subtypes would have different compositions of immune cell infiltration. We therefore chose two publicly available computational tools to estimate the specific immune cell types present in each tumor within the Cancer Genome Atlas Cohort (N=568 PTCs). These two computational tools, CIBERSORT and TIMER, use RNA sequencing data to estimate the immune infiltrate in each sample using unique gene signatures, determined by the creators of each tool. CIBERSORT calculates the immune cell fractions of 22 unique immune cells subtypes and normalizes the data such that all fractions sum to 1. TIMER calculates the immune cell infiltrate of 6 unique immune cell subtypes.

Using classical histology as the baseline category, CIBERSORT data demonstrated that the more clinically indolent follicular variant histology had a significant negative correlation with tumor associated macrophages (M0: OR=0.93, CI=0.89-0.96, p=1.3 x 10-5; M1: OR=0.91, CI=0.83-0.99, p=0.023) and DCs (resting: OR=0.90, CI=0.85-0.95, p=3.1 x 10-4; activated: OR=0.86, CI=0.76-0.97, p=0.014). Analysis of CIBERSORT data also

indicated that the more clinically aggressive tall cell variant had a slight positive correlation with the resting DC fraction (OR=1.1, CI=0.1.0-1.2, p=0.042). TIMER data analysis demonstrated a negative correlation between follicular variant histology and immune infiltrate including DCs (OR=0.057, CI=0.019-0.18, p=5.1 x 10-7), CD8 T cells (OR=0.22, CI=0.08-0.61, p=0.0034), and neutrophils (OR=0.0013, CI=5.3 x 10-5-0.031, p=4.1 x 10-5). Similar to CIBERSORT, TIMER showed the more clinically aggressive tall cell variant of PTC to be positively correlated with DCs (OR=4.5, CI=1.6-12, p=4.9 x10-3; Table 3.2.2.).

Table 3.1.2. CIBERSORT and TIMER Results by Histotype

CIBERSORT			
FOLLICULAR VARIANT PTC			
Cell Type	**OR**	**95% CI**	**p value**
Naïve B cells	0.95	0.90-1.0	0.038
Memory B cells	0.93	0.82-1.1	0.26
Plasma cells	0.97	0.92-1.0	0.38
CD8 T cells	1.0	0.97-1.1	0.71
Resting CD4 memory T cells	0.97	0.93-1.0	0.23
Activated CD4 memory T cells	0.65	0.41-1.0	0.068
Follicular helper T cells	1.1	0.97-1.1	0.25
Regulatory T cells	0.96	0.87-1.1	0.40
Gamma delta T cells	0.96	0.86-1.1	0.45
M0 macrophages	0.93	0.89-0.96	1.3×10^{-5}
M1 macrophages	0.91	0.83-0.99	0.023
M2 macrophages	1.0	0.96-1.0	1.0
Resting dendritic cells	0.90	0.85-0.95	3.1×10^{-4}
Activated Dendritic cells	0.86	0.76-0.97	0.014
Neutrophils	0.53	0.22-1.3	0.16
TALL CELL VARIANT PTC			
Cell Type	**OR**	**95% CI**	**p value**
Naïve B cells	1.0	0.97-1.1	0.27
Memory B cells	0.90	0.72-1.1	0.36
Plasma cells	1.0	0.93-1.1	0.71
CD8 T cells	0.93	0.85-1.0	0.12
Resting CD4 memory T cells	1.0	0.92-1.1	0.97
Activated CD4 memory T cells	1.2	0.83-1.7	0.36
Follicular helper T cells	0.98	0.86-1.1	0.70
Regulatory T cells	1.1	1.0-1.3	0.071
Gamma delta T cells	0.85	0.65-1.1	0.25
M0 macrophages	1.0	0.95-1.1	0.80
M1 macrophages	1.1	0.91-1.2	0.50
M2 macrophages	0.94	0.87-1.0	0.16
Resting dendritic cells	1.1	1.0-1.2	0.042
Activated Dendritic cells	0.97	0.82-1.1	0.72
Neutrophils	1.85	0.86-4.0	0.12
TIMER			
FOLLICULAR VARIANT PTC			
Cell Type	**OR**	**95% CI**	**p value**
DCs	0.057	0.019-0.18	5.1×10^{-7}

CD8 T cells	0.22	0.080-0.61	0.0034
CD4 T cells	0.14	0.0066-3.1	0.21
Macrophages	0.58	0.13-2.6	0.48
B cells	0.33	0.11-1.1	0.063
Neutrophils	0.0013	0.000053-0.031	4.1×10^{-5}
TALL CELL VARIANT PTC			
Cell Type	**OR**	**95% CI**	**p value**
DCs	4.5	1.6-12	4.9×10^{-3}
CD8 T cells	0.50	0.13-1.9	0.32
CD4 T cells	0.15	0.0018-12	0.40
Macrophages	0.60	0.020-18	0.77
B cells	1.1	0.19-5.9	0.94
Neutrophils	4.5	0.51-39	0.17

Next, we assessed the immune fractions in relation to BRAF and RAS mutational status (Table 3.2.3.). Evaluation of the 502 PTCs using CIBERSORT indicated that BRAF mutational status correlated with increased immune cell fractions for naïve B cells, regulatory T cells, macrophages, and dendritic cells. Follicular helper T cells negatively correlated with BRAF mutation. In contrast, RAS mutants correlated with decreased immune cell fractions of naïve B cells, macrophages, and dendritic cells. CD8 T cells and follicular helper T cells showed a positive correlation with RAS mutations. Similarly, TIMER indicated that BRAF mutational status correlated with significantly increased DCs, CD8 T cells, macrophages, B cells, and neutrophils. In contrast, RAS mutation correlated with significantly decreased DCs, CD8 T cells, CD4 T cells, B cells, and neutrophils (Table 3.2.3). These data were also analyzed to include morphologic subtype as a co-variate with the majority of immune cell types listed above remaining significantly correlated with mutational status. Overall, these data demonstrate that BRAF-mutant tumors are generally immune cell rich, while RAS-mutant tumors are immune cell poor.

Table 3.1.3. CIBERSORT and TIMER Results by Mutational Status

CIBERSORT			
BRAF MUTATION			
Cell Type	**OR**	**95% CI**	**p value**
Naïve B cells	1.1	1.1-1.2	5.2×10^{-5}
Memory B cells	0.98	0.89-1.1	0.73
Plasma cells	1.0	1.0-1.1	0.13
CD8 T cells	0.98	0.94-1.0	0.21
Resting CD4 memory T cells	1.0	0.99-1.1	0.13
Activated CD4 memory T cells	1.3	0.95-1.7	0.13
Follicular helper T cells	0.92	0.86-0.98	0.014
Regulatory T cells	1.1	1.0-1.2	0.0038
Gamma delta T cells	1.0	0.93-1.1	0.64
M0 macrophages	1.1	1.0-1.1	3.9×10^{-4}
M1 macrophages	1.1	1.1-1.2	7.5×10^{-4}
M2 macrophages	1.0	0.99-1.1	0.20
Resting dendritic cells	1.1	1.1-1.1	3.8×10^{-5}
Activated Dendritic cells	1.2	1.1-1.3	7.8×10^{-4}
Neutrophils	0.76	0.39-1.3	0.39
RAS MUTATION			
Cell Type	**OR**	**95% CI**	**p value**
Naïve B cells	0.89	0.80-0.98	0.028
Memory B cells	0.92	0.76-1.1	0.39
Plasma cells	0.95	0.85-1.1	0.38
CD8 T cells	1.1	1.0-1.1	0.0039
Resting CD4 memory T cells	1.1	0.99-1.1	0.10
Activated CD4 memory T cells	0.33	0.044-0.88	0.13
Follicular helper T cells	1.13	1.0-1.3	0.027
Regulatory T cells	1.1	0.96-1.2	0.20
Gamma delta T cells	1.1	0.96-1.2	0.15
M0 macrophages	1.0	0.98-1.1	0.55
M1 macrophages	0.87	0.76-0.98	0.023
M2 macrophages	1.1	1.02-1.1	0.0069
Resting dendritic cells	0.92	0.83-0.99	0.045
Activated Dendritic cells	0.84	0.71-0.96	0.023
Neutrophils	0.98	0.50-1.8	0.94
TIMER			
BRAF MUTATION			
Cell Type	**OR**	**95% CI**	**p value**
DCs	42	19-101	5.7×10^{-11}

CD8 T cells	7.3	3.4-17	1.1×10^{-6}
CD4 T cells	0.7	0.07-6.7	0.75
Macrophages	12	3.0-52	6.1×10^{-4}
B cells	3.1	1.1-9.0	0.038
Neutrophils	32	6.2-181	1.1×10^{-5}
RAS MUTATION			
Cell Type	**OR**	**95% CI**	**p value**
DCs	0.008	0.0007-0.05	1.0×10^{-5}
CD8 T cells	0.04	0.005-0.2	6.2×10^{-4}
CD4 T cells	0.001	3.0×10^{-6}-0.2	0.019
Macrophages	0.5	0.08-2.6	0.39
B cells	7.14×10^{-6}	5.7×10^{-10}-0.0056	0.0032
Neutrophils	0.001	6.0×10^{-6}-0.09	0.0070

Finally, we evaluated the TCGA data to investigate the relationship between immune cell infiltrates in the tumor microenvironment and age, gender, survival, and tumor mutational burden (TMB). There was no correlation between gender and immune infiltration. Increasing age correlated with an overall decreased immune infiltrate. Survival assessment using a Cox proportional hazard model with the immune infiltrates as co-variates showed no statistical significance. Overall PTCs in the TCGA had a very low TMB of <1mutation/Mb. In the TCGA PTCs, there was no correlation between infiltration of immune cell subtypes and total mutations.

3.1.5.2. Infiltrates and pathologic tumor stage in PTCs

We next evaluated whether changes in immune infiltrates were associated with pathologic tumor T stage (Figure 3.2.1, Table 3.2.4., N=568). CIBERSORT demonstrated increased activated DCs in tumors with more locally advanced tumor T stage (OR=1.2, CI=1.1-1.3, p=3.7 x 10-5, using the American Joint Committee on Cancer 7th Edition) and decreased follicular helper T cells (TFH) with more locally advanced T stage (OR=0.9, CI=0.87-0.98, p=0.013). TIMER analysis generated similar results, with increased DCs associating with advanced T stage (OR=2.6, CI=1.4-4.5, p=5.4 x 10-4, Figure 3.2.1., Table 3.2.4.). Using TIMER, there was no significant correlation with CD4 T cells and tumor T stage.

CIBERSORT showed a slight correlation between tumor associated macrophages and tumor T stage, but the significance is unclear with an odds ratio of 1. While there have been several reports of a correlation between tumor associated macrophages and tumor immunity[133,134]. TIMER did not confirm an association between macrophages and tumor stage. These data were also analyzed to include morphologic subtype as a co-variate with all the immune cell types listed above remaining significantly correlated with mutational status.

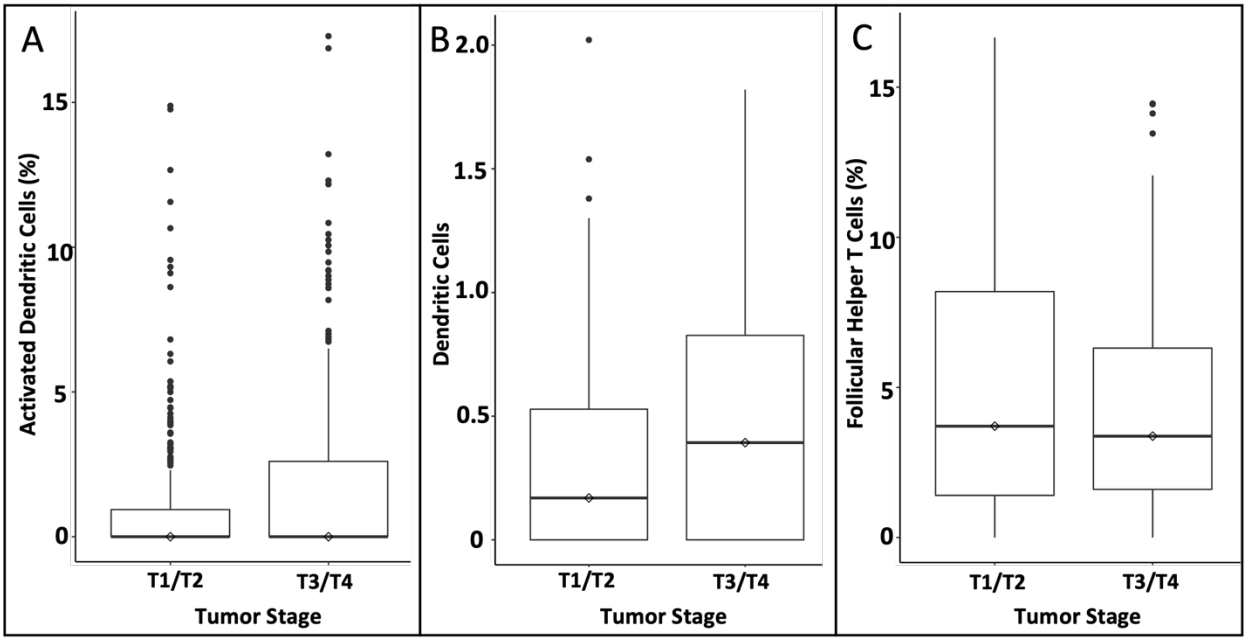

Figure 3.1.1. Distribution of immune cell infiltrate and pathologic tumor T stage. A. CIBERSORT distribution of activated dendritic cell fractions in low T stage (T1/T2) and high T stage (T3/T4) tumors. B. TIMER distribution of dendritic cell fractions in low T stage (T1/T2) and high T stage (T3/T4) tumors. C. CIBERSORT distribution of follicular helper T cell fractions in low T stage (T1/T2) and high T stage (T3/T4) tumors.

Table 3.1.4. Correlation of immune infiltrate and pathologic tumor stage.

CIBERSORT ANALYSIS			
T Stage	**OR**	**95% CI**	**p value**
Naïve B cells	1.0	0.98-1.1	0.24
Memory B cells	1.0	0.91-1.1	0.86
Plasma cells	1.0	0.94-1.0	0.67
CD8 T cells	1.0	0.98-1.1	0.35
Resting CD4 memory T cells	1.0	0.97-1.0	0.87
Activated CD4 memory T cells	1.0	0.77-1.2	0.75
Follicular helper T cells	0.9	0.87-0.98	0.013
Regulatory T cells	1.0	0.93-1.1	0.96
Gamma delta T cells	1.0	0.90-1.1	0.65
M0 macrophages	1.0	0.98-1.0	0.59
M1 macrophages	1.0	0.94-1.1	0.87
M2 macrophages	1.0	0.93-1.0	0.029
Resting dendritic cells	1.0	0.96-1.0	0.81
Activated Dendritic cells	1.2	1.1-1.3	3.7×10^{-5}
Neutrophils	0.8	0.45-1.4	0.45
TIMER ANALYSIS			
T Stage	**OR**	**95% CI**	**p value**
DCs	2.6	1.4-4.5	5.4×10^{-4}
CD8 T cells	0.9	0.50-1.6	0.73
CD4 T cells	2.3	0.32-16	0.41
Macrophages	0.9	0.28-3.3	0.96
B cells	0.8	0.31-1.7	0.50
Neutrophils	1.6	0.45-5.4	0.47

3.1.5.3. Infiltrates and pathologic lymph node stage in PTCs

Another important factor in thyroid cancer management and treatment is the presence of LN metastasis. Using CIBERSORT (N=568), resting DCs showed a slight positive correlation with LN metastasis (OR= 1.1, CI= 1.0-1.1, p=0.019). TIMER confirmed the presence of significantly increased DCs in tumors with LN metastasis (OR= 3.4, CI= 1.9-6.3, p=5.5 x 10-5) and also demonstrated increased CD8 T cells (OR= 2.1, CI=1.1-4.0, p=0.029) and robust neutrophil infiltrate (OR= 10.5, CI= 2.7-43, p=8.7 x 10-4) in tumors with LN metastases (Figure 3.2.2, Table 3.2.5.). CIBERSORT did not show a significant correlation with CD8 T cells. A slight correlation was seen with naïve B cells and M0 macrophages using CIBERSORT, but TIMER failed to confirm any B cell or macrophage association. These data were also analyzed to include morphologic subtype as a co-variate and found that for CIBERSORT Naïve B cells remained significantly correlated with LN stage and for TIMER DCs and Neutrophils remained significantly associated with LN stage.

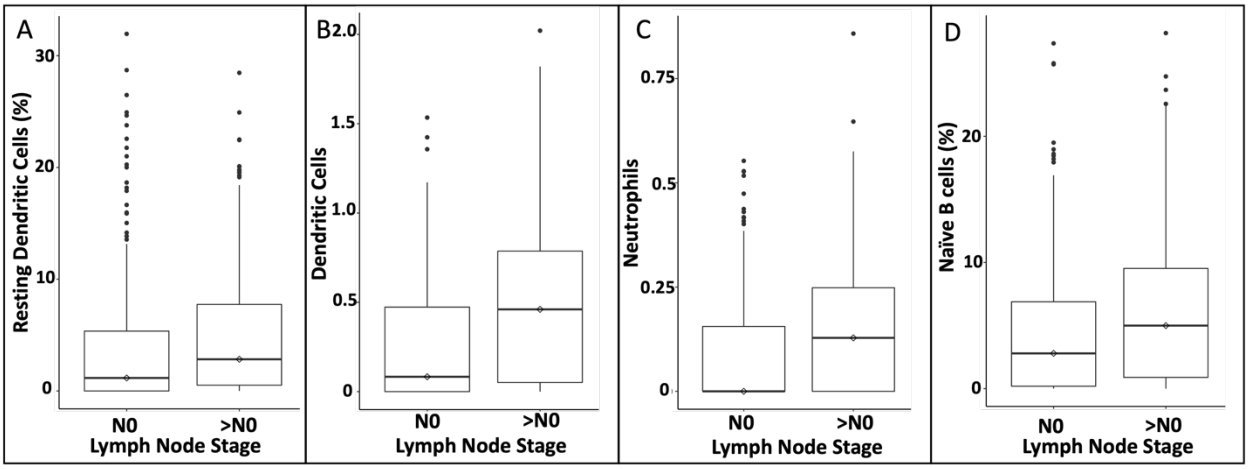

Figure 3.1.2. Distribution of immune cell fractions in tumors without (N0) and with (>N0) lymph node metastases. A. CIBERSORT distribution of resting dendritic cells in tumors without (N0) and with (>N0) lymph node metastasis. B. TIMER distribution of dendritic cells in tumors without (N0) and with (>N0) lymph node metastasis. C. TIMER distribution of neutrophils in tumors without (N0) and with (>N0) lymph node metastasis. D. CIBERSORT distribution of naïve B cells in tumors without (N0) and with (>N0) lymph node metastasis.

Table 3.1.5. Correlation of immune infiltrate and pathologic lymph node stage

CIBERSORT ANALYSIS			
LN Stage	**OR**	**95% CI**	**p value**
Naïve B cells	1.1	1.0-1.1	5.2×10^{-4}
Memory B cells	1.1	0.97-1.2	0.16
Plasma cells	1.0	0.98-1.1	0.30
CD8 T cells	1.0	0.96-1.0	0.83
Resting CD4 memory T cells	1.0	0.99-1.1	0.20
Activated CD4 memory T cells	1.0	0.78-1.2	0.82
Follicular helper T cells	1.0	0.96-1.1	0.55
Regulatory T cells	1.0	0.92-1.1	0.91
Gamma delta T cells	1.1	0.97-1.2	0.18
M0 macrophages	1.0	1.0-1.1	0.021
M1 macrophages	1.0	0.94-1.1	0.89
M2 macrophages	1.0	0.97-1.0	0.87
Resting dendritic cells	1.1	1.0-1.1	0.019
Activated Dendritic cells	1.1	0.99-1.2	0.076
Neutrophils	1.9	1.0-4.1	0.067
TIMER ANALYSIS			
LN Stage	**OR**	**95% CI**	**p value**
DCs	3.4	1.9-6.3	5.4×10^{-5}
CD8 T cells	2.1	1.1-4.0	0.029
CD4 T cells	0.69	0.087-5.4	0.72
Macrophages	0.58	0.15-2.2	0.43
B cells	2.3	1.0-5.7	0.054
Neutrophils	10.5	2.7-43	8.7×10^{-4}

3.1.5.4. Immune Suppression and Exclusion in PTCs

Tumor Immune Dysfunction and Exclusion (TIDE) analysis[131] was performed on the TCGA cohort of 502 PTCs. TIDE is another publicly available bioinformatics tool that uses RNA sequencing data to assess the immune infiltration of a given tumor based on gene expression. This tool generates information on the patient's susceptibility to checkpoint inhibitor therapies, the T cell exclusion status of the tumor, and the T cell dysfunction/exhaustion present in a tumor. The overall TIDE score predicts the susceptibility of the tumor to immune checkpoint blockade (Figure 3.2.3.A). Of the TCGA PTCs, 93% (469/502) were determined unlikely to respond to current checkpoint blockade therapies. Interestingly, only 9.2% (46/502) of the tumors had gene signatures indicating T cell dysfunction (Figure 3.2.3.B), while 95% (477/502) exhibited expression profiles consistent with T cell exclusive phenotype (Figure 3.2.3.C).

It is important to note that TIDE is currently only validated for melanoma and non-small cell lung cancer. In order to validate the computational findings of TIDE, we aimed to confirm these results by performing IHC on a cohort of 20 classical PTCs at Vanderbilt University Medical Center. We confirmed this phenomenon of T cell exclusion in our cohort of 20 classical PTCs using CD8, CD4, and FoxP3 immunohistochemistry. When observing the peripheral edge of each sample, 60% (12/20) demonstrated dense CD8 positivity, 90% (18/20) demonstrated dense CD4 positivity, and 85% (17/20) demonstrated dense FoxP3 positivity (Figure 3.2.3.D). The center of the tumor in the 20 PTCs analyzed was generally lymphocyte-poor. These VUMC data in combination with the TCGA TIDE data indicate that functional T cells are present in the tumor microenvironment but are primarily located around the margins of the tumor, often with predominant lymphoid aggregates. We hypothesized that factors produced by the tumor cells, particularly at the tumor margins, were mediating this immune-exclusion phenomenon.

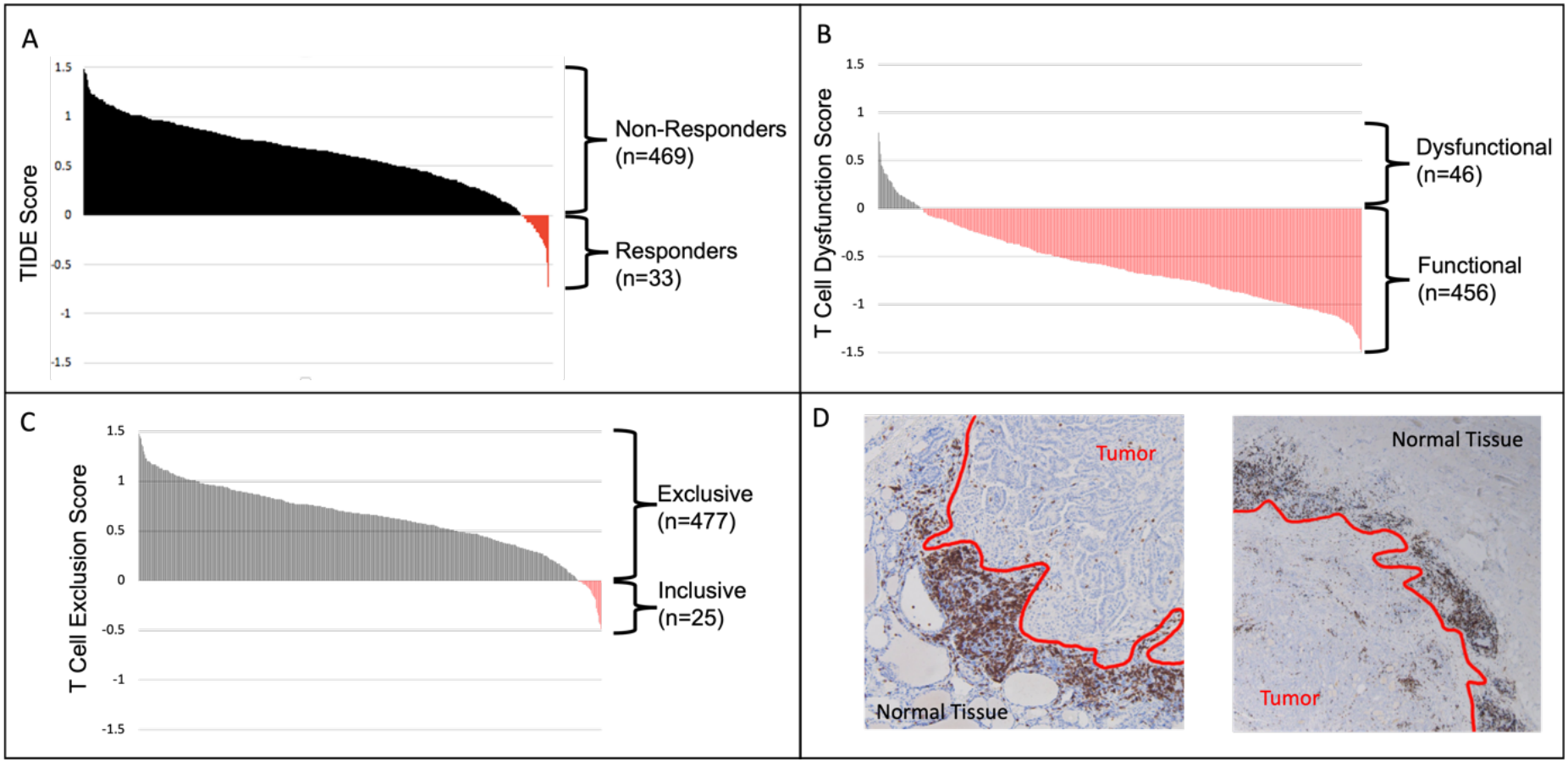

Figure 3.1.3. Tumor immune dysfunction and exclusion (TIDE) analysis. A. Overall TIDE scores and predicted tumor response to checkpoint blockade. B.TIDE dysfunction score. DS>0 indicates T cell dysfunction, DS<0 indicates functional T cells. C. TIDE T cell exclusion score. ES>0 indicates an T cell exclusive tumor, ES<0 indicates a T cell inclusive tumor. D. IHC of patient tumors, with CD8+ T cells shown in black.

3.1.5.5. Galectin 3 Potentially Mediates T Cell Exclusion in PTCs

Having demonstrated a significant correlation between DC infiltration and thyroid cancer histology/stage, we next investigated which genes were differentially expressed between the DC high and DC low groups. The TCGA thyroid expression data were subset for samples that had a significant ($p<0.05$) CIBERSORT score (in order to ensure inclusion of tumors with an immune infiltrate), and 805 genes differentially expressed between low activated DCs and high activated DCs were identified (FDR < 0.05). A DAVID analysis bioinformatics tool was then chosen to evaluate these differentially expressed genes. DAVID analyses are ideal for large gene sets and are designed to systematically extract meaningful biological data from large sets of gene expression. DAVID analysis of these genes showed enrichment for pathways involved in immunity (top cluster, Enrichment score=9.9, Figure 3.2.4.A). Interestingly, a heatmap of the genes in these immunity signatures showed that high activated DC samples tended to have low expression of these genes, while samples with low activated DC have high expression (Figure 3.2.4.B). This result suggested that the DC signature is associated with an immune-exclusive or immunosuppressive milieu. A similar analysis was performed for samples with high and low TFH, identifying 1149 differentially expressed genes (FDR<0.05). DAVID analysis of these genes also showed enrichment for pathways involved in immunity (top cluster, Enrichment score=11.1). A heatmap of the genes in these immunity signatures showed that high TFH samples tended to have high expression of these genes, while samples with low TFH have low expression (Figure 3.2.4.C). One of the differentially expressed genes in our DC immunity signature was lymphocyte-activation gene 3 (LAG3) (FDR, 0.0004). Galectin 3 (GAL3, encoded by LGALS3) is expressed on many cell types throughout the body, is highly expressed by many thyroid cancer types[135], and, among other functions, promotes immunosuppression by interacting with LAG3 on immune cells such as dendritic cells and CD8+ T cells[136]. We find that the LGALS3/LAG3 ratio was significantly higher in activated DC high versus activated DC low (Fig 3.2.4.D), suggesting that this mechanism may contribute to an immune-exclusion environment.

GEPIA[137] was then used to evaluate the expression of LGALS3 within the TCGA cohort. GEPIA is a publicly available bioinformatics tool that lets you explore the gene expression in the TCGA RNA sequencing data. Gene expression analysis of the TCGA PTCs using GEPIA revealed that the TCGA cohort significantly expressed more LGALS3 than normal thyroid tissues (Figure 3.2.5.A). The importance of GAL3 in PTC diagnosis has been widely investigated, and it has been documented that more aggressive variants of PTC express higher levels of LGALS3[135].

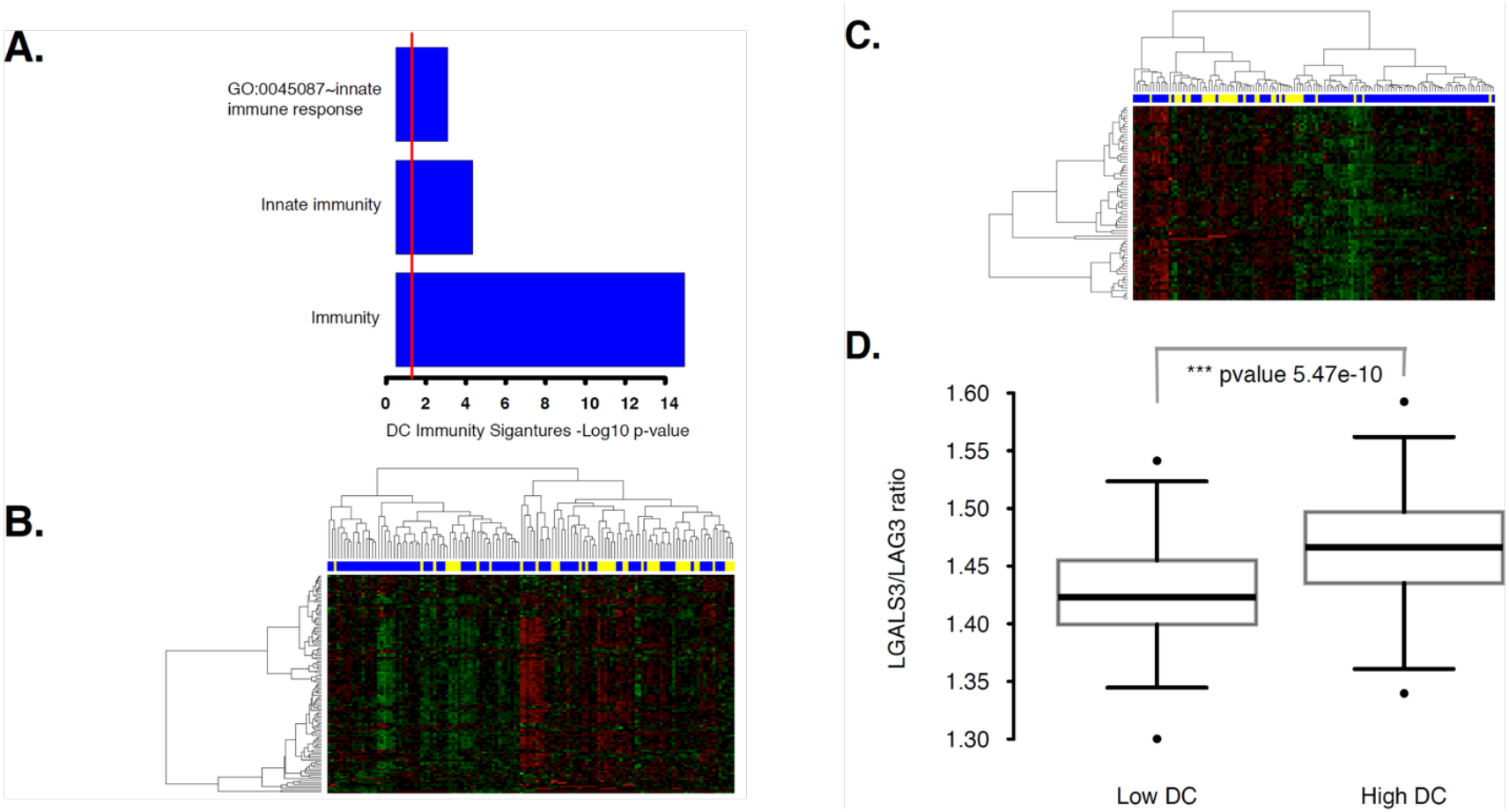

Figure 3.1.4. Immune gene expression in activated DC high PTCs. A) Negative log10 of the FDR value for pathway enrichment for terms in the top cluster from DAVID analysis of differentially expressed genes between low and high activated DC thyroid samples. Red line marks p-value of 0.05. B) Heatmap of the differentially expressed genes from DC enriched immunity signature. Green is high expression and red is low expression. Yellow marks high activated DC and blue marks low activated DC tumors. Most high activated DC samples are in the cluster with predominately low expression of the genes in the immune signature. C) Heatmap of differentially expressed genes from TFH enriched immunity signature. Green is high expression and red is low expression. Yellow marks high TFH and blue marks low TFH. Most high TFH samples are in the cluster with predominately high expression of the genes in the immunity signature. D) Ratio of LGALS3 to LAG3 in activated DC low and high samples ($p=5.47 \times 10^{-10}$).

In order to confirm the increased LGALS3 gene expression identified in TCGA using GEPIA, we collected a cohort of Vanderbilt infiltrative follicular variant PTCs (FVPTCs) and the more indolent non-invasive follicular thyroid neoplasms with papillary-like nuclear features (NIFTPs) to perform GAL3 immunohistochemistry. We evaluated GAL3 immunohistochemical expression in 11 NIFTPs and 12 infiltrative FVPTCs to see if GAL3 correlated with more malignant or indolent tumor types. We scored GAL3 IHC intensity on a scale of 0-3, where a score of zero indicated no staining, and a score of 3 indicated strong staining. The localization of the staining and score were used in conjunction to sort tumors into strong/diffuse GAL3 (diffuse 2-3+ staining), focal/subcapsular GAL3 (focal 1-3+ staining), and GAL3 negative (0 staining) (Figure 3.2.5.B,C). Fifty-four percent (7/12) of the invasive FVPTCs demonstrated strong, diffuse staining compared to none (0/11) of the NIFTPs. In contrast, none of the invasive FVPTCs were negative for GAL3, compared with 36% (4/11) of NIFTPs. Of note, the 7/11 (55%) of NIFTPs positive for GAL3 staining showed distribution that was distinct from that of invasive FVPTCs. Subcapsular staining with strong intensity (2-3+), was identified in 45% (5/11) of NIFTPS and 17% (2/12) of invasive FVPTCs. The remaining 18% (2/11) of NIFTPs showed focal GAL3 positivity (p=0.0019). These data demonstrate increased GAL3 in more invasive tumors and a distinct subcapsular or peripheral GAL3 staining in more indolent, and potentially pre-malignant, NIFTPs. This differential GAL3 expression confirms the GEPIA findings and is a potential mechanism for the T cell exclusive phenotype of papillary thyroid carcinomas.

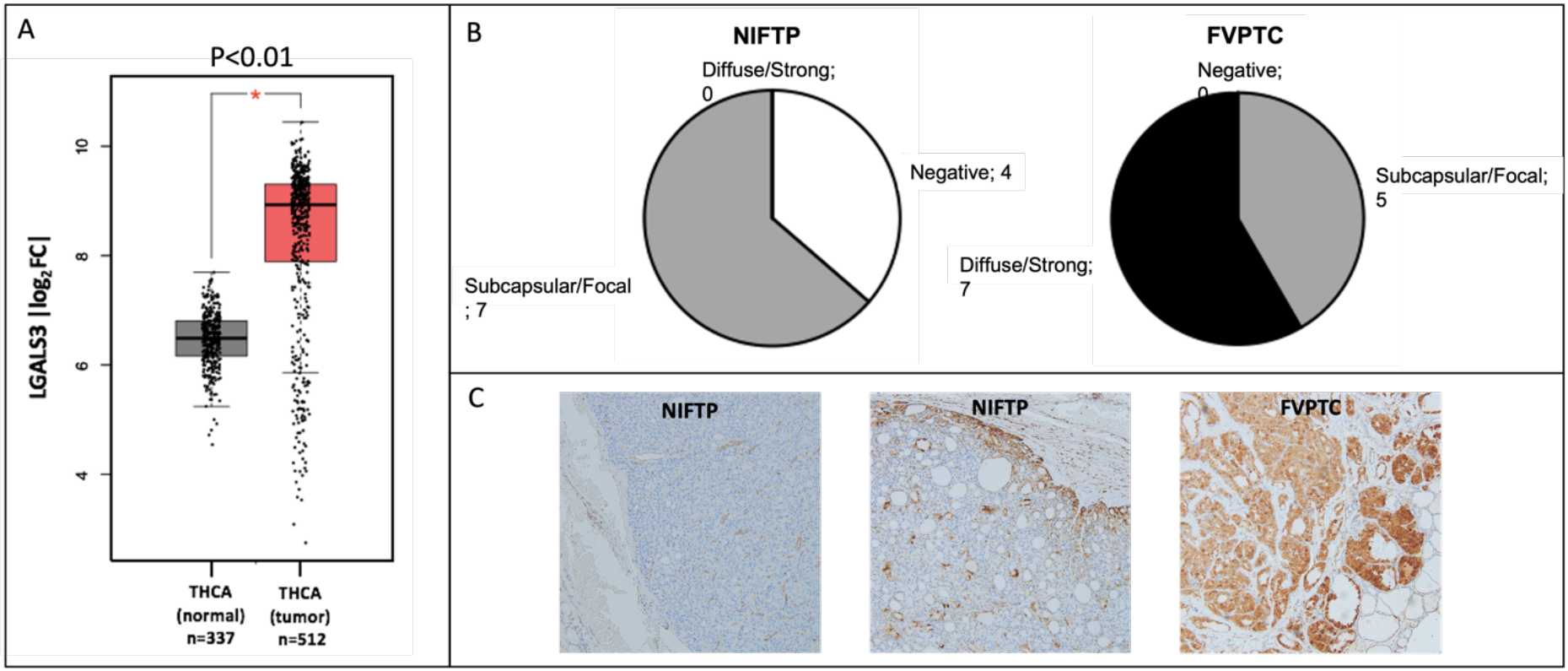

Figure 3.1.5. GAL3 expression in NIFTPs and infiltrative FVPTCs. A. GEPIA analysis of LGALS3 expression in TCGA THCA ($p<0.01$). Statistical analysis performed in GEPIA is a one-way ANOVA, using disease state as a variable for calculating differential expression. B. Tumor morphology was evaluated and tumors were stained for GAL3 expression ($p=0.0019$). C. Representative IHC images of GAL3 staining (left-negative; middle-subcapsular; right-strong/diffuse).

3.1.6. Discussion and Conclusion

The immunology of thyroid carcinoma has been previously studied using TCGA data. Similar to studies by Na et al.[126] and Kim et al.[127], our study confirms that immune infiltrates are associated with BRAF mutations and adverse outcomes. We also show that these findings are consistent across two deconvolution methodologies. However, the specific immune cells involved in aggressive thyroid tumor behavior are unclear, and this knowledge will be essential in designing targeted immunotherapy. Our study expands upon the findings of other groups by showing the specific immune cell subtypes associated with more aggressive tumor characteristics, as well as proposing a mechanism for immune exclusion by dendritic cell infiltration and galectin 3 expression.

The literature currently shows conflicting data regarding the role of specific immune infiltrates in thyroid cancer. Here, we present a robust evaluation of immune cell infiltrates and demonstrate that immune composition varies across different PTC histologic subtypes, mutational types, tumor T stage, and LN stage (potential surrogate markers of tumor behavior including extra-thyroidal extension and metastatic potential). The main immune cell types that are significantly associated with adverse PTC features across two distinct deconvolution tools are macrophages, dendritic cells, and neutrophils (Figure 3.2.6). Indeed, these innate immune cells significantly correlate with markers of aggressive disease such as BRAF mutation, tall cell morphology, increased tumor stage, and LN metastases. PTC-derived DCs may be responsible for regulatory T cell (Treg) differentiation from CD4 T cells, and subsequent tumor immune evasion[117]. Similar to DCs, tumor associated macrophages (TAMs) are associated with more aggressive tumor behavior, larger tumor size, lymph node metastases, and poor clinical outcome[,115,116,120-122]. Our studies confirm the presence of these innate immune cells in more advanced tumors and more aggressive subtypes using a large PTC cohort.

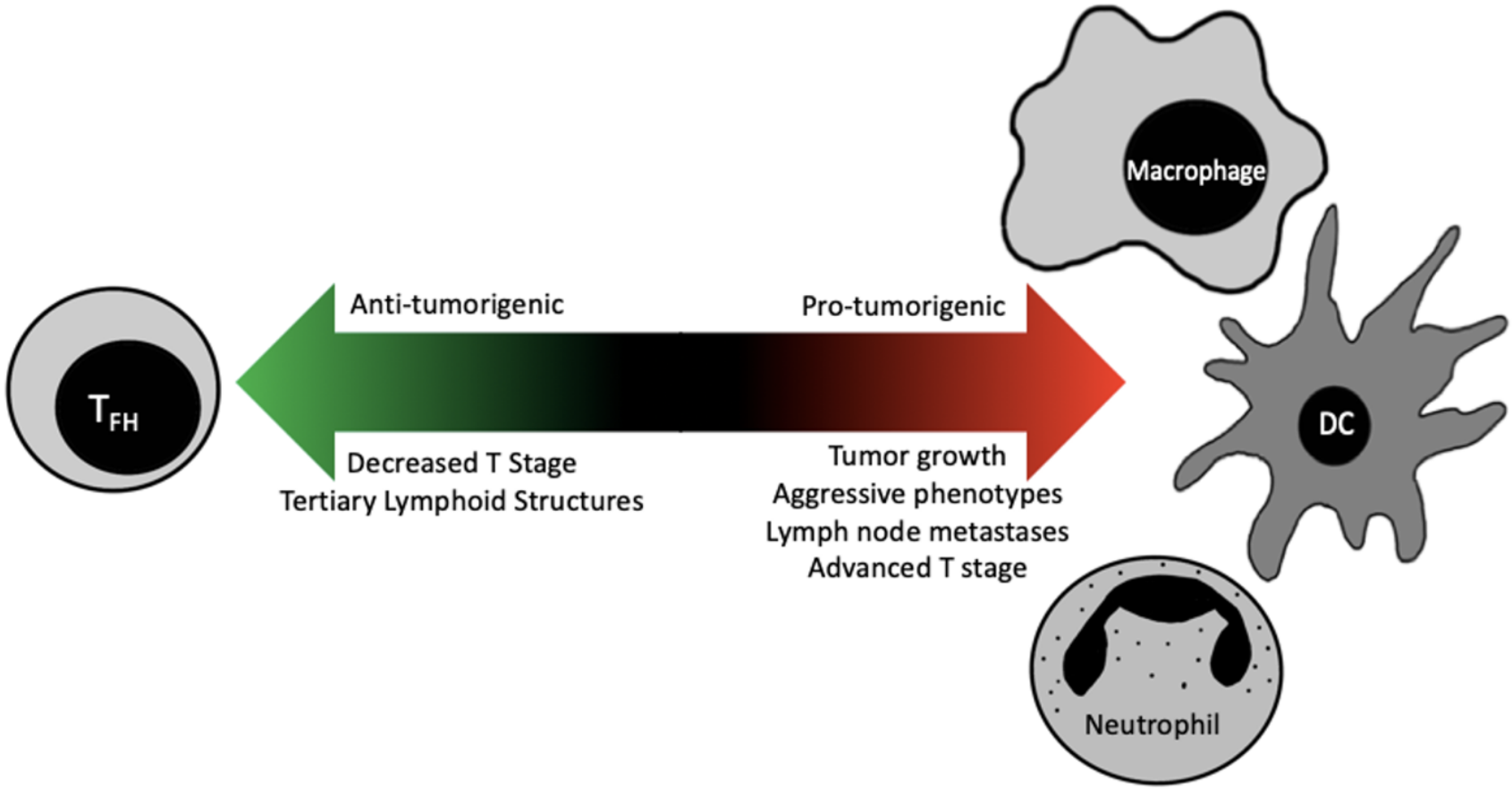

Figure 3.1.6. Representation of the potential role of immune cell types in thyroid cancer.

Our study also links certain innate immune cells, especially dendritic cells and neutrophils, with the development of lymph node metastases. Neutrophils have been shown to be important for metastasis in multiple cancer types, including melanoma[124], breast cancer[125], and gastric cancer[123]. Recent literature also suggests involvement of neutrophils in the growth of thyroid carcinomas[138]. While the mechanism of neutrophil-mediated enhancement of metastasis is unclear, some studies suggest that neutrophils inhibit CD8 T cells and may attract metastatic cells to new sites[125,139]. Data in breast and other cancers suggests that immunosuppressive DCs correlate with metastatic disease and shorter survival[140]. These DCs may enhance metastasis through their role in enhancing angiogenesis and tumor vascularization[141]. Our data support the role of neutrophils and immunosuppressive dendritic cells in enhancing metastatic behavior in thyroid cancer.

For many tumors, lymphocytes play an important role in anti-tumor immunity. A subset of tumors in the TCGA cohort demonstrate a potential anti-tumor infiltrate, the follicular helper T cells (TFH). TFH cells are thought to be essential in anti-tumoral immune recruitment and formation of tertiary lymphoid structures (TLS), which may be involved in T cell priming and B cell trafficking via CXCR5 expression[142-145]. The presence of TFH cells and TLS are thought to be good prognostic markers in many tumors, including breast cancer[146], where they are associated with a higher overall survival and increased response to neoadjuvant chemotherapy[147,148]. Our data suggests that this protective function may be present within a subset of PTC tumors.

The vast majority of PTCs in the TCGA cohort have gene signatures consistent with T cell exclusion. This T cell exclusion may be due to the presence of immunosuppressive DCs and macrophages. Evaluation of the TCGA PTC cohort demonstrates an overall decreased immune signature in DC-rich PTCs, suggesting an immunosuppressive or immune exclusive role in thyroid cancer. One potential mechanism of T cell exclusion is the interaction of LAG3 and GAL3. In assessing the immune signatures of DC low and high tumors, we find that the LGALS3/LAG3 ratio is significantly higher in activated DC high tumors, suggesting that this may be a potential mechanism for the immune-exclusion environment. Indeed, studies suggest that GAL3 may inhibit the formation of inflammatory DCs in the tumor microenvironment via LAG3[136]. In addition, GAL3 has been shown

to decrease T cell recruitment[149]. This mechanism of GAL3 mediated T cell exclusion may play an important role in thyroid cancer immune evasion. Evaluation of our PTC and NIFTP cohort confirms the increased GAL3 in infiltrative FVPTCs and the exclusion of T cells to the PTC periphery.

One limitation to this study is that the two analytic tools occasionally demonstrate some conflicting results, likely based on their different computational approaches, pre-defined immune gene signatures, numbers of immune subsets, and data output format. This can cause issues with the direct comparison of results. CIBERSORT provides an analysis of 22 immune cell subtypes. However, the method of defining these subtypes, such as M1 and M2 macrophages is controversial, and it is possible that false positives for each group were included in the output due to overlapping gene expression. This may also be the case with Treg cells, as both activated TFH[115,116] and PTC tumor cells[118,150] have been shown to express FoxP3 (an important Treg marker). This may explain why few significant Treg correlations were seen in this study using CIBERSORT, despite evidence that Tregs are important in many cancer types. Another issue is that CIBERSORT, while providing overall p values for each tumor, does not provide p values for each individual immune cell fraction. TIMER also provides no significance data for its immune cell calculations. These issues reveal a need for additional complex immune subset analyses, particularly for rare immune cell infiltrates, to confirm the results of computational analyses. It is also important to note that the staging data provided by TCGA is from AJCC edition 7, recently replaced by AJCC edition 8, wherein some previously high stage tumors would now be classified as lower stage. Although we are unable to re-stage the TCGA tumors, the previous staging method still provides useful qualitative information on the presence of microscopic extra-thyroidal extension and lymph node metastasis.

Here we present a computational evaluation of immune cell fractions in PTCs and show that the presence of certain cell types, particularly dendritic cells and neutrophils, strongly correlate with histology subtype, mutational status, T stage and lymph node metastases. We also demonstrate an immune exclusion phenotype of PTCs that may be dependent on GAL3 and LAG3 mediated mechanism of immune suppression and T cell exclusion. Further studies that include poorly-differentiated thyroid carcinomas will allow for a better

understanding of the role of immune cells in thyroid cancer progression and survival. In addition, an understanding of the immune composition of the tumor at the time of tumor biopsy may eventually provide supplemental diagnostic and prognostic information regarding the thyroid cancer subtype and potential for metastatic or recurrent disease.

3.1.7. Subsequent Related Work (Unpublished)

After defining the tumor-immune microenvironment and finding significant associations between tumor behavior and disease aggression, we yet again recognized the need for model system development to study the thyroid tumor-immune interaction. The first of these, the monocyte-spheroid co-culture system, was established to allow for time-resolved imaging studies of monocyte trafficking into spheroids, as well as the impact of treatment on macrophage differentiation and behavior within a three-dimensional system (Figure 3.2.7.A.). We found that monocytes derived from human PBMCs, when co-cultured with K1 PTC cells, survive for at least 7 days and do not require additional supplementation. Additional work is required to characterize media conditions that will allow for enhanced survival.

We then created an immune-humanized murine model that could be xenografted with our cell lines to produce a system that allows for measurement of monocyte trafficking in a complex in vivo model as well as determination of monocyte effects on tumors in the presence of therapeutics. Tumors were injected subcutaneously into the flank of NOD.Prkdc^{scid}Il2rg$^{-/-}$H2-$^{dlAb1\text{-}Ea}$B2m$^{-/-}$(NSG$^{\Delta MHC}$) mice. These mice do not express their own major histocompatibility complex (MHC) molecules, which greatly reduces the risk of graft vs. host disease and allows for extended reconstitution with human immune cells. One week after tumor injection, CD14+ enriched PBMCs were administered via tail vein injections. Excitingly, at 6 and 14 days post-injection we see preferential trafficking and activation of the monocytes within the tumors (Figure 3.2.7.B.). This model will be used for future studies on the impact that therapeutics and mutational status have on immune cell trafficking in vivo.

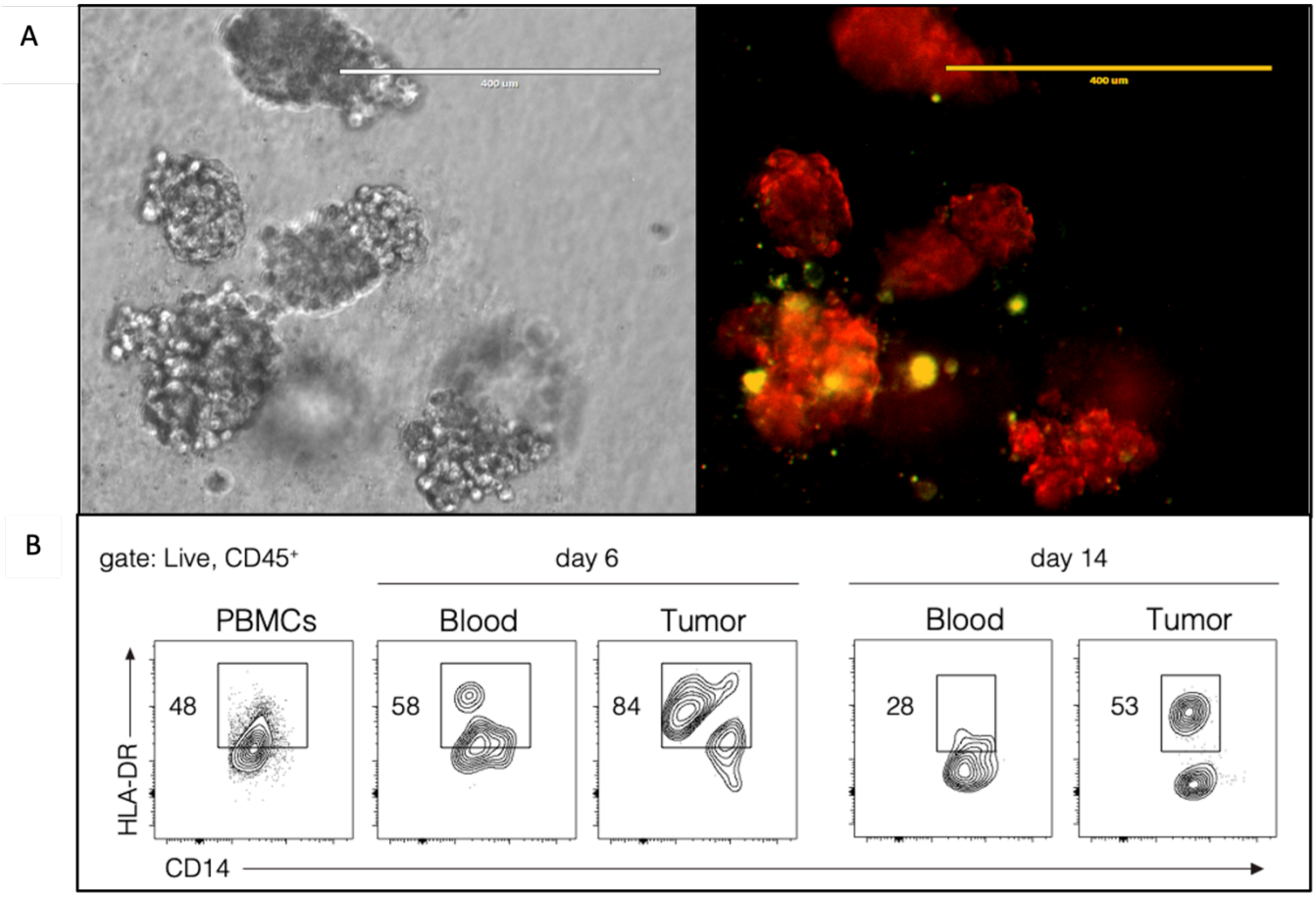

Figure 3.1.7. Tumor-immune modeling in spheroid co-cultures and humanized mice. A. K1 PTC cells expressing constitutive nuclear mKate (red) were mixed with CSFE-stained (green) CD14+ (monocyte) enriched primary blood mononuclear cells (PBMCs). After 7 days of culture in 5% Matrigel, spheroid co-cultures were imaged at 10X. Scale bar is 400um. B. Monocytes were enriched from PBMCs and injected via tail vein one week after flank tumor establishment. At the indicated timepoint, mice (n=5/timepoint) were euthanized, and tumors and blood were collected for flow cytometry. Based on gating from PBMCs, we established a live, CD45+, CD14+, HLA-DR high population, indicated in boxes and as percentages.

3.3. DEFINING THE PRESENCE AND ROLE OF WNT/β-CATENIN IN ATC

3.3.1. Summary and Contribution of Study

This project is split across this subsection and 4.2. to provide adequate context to each section. In this subsection, I detail the process of identifying Wnt/β-catenin signaling as a therapeutic target in anaplastic thyroid carcinoma. Previous work on Wnt signaling in ATC has indicated that ATCs have highly elevated Wnt activity, though it has been attributed to gain-of-function mutations in β-catenin or loss-of-function mutations in parts of the β-catenin destruction complex (such as AXIN1). Our study, with a large cohort of ATC patients and access to a variety of patient-derived organoid cultures, has shown that elevated Wnt signaling is not due to mutations, but rather due to increased ligand levels. Having defined the presence and importance of Wnt signaling in ATCs, we then sought to target the Wnt pathway to determine the therapeutic potential of this target. Pyrvinium was selected as a first approach due to FDA-approval as an orphan drug, which could potentially allow it to move into clinical trials much faster.

This work has been submitted for publication to *Nature Cancer*, and the text herein is adapted from:

Bergdorf, K., Xu, G., Loberg, M., Phifer, C., Sheng, Q., Ye, F., Rohde, S., Netterville, J., Baregamian, N., Shaddy, S., Huang, E., Murphy, B., Goettel, J., Lee, E., and Weiss, V. 2022. Wnt/β-catenin signaling is a therapeutic target in anaplastic thyroid carcinoma. *Submitted to Nature Cancer.*

3.3.2. Abstract

Anaplastic thyroid carcinoma (ATC) is a highly aggressive malignancy that has consistently shown Wnt/β-catenin (canonical) signaling activation in various study populations. Herein, using a large patient cohort and organoid models, we confirm that this near-universal Wnt signaling activation is ligand- rather than mutation-driven and promotes the dedifferentiation that defines disease transformation. Finally, we characterize Wnt inhibitors, both in vitro and in vivo, as a potentially effective novel therapy for this highly lethal disease.

3.3.3. Introduction

The incidence of thyroid cancer is rapidly increasing in the US and is projected to surpass colorectal cancer as the 4th leading cancer diagnosis by 2030[1]. Most patients respond to initial therapy, but approximately 20% will develop recurrence and 10% will develop metastatic disease[33]. Treatment options are extremely limited for patients with metastatic, recurrent, or dedifferentiated disease, such as anaplastic thyroid carcinoma (ATC). There is currently no targeted therapy for BRAF-wildtype ATCs, and combination dabrafenib-trametinib therapy (approved for ~25% of BRAFV600E mutant ATCs) has shown limited efficacy to date[28,29]. Lack of effective interventions has led to a dismal 5-year survival rate of only 5% and a median survival post-diagnosis of 4-6 months[2].

3.3.4. Materials and Methods

3.3.4.1. Patient cohort

361 thyroid resection specimens were collected from 251 patients at Vanderbilt University Medical Center (VUMC) and the University of Washington between 2004-2020. Thyroid pathology was reviewed (VW) and final tumor staging assignments were updated according to the AJCC 8th Edition Cancer Staging Manual[151].

3.3.4.2. DNA sequencing and mutational analysis

We completed whole-exome sequencing of our formalin-fixed paraffin-embedded (FFPE) cohort (>200x average coverage, 66x average depth, 10x minimum acceptable average depth per sample). DNA/RNA was extracted using the COVARIS DNA/RNA FFPE isolation kit. DNA libraries were built using the NEB DNA Ultra II kit. Sequencing was performed in the Vanderbilt Technologies for Advanced Genomics (VANTAGE) core facility on an Illumina NovaSeq 6000 platform using the IDT xGen® Exome Research Panel. Raw 150 bp paired-end reads were trimmed to remove adapter sequences using Cutadapt (v2.10) and the quality of the reads before and after trimming was checked by FastQC. Trimmed reads were aligned to hg38 genome using BWA (v0.7.17-

r1188). GATK v.4.1.8.1 was used to remove duplicate reads, perform base quality score recalibration and variants discovery. Variant calling was performed on individual samples using HaplotypeCaller in gVCF mode, then all samples were jointly genotyped, and variant filtering was performed with VQSR. Variant annotation was conducted with ANNOVAR (v2018-04-16). Variants with minor allele frequency ≥0.1% in any of ExAC (Exome Aggregation Consortium), 1000g, and gnomad databases were filtered out. AXIN1 and CTNNB1 mutations were evaluated according to the standards and guidelines for the reporting of sequence variants in cancer by the Association for Molecular Pathology, American Society of Clinical Oncology, and the College of American Pathologists[152].

3.3.4.3. RNA sequencing and GSEA

Illumina TruSeq mRNA sequencing libraries were prepared and sequenced at VANTAGE on a NovaSeq 6000 (Illumina) platform. Raw 150bp paired-end reads were trimmed to remove adapter sequences using Cutadapt (v2.10) and aligned to the GENCODE GRCh38.p13 genome using STAR (v2.7.8a)[153]. GENCODE v38 gene annotations were provided to STAR to improve the accuracy of mapping. Quality control on both raw reads and adaptor-trimmed reads was performed using FastQC (www.bioinformatics.babraham.ac.uk/projects/fastqc). featureCounts (v2.0.2) was used to count the number of mapped reads to each gene[154]. Gene set enrichment analysis was performed using GSEA (v4.1.0) on msigdb v7.1 database[155].

3.3.4.4. Cell Culture

K1 cells were obtained from Sigma Aldrich. TPC1 cells were obtained from Dr. Adel El- Naggar (University of Texas MD Anderson Cancer Center, Houston, Texas). Cells were authenticated using STRS analysis and maintained and used experimentally at <20 passages from thaw. Cells were grown in RPMI (VWR) containing 10% FBS (ThermoFisher Scientific), 1% penicillin-streptomycin (Sigma), 1X MEM Non-Essential Amino Acids (VWR), and 1 mM sodium pyruvate (Vanderbilt Molecular Biology Resource), henceforth referred to as ‘complete RPMI’.

3.3.4.5. Spheroid Area and Counting

K1 cells were plated in 5% Matrigel in a 24-well low-attachment cell culture plate and treated with 50% LWRN conditioned DMEM or 50% DMEM (control collection media) for 6 days prior to imaging with a Leica DMi1 MC170 inverted microscope with a 4× objective and processed on Leica Application Suite, version 4.10.0. ImageJ v1.53.o was used to count and measure the area of each organoid across 8 replicates per condition. A t-test was used to compare counts and areas across conditions for 3 replicates.

3.3.4.6. Flow Cytometry

VWL-T40 were cultured and maintained as described in Vilgelm et al.13 and Phifer et al.15 in DMEM, Ham's F12, and MCDB media + 10% FBS with 2% B27 Supplement without Vitamin A. 12-well plates were seeded with 50,000 cells/well, and CHIR99021 was added to a final concentration of 1uM in treatment wells. CHIR99021 was refreshed 48 hours after plating. After 4 days of incubation at 37C, cells were stained with eBioscience Fixable Viability Dye eFluor™ 506 (Thermofisher) prior to trypsinization, fixation with 4% formaldehyde for 20 minutes at room temperature, and permeabilization with 0.5% TBS + 0.5% Triton X for 30 minutes on ice. Rabbit anti-thyroglobulin (Abcam ab156008) was used at a 1:200 dilution in PBS and allowed to incubate for 30 minutes at RT. Donkey anti-rabbit IgG conjugated to PE and and mouse anti-human CD29 conjugated to APC were each used at a dilution of 1:1000 in PBS and incubated for 30 minutes at RT in the dark prior to data acquisition with a 3-laser Fortessa (BD). Data were analyzed using FlowJo 10.8.1 (BD).

4.2.2.1. Cell Culture

THJ-11T, THJ-16T, THJ-21T, and THJ-29T were obtained from Dr. John Copland (Mayo Clinic, Jacksonville, FL, USA). Cells were authenticated using STRS analysis and maintained and used experimentally at <20 passages from thaw. Cells were grown in RPMI (VWR) containing 10% FBS (ThermoFisher Scientific), 1% penicillin-streptomycin (Sigma), 1X MEM Non-Essential Amino Acids (VWR), and 1 mM sodium pyruvate (Vanderbilt Molecular Biology Resource), henceforth referred to as 'complete RPMI'.

4.2.2.2. Generating dose-response curves

THJ-11T, THJ-16T, THJ-21T, and THJ-29T cells Utilizing the high-throughput equipment in the Vanderbilt High-Throughput Screening (VHTS) core facility, 300 cells in 30 µL of cell suspension was plated per well in black 384-well cell-repellant culture plates (Greiner Bio-One). Spheroids were allowed to form for 24 h prior to treatment with DMSO, dabrafenib+trametinib, and/or pyrvinium (Selleck Chemicals) in RPMI. Following 72 h of treatment, wells were imaged using an ImageXpress Micro XL automated high-content microscope (Molecular Devices). To assess viability, CellTiter-Glo 3D (Promega) was added to wells and mixed with the Bravo liquid handler (Velocity 11/Agilent). Per the CellTiter-Glo protocol, plates were placed on a shaker for 25 min before luminescence was quantified using a Synergy NEO (BioTek multi-mode plate reader).

4.2.2.3. Organoid culture

Patient-derived organoids were collected and maintained as described in Vilgelm et al. and Phifer et al. For drug treatment, organoids were centrifuged for 5 minutes at 340 x g to form a loose pellet. This pellet was washed with cold PBS prior to dissociation for 30 minutes at 37°C in 1X TrypLE (Gibco). The resulting cell suspension was washed and resuspended in culture media containing 5% Matrigel and DMSO, 30nM dabrafenib+5nM trametinib, and/or 300nM pyrvinium prior to plating in a 24-well low-attachment culture plate. Organoids were incubated at 37°C, 5% CO_2 for 8 days prior to imaging with a Leica DMi1 MC170 inverted microscope with a 4× objective and processed on Leica Application Suite, version 4.10.0. All work with patient-derived cells was approved by the Vanderbilt Institutional Review Board.

4.2.2.4. Murine studies

All procedures were approved by the Institutional Animal Care and Use Committee prior to completion. NOD.Prkdc^{scid}Il2rg$^{-/-}$ (NSG-Jackson Laboratories) were injected with 1 million PDX THJ-16T cells subcutaneously in the flank using a 22G needle affixed to a 1mL syringe. When tumors became palpable (approximately 2 weeks post-injection), intraperitoneal injection of vehicle or pyrvinium (5% DMSO in corn oil) was started. We performed a dose-escalation of 0.5mg/kg, 1mg/kg, 1 mg/kg, 2mg/kg with injections every other day, maintaining at 2mg/kg for the remainder of the experiment. All injections were performed with a 26G SubQ

needle on 1mL syringes. Tumors were measured every other day using digital calipers, and mice were weighed weekly to ensure no significant weight loss was occurring. Endpoints were reached when tumors reached 2cm in any dimension or ulcerated, and mice were humanely euthanized. Data were analyzed using Microsoft Excel and GraphPad Prism 8, and significance was determined by a mixed-effects model.

3.3.5. Results

Interestingly, it has been shown in multiple study populations that ATCs consistently exhibit elevated Wnt/β-catenin signaling (hereafter referred to as Wnt signaling)[156-158]. These studies have attributed the increase in signaling to stabilizing β-catenin mutations or loss-of-function mutations in the β-catenin destruction complex (increases β-catenin levels). As part of our IRB-approved study, we have completed RNA- and whole exome sequencing on 361 patient tumors, 17 of which are primary anaplastic thyroid carcinomas. Notably, we do not detect any previously reported Wnt pathway mutations in ATCs, though we do observe highly elevated Wnt signaling levels across ATC patient tumors when compared to less aggressive subtypes (Figure 3.3.1.A,B,C). The lack of mutations, in combination with elevated signaling, led us to identify significantly higher levels of Wnt ligands Wnt1, Wnt2, Wnt5B, Wnt7A, Wnt7B, Wnt10A, Wnt10B, and Wnt16 in ATC compared to less aggressive subtypes (Figure 3.3.1.D).

To determine the effects of canonical and non-canonical Wnt signaling on spheroid growth and behavior, we treated K1 (PTC) cells with L-WRN (Wnt3A, R-spondin3, Noggin) media for 6 days to activate Wnt signaling prior to assessing spheroid morphology. LWRN treatment led to an increased number of spheroids with a morphology resembling ATC spheroids (THJ-21T). These smaller, discohesive, spindly spheroids suggest epithelial-to-mesenchymal transition (EMT, Figure 3.3.1.E).

Having established that Wnt signaling is elevated in our patient population and that this Wnt signaling can promote dedifferentiation, we aimed to identify a targeted inhibitor. Many Wnt inhibitors are commercially available and have been explored in clinical settings. Pyrvinium is an anti-helminth (pinworm) drug that was

identified as a potent Wnt inhibitor in 2010[194] and has been given orphan drug designation by the FDA for Familial Adenomatous Polyposis. Using our high-throughput spheroid methodology, we generated dose-response curves to pyrvinium (PYR-Figure 4.2.2.A). Interestingly, pyrvinium showed enhanced potency in the BRAF-wildtype cell lines (THJ-11T, THJ-16T, THJ-29T).

To evaluate Wnt inhibition as a therapeutic approach, we used the most aggressive of our three BRAF-wildtype ATC cell lines, THJ-16T, in a xenograft model of anaplastic thyroid cancer. Mice treated with pyrvinium showed significantly decreased tumor growth, β-catenin, and vasculature compared to mice receiving only vehicle (Figure 4.2.2.B, C). Next, we utilized our fine-needle aspiration-derived patient tumor organoid cultures and a mouse xenograft model. As seen in the four ATC cell lines, pyrvinium significantly inhibited the growth of the BRAF-wildtype ATC organoid line VWL-T5 (Figure 4.2.2.D). We also compared pyrvinium to current BRAF-mutant standard-of-care, dabrafenib + trametinib (DAB+TRA), in our VWL-T60 BRAF-mutant organoid culture (Figure 4.2.2.E). We found that DAB+TRA combination therapy did not significantly decrease organoid size, consistent with clinical data demonstrating variable response to this therapy. In contrast, pyrvinium in combination with DAB+TRA and alone significantly inhibited organoid growth. These data show the potential utility of Wnt inhibitor therapy as a novel treatment for aggressive thyroid cancer.

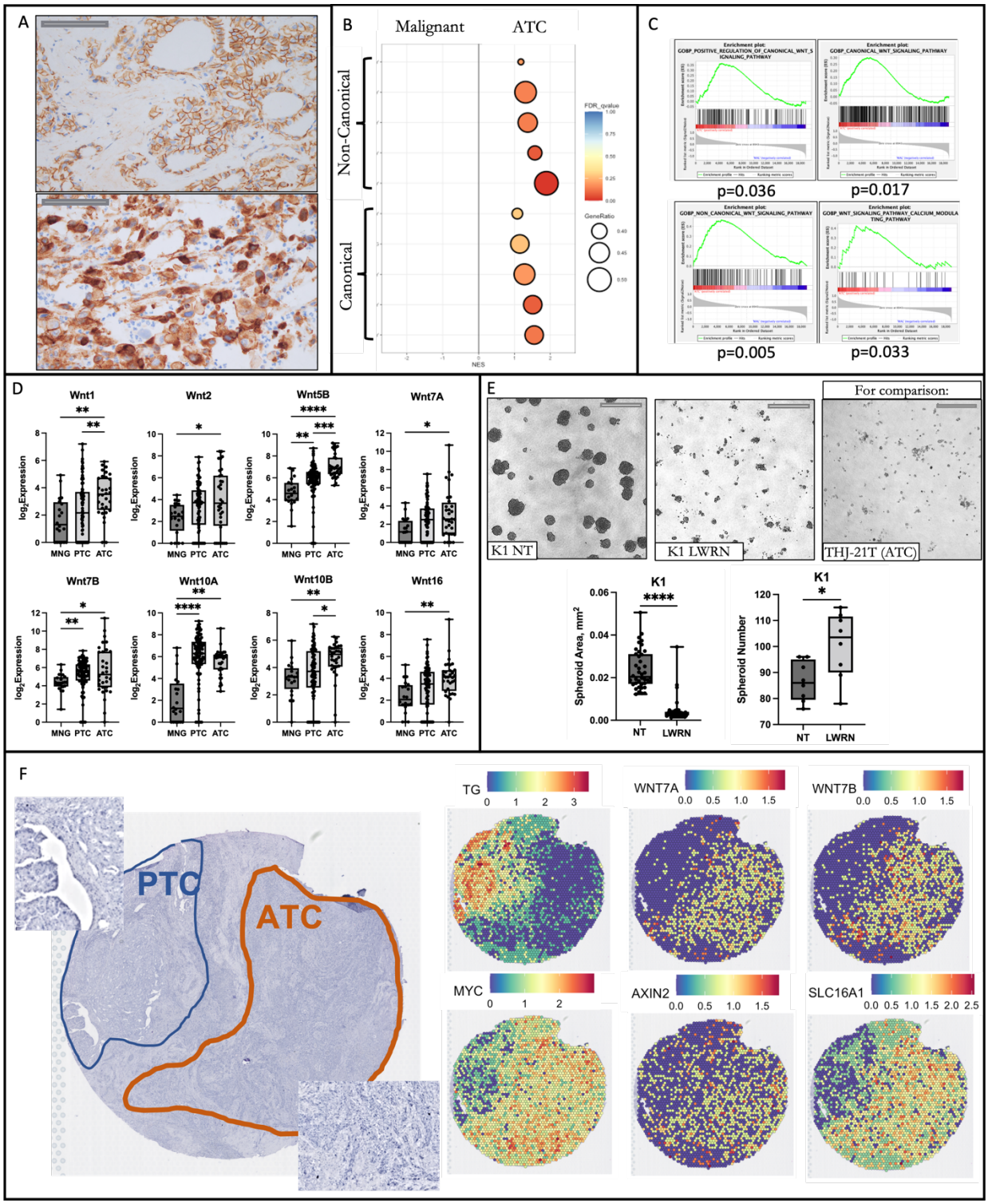

Figure 3.3.1. Increased Wnt ligand expression in ATC drives enhanced signaling and de-differentiation. A. IHC of patient tumors shows increased nuclear β-catenin in ATC. B. Bubble plot of 10 Wnt-related gene sets (5 canonical, 5 non-canonical). All are enriched in ATCs compared to all other malignant samples. C. Significantly enriched gene sets identified by GSEA of ATC RNAseq data compared to all other malignant samples. D. Expression of Wnt ligands compared between MNG, PTC, and ATC indicate higher Wnt ligand expression in ATCs. E. Treatment of K1 (PTC) spheroids with LWRN (Wnt3A, R-spondin3, Noggin) media promotes an EMT- and ATC-like phenotype. THJ-21T (ATC) spheroids for comparison. F. Visium data (spatially resolved scRNA sequencing data) of a mixed sample indicates negative association between Wnt and thyroglobulin.

3.3.6. Discussion

In defining the molecular drivers of anaplastic thyroid carcinoma, we aim to identify druggable targets for patients that currently have few treatment options. Through our studies, we have shown that elevated levels of both canonical and non-canonical Wnt ligands within the tumor microenvironment drive elevated Wnt signaling in ATCs compared to what is seen in all other malignant thyroid neoplasia. Additionally, we use a combined activator of both canonical and non-canonical Wnt signaling, LWRN media, in combination with K1 (PTC) spheroids. After 6 days of treatment, spheroids treated with LWRN media were smaller, discohesive, and spindly, suggesting an epithelial-to-mesenchymal transition (EMT). We treat a primary PTC organoid culture (VWLT40-containing tumor and stromal cells) with CHIR99021 (inhibits GSK3, increases Wnt signaling). While thyroid cancer cells are known to lose thyroglobulin expression in vitro, activation of Wnt signaling led to a further, albeit insignificant, decrease in thyroglobulin expression (Figure 3.3.2). This trend suggests that Wnt signaling may also play an important role in thyroid cancer de-differentiation. In addition to defining the importance of Wnt signaling in ATC, we also demonstrate the efficacy of pyrvinium, a Wnt inhibitor, in spheroids, murine models, and patient-derived organoid cultures. These studies provide preclinical evidence for the effectiveness of Wnt inhibitors in the treatment of ATC, a devastating cancer with limited treatment options.

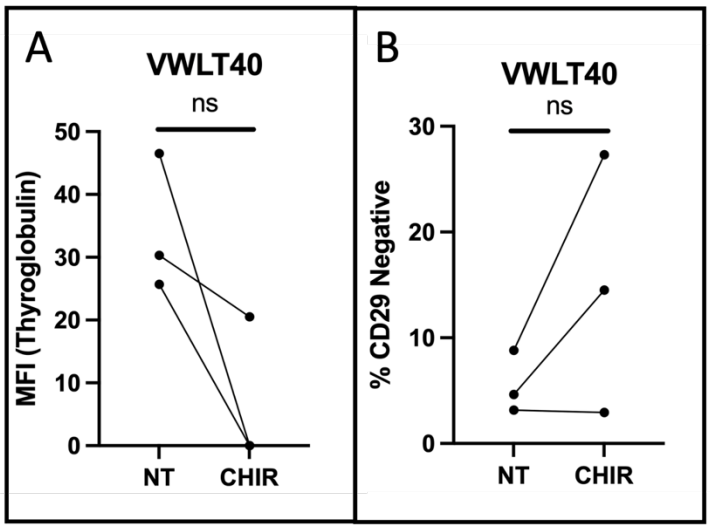

Figure 3.3.2. VWLT40, a BRAF-wildtype PTC organoid line, was treated with CHIR99021 (GSK3 inhibitor, stabilized β-catenin) for 4 days prior to analysis of thyroglobulin and CD29 levels via flow cytometry. A. The loss of thyroglobulin, while not significant, indicates possible transformation to a more dedifferentiated state as is seen in ATC. B. CD29, a marker of mesenchymal cells, identifies fibroblasts in the mixed population present in our organoid cultures. The increase in CD29- cells in the presence of CHIR is likely indicative of tumor cell expansion, though the data are not currently significant.

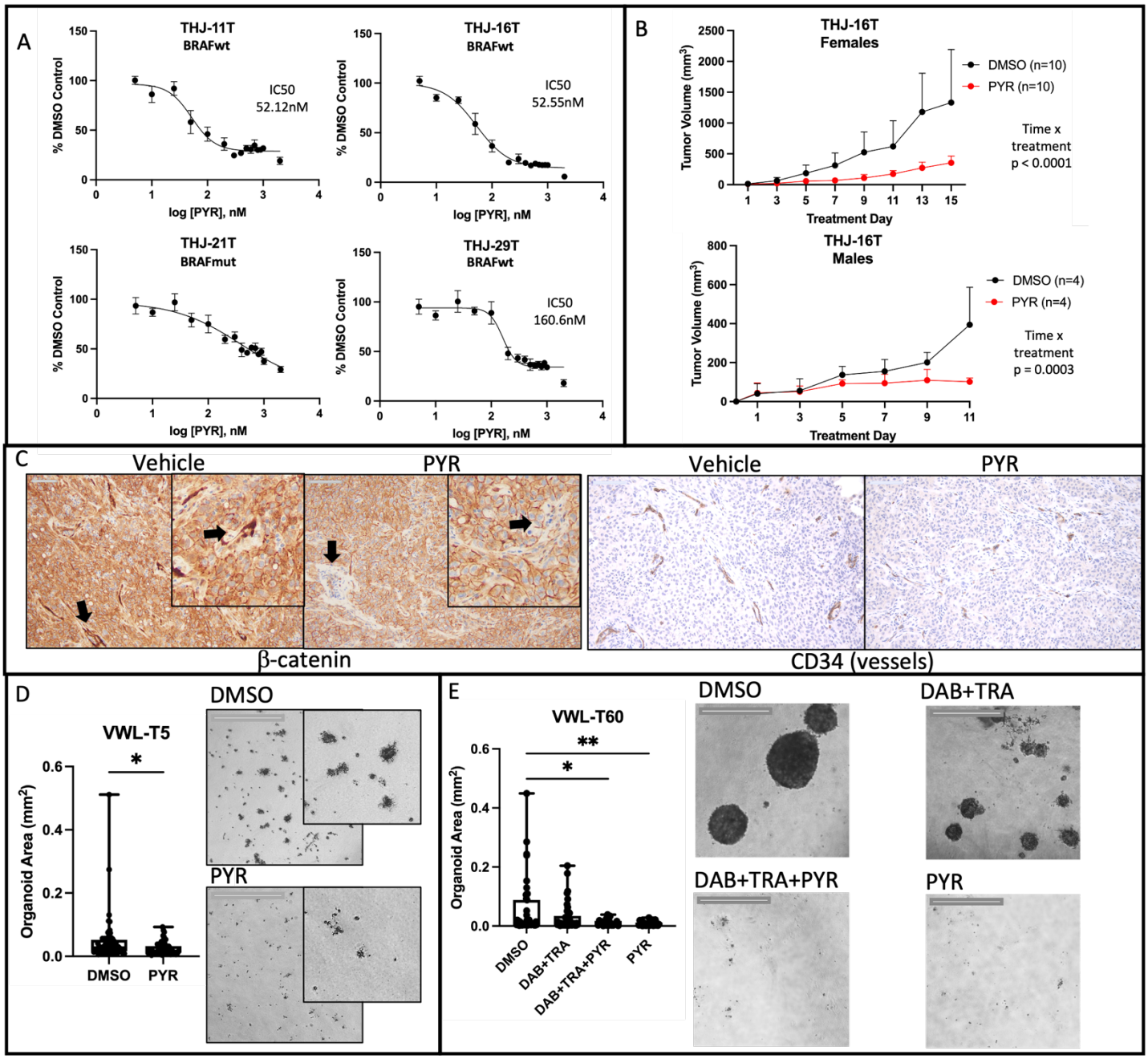

Figure 4.2.1. Pyrvinium significantly decreases ATC growth *in vitro* and in *vivo*. A. Normalized dose response curves (±SEM) were generated for spheroids treated with pyrvinium (PYR) for 72 hours (n=3). B. NSG mice with subcutaneous THJ-16T flank tumors were administered PYR once tumors were palpable. Tumor volume (±SD) was measured every other day. Both male and female mice treated with PYR had significantly smaller tumors than control mice. C. Immunohistochemical staining for β-catenin and CD34 (marker for vessels) in vehicle vs. pyrvinium treated mice indicates decreased overall β-catenin and vasculature in PYR treated mice. Arrows indicate stroma. D. Patient-derived organoid lines VWL-T5 (*BRAF*-wildtype) and E. VWL-T60 (*BRAF*-mutant) were treated with PYR for 8 days prior to organoid measurement. When used alone or in combination with standard-of-care (DAB+TRA, *BRAF*-mutant), pyrvinium significantly decreased organoid size. (* represents a p-value < 0.05, ** p<0.01

CHAPTER IV.

CHARACTERIZING NOVEL THERAPEUTICS FOR ATC

4.1. UTILIZING SPHEROIDS IN HIGH-THROUGHPUT DRUG SCREENING

4.1.1. Summary and Contribution of Work

After developing our spheroid culture model of ATC and adapting it to high-throughput screening methods, our first priority was performing a large-scale screen of over 1500 drugs to identify potential therapeutic candidates. Many of the drugs tested are already FDA-approved, meaning they can rapidly move into clinical trials for ATC patients. Additionally, by adding spheroids to the screening process, we sought to enhance the translatability of our data. As a result, we identified 33 promising therapeutic candidates and selected three high priority drugs: bortezomib, cabazitaxel, and YM155.

This subsection is adapted from work under review at *Cancers* for a feature in a thyroid carcinoma edition:

Bergdorf, K., Bauer, J., Westover, D., Phifer, C., Murphy, B., Tyson, D., Lee, E., and Weiss, V. 2022. Utilizing three-dimensional culture methods to improve high-throughput drug screening in anaplastic thyroid carcinoma. *Under review at Cancers.*

4.1.2. Abstract

Anaplastic thyroid carcinoma (ATC) is the most aggressive endocrine neoplasm, with a median survival of just four to six months post-diagnosis. Even with surgical and chemotherapeutic interventions, the five-year survival rate is less than 5%. While combination dabrafenib/trametinib therapy was recently approved for treatment of the ~25% of ATCs harboring BRAFV600E mutations, there are no approved, effective treatments for BRAF-wildtype disease. Herein, we perform a screen of 1567 drugs and evaluate therapeutic candidates

using monolayer cell lines and four corresponding spheroid models of anaplastic thyroid carcinoma. We utilize three-dimensional culture methods, as they have been shown to more accurately recapitulate tumor responses in vivo. These three-dimensional cultures include 4 distinct ATC spheroid lines representing unique morphology and mutational drivers to provide drug prioritization that will be more readily translatable to the clinic. Using this screen, we identify three exceptionally potent compounds (bortezomb, cabazitaxel, and YM155) that have established safety profiles and could potentially be moved into clinical trial for the treatment of anaplastic thyroid carcinoma, a disease with few treatment options.

4.1.3. Introduction

Anaplastic thyroid carcinomas (ATCs) are exceptionally aggressive tumors, with a median survival time of 4-6 months post-diagnosis, a 35% six-month survival rate, and a dismal five-year survival rate of less than 5%[160,161,]. These de-differentiated tumors grow rapidly and have a disease-specific mortality nearing 100%[162]. As the genetic and molecular drivers of transformation to ATC are not well-understood, early detection and treatment options are limited. It is this disparity, combined with their aggressive nature, that leads ATCs to account for over half of all thyroid cancer-related deaths despite comprising less than 2% of all thyroid neoplasms[2].

Approximately 25% of ATCs harbor a BRAFV600E mutation, which leads to constitutive activation of MAPK signaling. Fortunately, mutant BRAF can be targeted using dabrafenib, and paradoxical MEK/ERK activation can be avoided with the addition of trametinib[28,29]. This combination therapy was FDA-approved for the treatment of BRAFV600E mutant ATC in 2018. Median overall survival in patients treated with dabrafenib-trametinib therapy was extended to 14.5 months, though only 8% of patients exhibited a complete response to the therapy[29]. There are currently no effective, targeted therapies available for BRAF-wildtype ATC.

We have recently developed methods for culturing thyroid cancer spheroids and adapting these cultures to formats amenable to high-throughput drug screening[163]. Spheroids allow for cell-cell interactions and

nutrient gradients not possible in traditional monolayer culture, making them an ideal model for drug discovery and development[163,164]. Additionally, drug responses in three-dimensional cultures have previously been shown to deviate from those observed in corresponding monolayer cultures and to more accurately recapitulate patient tumor responses[39,165].

In this study, we sought to combine our ATC spheroid cultures with high-throughput drug screening to identify potential therapeutics for a disease with few treatment options. Through this methodology, we were able to identify three lead candidates for follow-up studies in both BRAF-mutant and -wildtype ATC. Notably, this study provides the basis for many routes of investigation into the molecular drivers and therapeutic targets of ATC to inform future clinical trials.

4.1.4. Materials and Methods

4.1.4.1. Cell Culture

ATC cell lines (THJ-11T, THJ-16T, THJ-21T, and THJ-29T) were obtained from Dr. John Copland (Mayo Clinic, Jacksonville, FL, USA). Cell lines are maintained at 37°C, 5% CO2 in RPMI (VWR, Radnor, PA, USA) supplemented with 10% fetal bovine serum (ThermoFisher Scientific, Waltham, MA, USA), 1% penicillin-streptomycin (Sigma, St. Louis, MO, USA), 1X MEM non-essential amino acids (VWR), and 1mM sodium pyruvate (hereafter referred to as “complete RPMI”). All cell lines are used experimentally at less than 20 passages and authenticated via STR analysis.

4.1.4.2. Drug libraries

The NCI Approved Oncology Drugs Set VII (National Cancer Institute, Division of Cancer Treatment and Diagnosis, Developmental Therapeutics Pro-gram) and the Selleck Chemicals FDA-approved and Anti-cancer Compound libraries (Selleck Chemicals, Houston, TX, USA) are maintained and distributed by the Vanderbilt High-Throughput Screening (VHTS) facility within the Vanderbilt Institute of Chemical Biology. In total, 1567 compounds were screened.

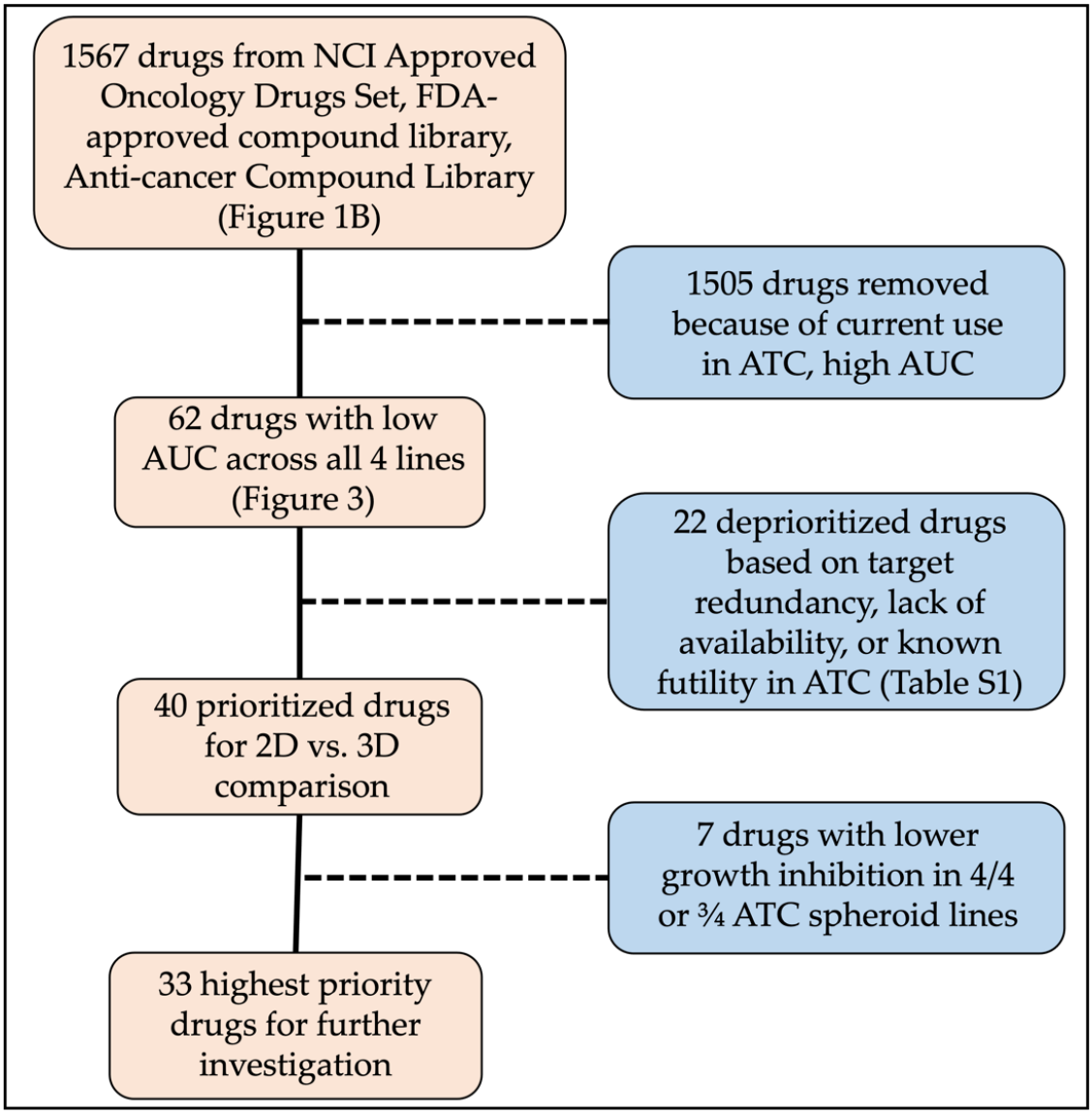

Figure 4.1.1. Schematic of drug numbers throughout studies.

4.1.4.3. Primary high-content imaging screen in ATC cell lines

High-throughput screens were performed in collaboration with the VHTS facility. Cells were seeded in 384-well cell culture plates (Greiner Bio-One #781091, Greiner Bio-One, Kremsmünster, Austria) at a density of 600 cells/well (THJ-11T; THJ-16T; THJ-29T) or 900 cells/well (THJ-21T) using a ThermoScientific Multi-Drop Combi dispenser and incubated at 37°C with 5% CO_2. After 24 hours, drugs and small molecules were transferred from library stock plates at 10mM DMSO solutions using an ECHO acoustic liquid transfer system (LabCyte/Beckman) to a 384-well drug plate. Drug plates were diluted with complete RPMI and robotically added to the cell plates at five final concentrations (5.14µM, 1.09µM, 156nM, 30.8nM, 6.2nM) in 0.2% DMSO (v/v). Cells were incubated with drugs for an additional 72 hours, after which they were stained with Hoechst 33342 (Invitrogen, Waltham, MA, USA) and propidium iodide (MilliporeSigma, Burlington, MA, USA) to final concentrations of 2µg/mL and 0.2µg/mL, respectively, and imaged on an ImageXpress Micro XLS using DAPI and Texas red filters (Molecular Devices, LLC, San Jose, CA, USA).

Viable cells were identified as those that were Hoechst positive and propidium iodide negative and compared across cell lines for each drug using the area under the curve for the 5 concentrations. In total, 62 drugs were identified via AUC and further confirmed by concentration-response plots generated using ten concentrations in technical triplicate ranging from 20µM to 20nM. Twenty-two drugs did not progress to further studies due to: (1) target redundancy; (2) lack of current clinical availability; or (3) established clinical futility in ATC (Figure 4.1.1.).

4.1.4.4. Lentiviral transduction

A lentivirus containing constitutive nuclear mKate under the human PGK promoter with blasticidin selection (TRC2-pLKO-PGK-nlsmKate2/Bsd) was generously provided by Dr. Huan Qiao (Vanderbilt University, Nashville, TN, USA). All cell lines were transduced at a multiplicity of infection of 10:1 for 24 hours prior to media replacement. Blasticidin selection concentration was determined prior to transduction and defined as the concentration needed to kill non-transduced cells in 5 days. Final concentrations used were between 5–

10µg/mL. Selection media (complete RPMI + blasticidin) was changed every 48 hours for the first two weeks post-transduction, then passaged regularly and maintained in selection media as needed.

4.1.4.5. Comparison of time-resolved drug response in 2D vs. 3D growth conditions

Transduced cells were seeded for monolayer culture in 384-well cell culture plates (Greiner Bio-One #781091) at a density of 300 cells/well in complete RPMI. All cell lines were seeded for spheroid culture in 384-well cell-repellent culture plates (Greiner Bio-One #781976) at a density of 600 cells/well (THJ-11T; THJ-16T; THJ-29T) or 900 cells/well (THJ-21T) in complete RPMI supplemented with 2% Matrigel (Corning, Corning, NY, USA) using a peristaltic EL406 dispenser (BioTek, Santa Clara, CA, USA) within a bi-osafety cabinet. Plates were immediately centrifuged for 5 min at 200g to allow cells and matrix to collect on the flat bottom plates. Following a 24-hour incubation at 37□C, 5% CO2, cell plates were placed into an automated incubator (Cytomat, Thermo) and each plate was shuttled to a Molecular Devices' ImageXpress MicroXL imaging system via a robotic plate handler (F3 arm, Thermo) and using the Momentum scheduler. Following initial cell density baseline imaging, drug plates diluted in media (as above) plus 5nM SYTOX Green (to detect dead cells- Invtirogen) were added to cell plates using a liquid handler and returned to the Cytomat. Cell plates were scheduled in a continuous loop to be imaged consecutively for 5 days.

4.1.4.6. Analysis of 2D vs. 3D drug response data.

The number of viable cells at each time point was determined by counting segmented nuclei from the red fluorescence channel that did not have fluorescent signal overlap in the green (dead cell) channel using custom Python scripts as previously described[166]. We calculated the highest dead cell fraction observed at any point over 72 hours at a given drug concentration, and that value was subtracted from 1 to generate a fraction of viable cells. These data were uploaded into a local instance of Thunor-web software that was specifically designed to automatically fit the data with 4-parameter log-logistic models[167]. The activity area (observed) is effectively the integrated area above the observed response values and calculated as described (https://docs.thunor.net/dose-response-parameters)[167]. Observed activity area (AAobs) is used in the analyses

of these data rather than AUC, as AAobs is positively associated with drug efficacy, where AUC is an inverse association. AAobs is also independent of any fitting function, relying only on the data collected. This same approach was applied to the spheroid cultures after first obtaining a maximum projection image from the complete z-stack obtained for each sample and time point.

To define differential drug response between monolayer and spheroids, AAobs values were plotted on axes of 2D AAobs (x) vs. 3D AAobs (y) (not shown). If a given compound produced identical results in monolayer and spheroid cultures, we expect that point to fall at x = y. A reference line was drawn representing this relationship and residuals from this reference were plotted for each cell line (Figure 4.1.4.D.-deltaAA). A positive value indicates higher activity in spheroid culture, while a negative value indicates in-creased activity in monolayer cultures. At this point, drugs were eliminated if they exhibited decreased inhibition in at least three of the four ATC spheroid cultures.

4.1.5. Results

4.1.5.1. Primary and Confirmation Screens Identify 40 High-Priority Compounds

4.1.5.1.1. Primary compound screen of 1567 drugs identifies 62 hits.

For our studies, we utilize four anaplastic thyroid carcinoma cell lines-THJ-11T; THJ-16T; THJ-21T; and THJ-29T. These cell lines were chosen due to distinct mutational and morphological profiles, summarized in Table 1, that are representative of disease diversity observed in vivo[168,169]. In using these distinct lines, we sought to identify compounds that were effective in inhibiting (1) ATC lines harboring certain mutations (BRAFV600E, KRAS, PI3KCA); (2) ATC lines harboring wildtype BRAF; and (3) all lines regardless of mutational status.

Table 4.1.1. Mutations and morphology of anaplastic thyroid carcinoma cell lines.

Cell Line	Notable Mutations	Morphology
THJ-11T	*KRAS c.G35T, TP53 c.G733A, TERT c.C228T* and c.*T349C*	Squamoid; macrofollicular, compact spheroids
THJ-16T	*PI3KCA c.G1633A, TP53 c.G818A, TERT c.C228T, MKRN1-BRAF* fusion	Spindle; large, macrofollicular, compact spheroids
THJ-21T	*BRAF c.T1799A, TP53 c.G839C, TERT c.C228T* and c.*T349C*	Spindle; invasive and loosely associated spheroids
THJ-29T	*TP53 c.C310T* and *TERT c.C250T*	Spindle/giant; large, invasive, loosely associated spheroids

We first executed a screen of 1567 compounds from three established libraries: NCI Approved Oncology Drug Set VI, FDA-Approved Drug Collection, and the Anti-Cancer Compound Library. Five concentrations of each compound were tested in the four cell lines in monolayer culture (Figure 4.1.2.A), and results were reported as area under the curve (AUC). As expected, many compounds did not significantly inhibit growth in any of the four ATC lines and clustered at the far right of the plot (Figure 4.1.2.B). However, we were able to confirm the inhibitory effects of currently used therapeutics such as paclitaxel, doxorubicin, and trametinib (blue-Figure 4.1.2.B). Notably, tyrosine kinase inhibitors lenvatinib and sorafenib were not broadly effective across the four lines (Figure 4.1.2.B). For prioritization, drug hits were identified as those with the lowest AUC and lowest standard deviation in AUC. In total, we identified 62 compounds of interest to perform a follow-up confirmation screen. Drug classes represented in the 62 prioritized compounds include inhibitors of HSP90, HDAC, and proteasomes, all have which have been investigated for the treatment of ATC in recent years[160]. Our results confirm the importance of these pathways in ATC and their identification provided increased confidence in the results of our broad screen.

4.1.5.1.1. Confirmation screen allows for IC50 calculation and prioritization

To further prioritize compounds for more in-depth follow-up, we generated dose response curves for 62 compounds in monolayer culture of the four ATC cell lines (Figure 4.1.3.). Following confirmation of efficacy, we evaluated compounds based on potency, clinical trial success, previous relevance in ATC, and target redundancy. This resulted in removal of 22 compounds, including emetine (an emetic), disulfram (Antabuse, a treatment for alcohol dependence), and four of seven HSP90 inhibitors. Finally, we were left with 40 priority drugs to compare in monolayer and spheroid cultures.

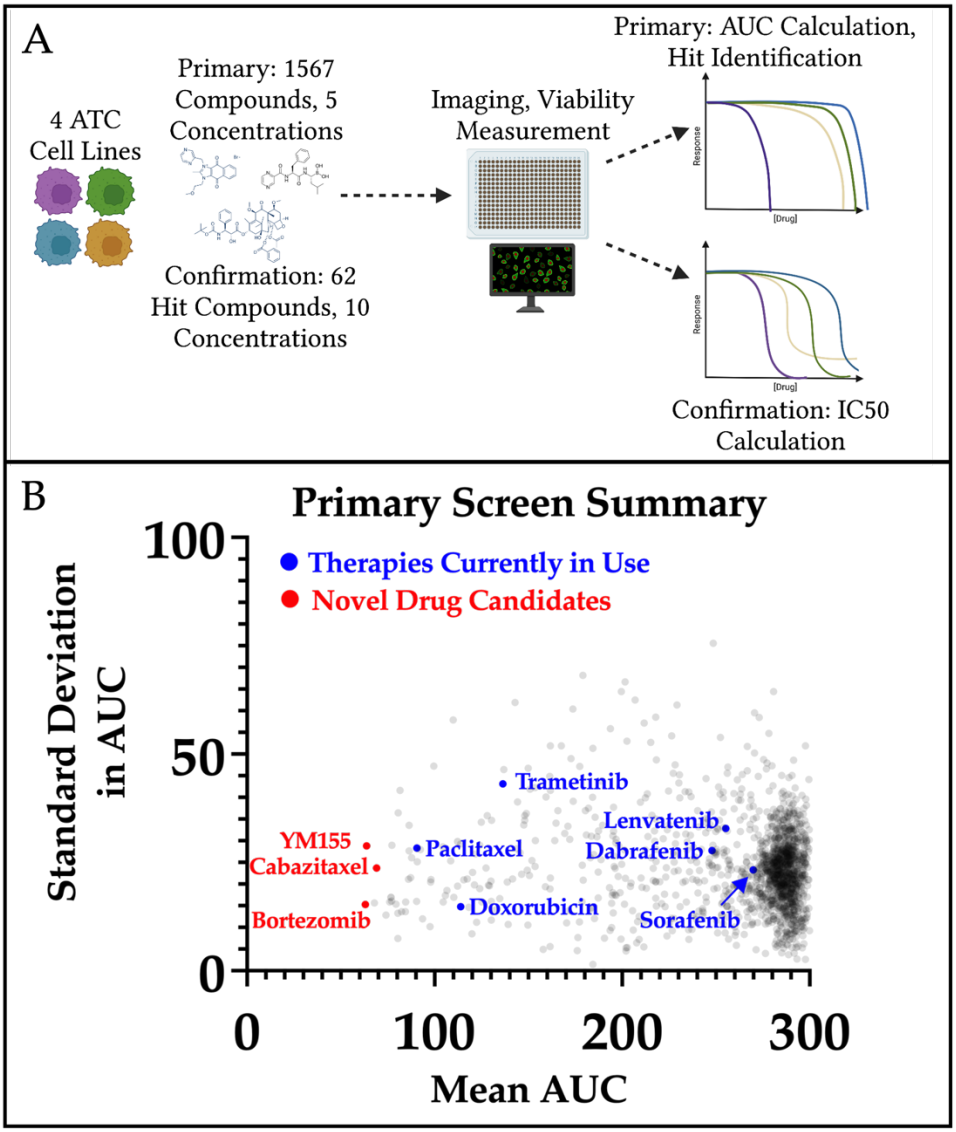

Figure 4.1.2. Workflow and results of primary compound screen. A. Schematic of plating, treating, and analysis for the primary compound screen. The four ATC cell lines (THJ-11T, THJ-16T, THJ-21T, and THJ-29T) were plated in 384-well tissue culture plates. After a 24-hour incubation, 1567 compounds were added to plates at five concentrations (5.14µM, 1.09µM, 156nM, 30.8nM, 6.2nM). Plates were incubated for 3 days prior to staining for the nucleus and dead/dying cells and imaging. B. Summary results for primary compound screen. Curves were generated for each compound (for each cell line), and average area under the curve (AUC) and standard deviation across the four lines were calculated for each compound. Therapies that are currently in use or clinical trial are denoted by blue points, and compounds that showed low AUC and low standard deviation are denoted by red points.

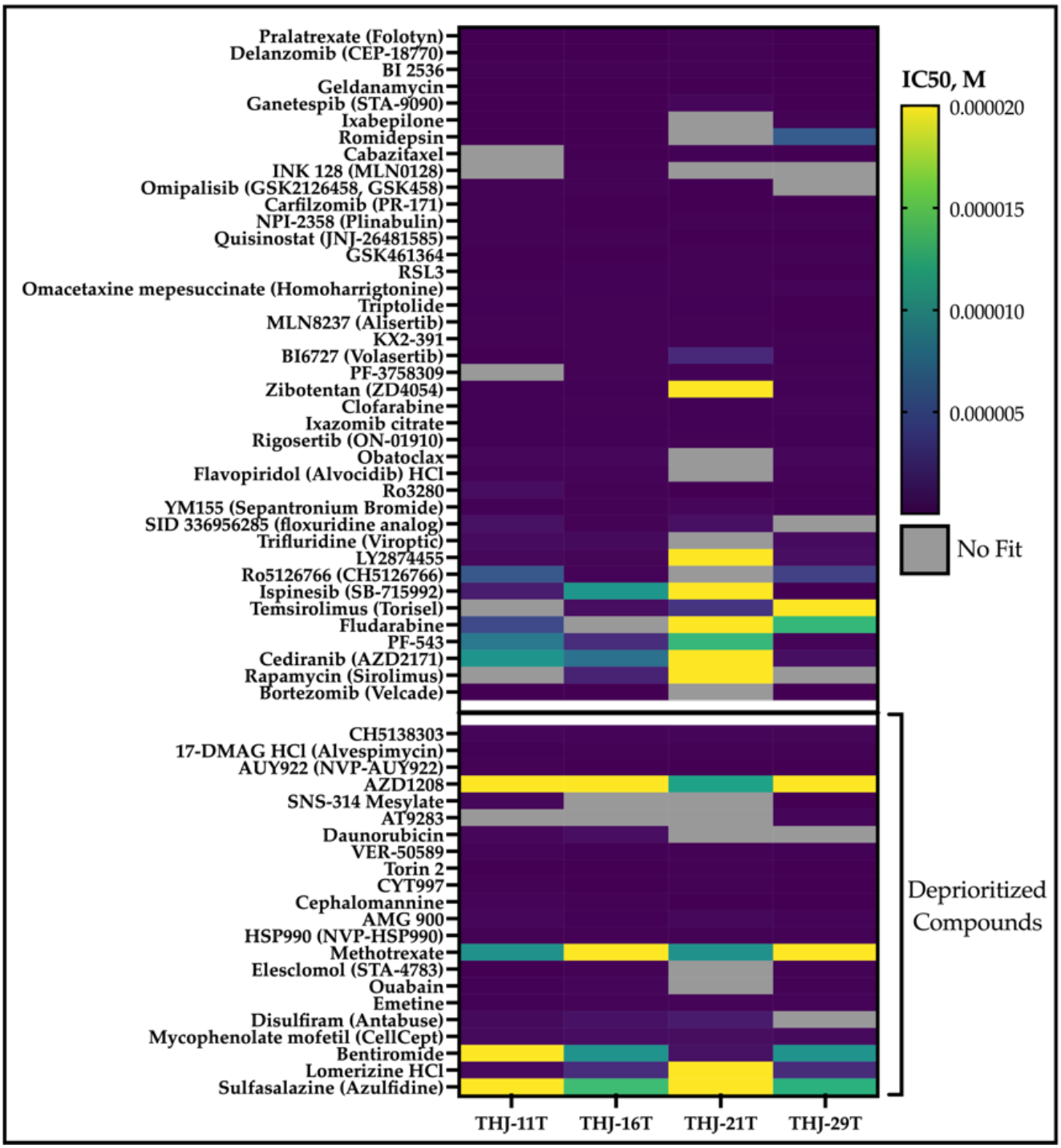

Figure 4.1.3. Summary of confirmation screen. Ten concentrations of each compound were plated with each of the four ATC cell lines and incubated for 3 days prior to imaging to detect nuclei and dead cells. High potency (low IC50) drugs are denoted in purple, and lower potency drugs are denoted in the green/yellow cells. Cells are shaded in grey if no curves could be generated to fit the collected data. Drugs that exhibit target redundancy, lack of current clinical availability, and/or known futility in ATC are graphed separately as Deprioritized Compounds.

4.1.5.2. Three-Dimensional Culture Identifies Compounds with Differential Efficacy

4.1.5.2.1. Value of spheroids in drug screening

Spheroids are three-dimensional cell structures composed of a single cell source. We previously reported the development and characterization of multiple thyroid cancer spheroid lines, as well as the methods for adapting them to high-throughput formats. Briefly, our spheroids are derived from monolayer cultures and form when plated in low-attachment or cell-repellent plates in as little as 2% Matrigel. Structures can vary in size and morphology, with THJ-16T spheroids being relatively large (200–400μm) and compact and THJ-21T spheroids being smaller (50–100μm) and less cohesive. While these differences cause concern for issues of drug penetrance, we do not observe any correlation between spheroid size and consistently diminished potency or efficacy in three-dimensional cultures. As spheroids more accurately recreate nutrient and oxygen gradients that occur in vivo, they are believed to better represent patient responses to therapeutics. Due to the cost and time associated with spheroid screens, we understand that they are not viable options for many initial screens. However, in adapting these cultures to a high-throughput format to decrease time required and using a minimal Matrigel content to reduce costs, we aim to enhance the feasibility and translatability of these data.

4.1.5.2.2. Comparing monolayer and spheroid drug responses to inform future studies

We tested our 40 priority drugs, which were identified following deprioritization of 22 drugs from the confirmation screen, in all four ATC cell lines in both monolayer and spheroid cultures to identify those with altered efficacy in three-dimensions (Figure 4.1.4.A-C). The activity area (area over the dose–proliferation response curve) for each drug in each cell line indicated 7 compounds with decreased inhibitory activity in spheroid culture when compared to the corresponding monolayer culture in at least three ATC cell lines (Figure 4.1.4.D). The remaining 33 compounds showed relatively good potency and 3D inhibitory activity. Of these, we identify three drugs that have high potential for translation to clinical trial: bortezomib, a proteasomal inhibitor; cabazitaxel, a derivative of docetaxel; and YM155, a survivin inhibitor (highlighted in red, Figures 4.1.2.B, 4.1.4.D).

While all 33 drugs with good 3D efficacy have potential therapeutic utility, we identify three with exceptional potency across all four ATC lines. Bortezomib had the highest potential for therapeutic efficacy overall. Of all the drug classes included in this study, proteasome inhibitors (bortezomib, ixazomib, delazomib, carfilzomib) demonstrated some of the highest potency across all four ATC lines. While bortezomib demonstrated a slightly decreased response in spheroids, it still showed the highest potency of all drugs evaluated. Beyond the proteasome inhibitors, two additional potent drugs showed 3D efficacy in at least two of the four ATC lines, cabazitaxel and YM155. Of note, all three drugs were among the 10 top compounds identified in our initial screen (Figure 4.1.2.B) based on the sum of observed activity areas across each of the four ATC cell lines.

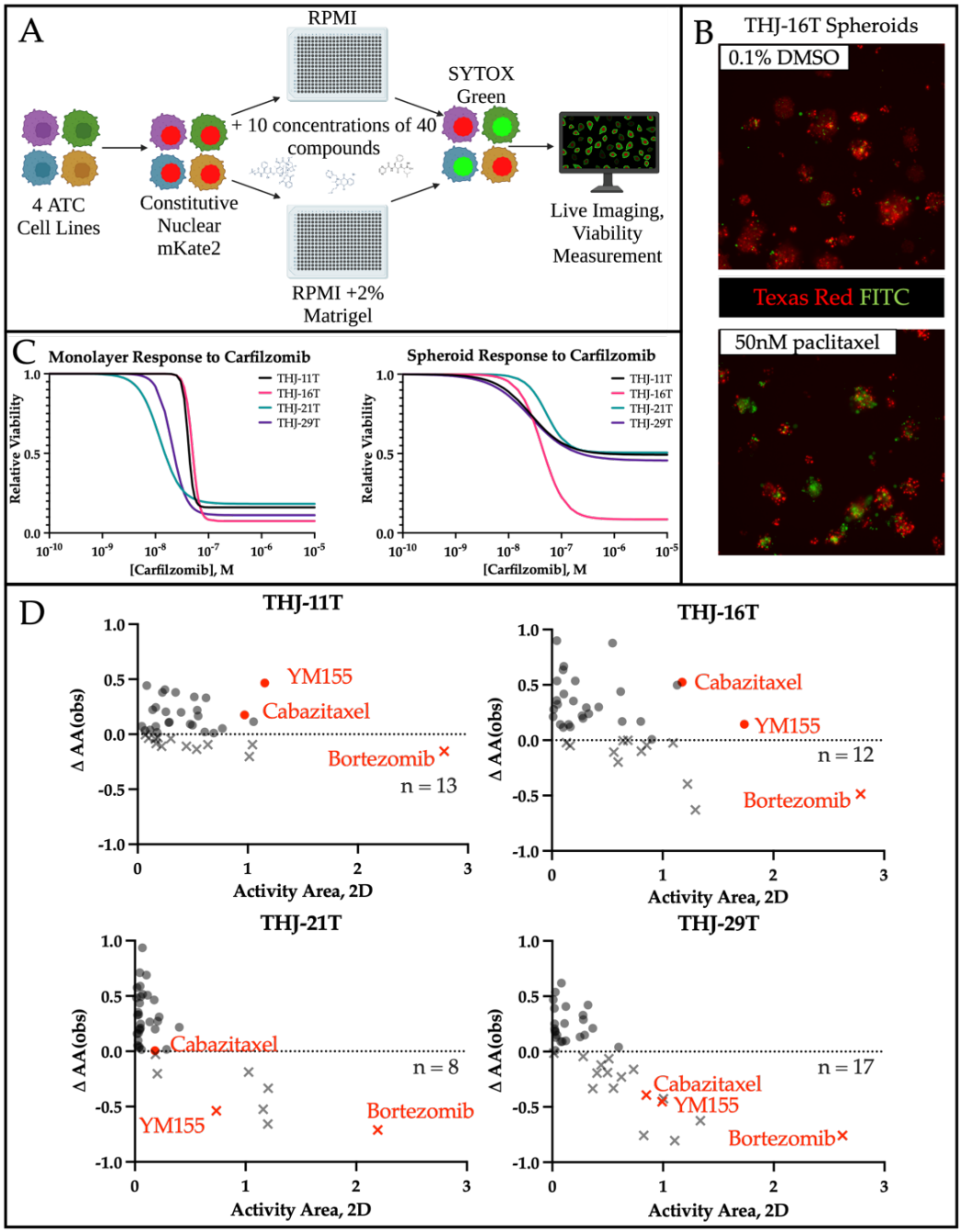

Figure 4.1.4. Inclusion of spheroids in drug screening workflows identifies drugs with culture-format dependent effects. A. Schematic of workflow for the monolayer vs. spheroid screen. B. ATC cell lines were infected with lentiviruses to express nuclear mKate2 (Texas Red channel) prior to plating in 384 well plates and treating with 40 priority compounds over a range of 10 concentrations. SYTOX Green was included to mark dead or dying cells (FITC channel, green). With DMSO treatment, baseline cell death can be observed at the margins of each spheroid. When treated with 50nM paclitaxel, the ratio of dead to live cells visibly increases. C. Example of a differential response to carfilzomib. Left panel, monolayer responses to carfilzomib show near 100% efficacy in all 4 lines. However, when the same cells are plated in 2% Matrigel to form spheroids (right panel), this efficacy is lost in 3 of the 4 cell lines. THJ-11T, THJ-21T, and THJ-29T retained approximately 50% viability after 72 hours of treatment with up to 10uM carfilzomib. D. Comparison of 2D and 3D culture re-sponse. Positive values (circles) represent drugs with retained/enhanced inhibition in spheroids, while negative values (Xs) indicate drugs that demonstrate greater inhibitory activity in monolayer cultures. Counts represent the number of drugs (of the 40 drugs tested) that exhibit decreased inhibition in spheroids.

4.1.6. Discussion and Conclusion

Three-dimensional cultures have been shown to produce differential drug responses compared to corresponding monolayer culture. They also more accurately recreate the nutrient and oxygen gradients seen in tumors in vivo. As such, a major goal of this study was to identify novel therapeutics for anaplastic thyroid carcinoma with retained or enhanced efficacy in spheroids that may have been overlooked in monolayer screens. We utilized four unique spheroid cultures that represent a range of mutations commonly observed in ATCs to narrow the scope and list of potential therapeutic candidates from a screen of 1567 drugs. As a result, we identified multiple broadly effective therapeutic candidates that retain inhibitory activity in 3D cultures.

The vast majority of preclinical drug screening occurs in monolayer culture, as it has been the standard for decades and is highly accessible and amenable to many formats. However, with the current anti-cancer drug attrition rate of up to 95%, there is a clear need for improvement of our preclinical models of disease and their utilization in the drug development pipeline[170-172]. Many improvements have been made in animal models of disease, from primary xenograft models, spontaneous tumor models, and even humanized mice. However, these models are very expensive and require significant time and resources to maintain for drug studies. Our spheroid screening methodology represents a cost-effective intermediate between monolayer screening and animal tumor models.

There are currently no approved targeted treatments that are effective in BRAF-wildtype ATC. Even with the most aggressive surgical, radiation, and chemotherapeutic interventions, most patients die within 5 years [173,174]. Herein, we describe multiple compounds that demonstrate efficacy in three BRAF-wildtype lines with various driver mutations and one BRAF-mutant ATC line. Based on the initial screening data and support from follow-up three-dimensional studies, we have chosen to highlight three compounds with exceptional promise for future development: bortezomib, cabazitaxel, and YM155. All three were identified in the top 10 compounds based on total observed activity area. Bortezomib was chosen based upon having the highest consistent overall

efficacy and potency; cabazitaxel has potential to improve on a current treatment for ATC (paclitaxel); and YM155 has been previously shown to inhibit ATC xenograft tumors in vivo.

Bortezomib (PS-341) is an inhibitor of the 20S core catalytic component of the 26S proteasome, which leads to accumulation of polyubiquitinated proteins and eventual apoptosis of rapidly dividing cells[175,176]. Bortezomib is currently FDA-approved for use in patients with treatment-resistant multiple myeloma and has demonstrated a manageable side-effect profile when given in an outpatient setting[177-179]. Bortezomib has been previously evaluated in anaplastic thyroid carcinoma, causing G(2)-M cell cycle arrest, sensitization to BRAFV600E-inhibitor vemurafenib, and altered tumor metabolism in vivo[180-182].

Cabazitaxel is a microtubule inhibitor similar to paclitaxel, which is currently used in palliative care for ATC patients[183,184]. Cabazitaxel is an exciting new therapeutic, as it exhibits a lower affinity to p-glycoprotein (Pgp, MDR1), which is known to mediate resistance to other taxanes, including paclitaxel[185]. As increased expression of MDR1 has been described in ATCs, cabazitaxel is likely to be more effective than paclitaxel in the treatment of ATCs[186]. This is supported by the results of our primary drug screen, where cabazitaxel demonstrated a consistently lower AUC across all four ATC cell lines than paclitaxel (Figure 4.1.2.B). Cabazitaxel has demonstrated efficacy in metastatic taxane-resistant prostate and breast cancers but has not yet been evaluated in the treatment of ATC to our knowledge[187,188].

The final compound, YM155 (sepantronium bromide), is a potent inhibitor of the survivin promoter, with an IC50 of less than 1nM[189]. Survivin is a member of the Inhibitor of Apoptosis family of proteins and has been shown to be significantly upregulated in all thyroid cancers[190]. Evaluation of ATCs has indicated that survivin is not only generally dysregulated, but has distinct nuclear localization not seen in more indolent tumor types[191]. Finally, YM155 has been characterized by others as a potential therapeutic for ATC, initiating cell cycle arrest in vitro and inhibiting the growth of ATC lung metastases in a murine xenograft model[192,193].

In demonstrating the importance of including three-dimensional cultures in a high-throughput compound screening workflow, we have identified 33 promising therapeutic candidates for anaplastic thyroid

carcinoma. While each of these will require further investigation prior to clinical studies, many have already successfully cleared safety testing and are in clinical trials for other tumor types. Additionally, our three lead candidates identified based on their overall potency and retained efficacy in 3D culture show promising therapeutic efficacy for ATC based on recent publications showing efficacy in mouse models, current use of the parent drug, and known relevant molecular alterations. The independent identification of compounds that have shown efficacy in separate studies using more costly mouse models of ATC validates the utility of our screening methodology. The benefits of this study are two-fold: 1) we have generated a substantial list of potentially useful drugs that already have FDA-approval and/or a history of use that can be further explored in follow up studies of ATC in vivo; and 2) we have identified three lead drug candidates that have evidence of in vivo efficacy and may be rapidly moved into clinical trials.

CHAPTER V.

SYNOPSIS AND FUTURE DIRECTIONS

5.1. Summary

Thyroid cancer is an understudied malignancy, despite its rising prevalence. ATCs are the most aggressive endocrine neoplasms, and the lack of understanding of ATC pathogenesis has created a significant lack of treatment options. Through the course of my thesis work, I have generated novel spheroid, organoid, and murine xenograft models of thyroid carcinoma, and developed many downstream applications for those model systems, including high-throughput drug screening and immunofluorescence. These models will allow for more accessible and in-depth study of PTC and ATC pathogenesis, behavior, and treatment options. Prior to these studies, the only available model systems were monolayer cell culture and murine models, both of which have many caveats that decrease the translatability to patient treatment.

I have created immune-spheroid co-cultures, characterized the immune infiltrate associated with aggressive PTCs, and established an immune-humanized murine model of ATC to be used in future studies of the thyroid tumor microenvironment. Current understanding of ATC pathogenesis does not account for alterations and impact of the tumor microenvironment, though the tumor microenvironment has been implicated in aggressive behavior and progression in many cancers. As we identified elevated levels of Wnt ligands that drive dedifferentiation of PTC, studies of the tumor microenvironment may reveal the source of those ligands. Currently ongoing studies with the Weiss lab are incorporating immune infiltrate in predictive models of poor outcome.

Using spheroid and organoid cultures, I have identified over thirty potential therapeutics that can be incorporated into clinical trials for patients who currently have few treatment options. We have already established a collaboration with an oncologist who is proposing a clinical trial of bortezomib in ATC, which will begin as early as summer 2022. The identification of Wnt signaling as a driver of dedifferentiation has also revealed a druggable target with the potential to prevent dedifferentiation or inhibit growth and metastasis of these incredibly aggressive tumors.

5.1.1. Significance

5.1.1.1. Importance of the problem.

Thyroid cancer incidence is rising, with over 50,000 new cases predicted to be diagnosed this year. Mathematical models predict that by 2030, thyroid cancer will replace colorectal cancer as the fourth leading cancer diagnosis. While the majority of patients respond well to first line treatments such as radioactive iodine and surgery, approximately 20% will experience recurrence, and 10% will develop metastatic disease. Once tumors progress to this point, treatment options are very limited. Only 25% of anaplastic thyroid carcinomas (ATCs) carry BRAF mutations, which allow them to be treated with the recently FDA-approved combination of dabrafenib (mutant BRAF-specific inhibitor) and trametinib (MEK inhibitor). Trametinib was added to this

therapy regimen to prevent paradoxical MEK activation and thus limit resistance, but the complete response rate is still only a dismal 8% in BRAF-mutant ATC. This work has defined the role of Wnt signaling in thyroid cancer pathogenesis, identified 33 promising drug candidates, and paved the way for new therapeutic interventions for patients with aggressive disease.

5.1.1.2. Advancement of scientific knowledge.

The role of Wnt/β-catenin in the development of colorectal cancer has been well defined, but there is a lack of understanding of the role of Wnt in the pathogenesis of aggressive thyroid cancers. The major goals of this project were to develop novel model systems to enhance translatability, define the tumor immune microenvironment and role of Wnt signaling in thyroid carcinomas, and investigate potential therapeutics (including Wnt inhibitors) in the treatment of anaplastic thyroid cancer. To our knowledge, these studies are the first to investigate Wnt inhibitors as potential therapeutics for thyroid cancer, with the potential to impact treatment for thousands of patients. Finally, the model systems developed to complete these studies can be utilized by the field as a whole to elucidate the pathogenesis of aggressive PTC and ATC, as well as establish improved therapies.

5.1.2. Innovation

These studies represent significant collaborative, intellectual, and technical innovation. In bringing together individuals with expertise in thyroid cancer, Wnt/β-catenin signaling, high-throughput screening, and murine models of disease, we have been able to gain diverse perspectives and incorporate a number of approaches to answer our research questions. Moreover, we bring together clinicians and researchers to implement solutions that are clinically relevant and can be rapidly translated into practice. Finally, while we have access to a large patient population willing to participate in sequencing studies, we have also expanded our cohort through collaboration with the University of Washington.

As mentioned in the introduction, research for thyroid cancers lags substantially behind that of other cancers, likely due to the success of RAI therapy, rarity of ATC, and/or the perceived ease of total thyroidectomy (despite leaving patients dependent on levothyroxine for the remainder of their life). We recognized this lack of attention and seek to address this disparity. There is currently no personalized medicine available for thyroid cancer, despite the practice becoming the golden standard for many comparable tumor types. Sequencing studies and establishment of high-throughput patient-derived organoid workflows open the door to personalized medicine for these patients, representing a major advance in treatment.

Finally, these studies are highly technologically innovative, as we combine sequencing, high-throughput automated drug screening, patient-derived organoid cultures, murine xenograft models, and multiple spheroid models of both PTC and ATC. These methods allow us to be more well-informed during the planning stages and have allowed for a greatly expedited timeline for the completion of my aims. We have focused heavily on model system development to advance the field and enhance the translatability of our findings. Our studies have already have generated interest in a clinical trial of bortezomib in ATC patients, with the potential to initiate many more.

5.1.3. Limitations

While our data is certainly exciting, there are remaining limitations that must be kept in mind. Relating to the organoids, there is concern about the transformation and loss of cells over time. We have kept our culture media as simple as possible to prevent biasing the cell populations that survive after an FNA or in culture. However, there is most certainly loss of cell populations due to lack of stimulation (immune cells), competition for nutrients (especially with fibroblast outgrowth), and/or lack of proper nutrients within the media.

In characterizing the tumor-immune microenvironment using CIBERSORT, TIMER, and TIDE, we must keep in mind that it is based on bulk RNA-sequencing, rather than single-cell RNA sequencing. As such, we are not able to determine the localization or activity of specific cells within a given sample. Instead, we must

compare immunohistochemistry to our computational findings and perform assays with corresponding organoid cultures to draw meaningful conclusions. Future scRNA studies would be an exciting complement to the bulk-sequencing data, especially given the potential link between stromal and immune cell localization and Wnt expression.

Many of the promising therapeutic candidates require further characterization prior to clinical translation. Of our three highest priority compounds, bortezomib and YM155 have already shown efficacy in murine models of ATC, and the mechanism has been defined. Cabazitaxel is similar to paclitaxel, which is currently used in palliative care for ATC, but it has not been tested in any other preclinical models of ATC to our knowledge. The other thirty drugs require additional studies to determine relevance to molecular drivers of ATC and efficacy in preclinical disease models.

Finally, there are several limitations with our murine models of thyroid cancer, including the immune humanized mice. While these models are an improvement on immunocompromised mice, they do not produce human cytokines capable of supporting immune cell populations long term. This may result in enhanced trafficking to the tumor as the only other source of human cytokines within the mouse, which would not be reflective of what occurs in a fully human system. For this reason, it is important to combine both organoid and murine studies to produce a more complete picture of what happens in patient tumors.

5.2. Future Directions

5.2.1. Further Drug Identification and Clinical Trials

While we have identified many potential drug candidates, there are many others that have not yet been explored as potential therapeutics for ATC. We only utilized three drug libraries in our high-throughput screen, and there are dozens more. Another iteration of that screen with other drug libraries included could potentially identify novel drivers of ATC and new classes of inhibitors that may be clinically relevant. At this time, we only

sought to identify therapeutics that can be rapidly translated into the clinic, so clinical trials are the logical next step. The majority of our drugs identified in 4.1 have passed safety and clinical tolerability trials, and under the Right to Try Law of 2018, the FDA may grant permission for experimental use in just a matter of days, rather than waiting for completion of a full clinical trial. Clinical trials are notoriously difficult in ATCs due to the rapid growth and short median survival time. As previously mentioned, we have at least one clinician interested in a clinical trial of bortezomib for ATC, and I believe others will follow. ATCs are so aggressive that patients are suffocating or bleeding into their trachea due to invasion into their airway, and current therapies are not able to make a significant impact for these patients. There is an incredible need for new therapeutics, and in using our spheroid culture systems in a screening methodology, we have laid the foundation for dozens of research projects and clinical trials.

5.2.2. Further Elucidation of the Role of Wnt in PTC Transformation

While we have identified Wnt signaling as a critical part of ATC pathogenesis, further work is necessary to delineate the role of Wnt in the transformation of PTC into ATC. We have established that Wnt stimulation via CHIR99021 or LWRN media alters PTC morphology and behavior. A critical next step would be RNA-sequencing of Wnt-treated PTC lines or organoids for comparison to RNA-sequencing of our ATC lines/organoids. We know that ATCs have very distinct expression profiles that allow them to be identified computationally, and I imagine that Wnt-treated PTCs would fall between the original PTCs and untreated ATCs.

5.2.3. Refining Wnt Inhibition for Clinical Use

Our studies were performed using pyrvinium as a Wnt inhibitor because it is currently FDA-approved as an orphan drug and would therefore have the quickest route to use in patients. However, pyrvinium does have some bioavailability and safety concerns. Pyrvinium was originally used as an anti-pinworm drug, where it would primarily need to function within the gastrointestinal (GI) tract. This is ideal for pyrvinium, as it has a low oral

bioavailability and will remain in the GI system to have the largest impact therein. This is also taken advantage of in the treatment of familial adenomatous polyposis, which occurs in the colon. To my knowledge, pyrvinium has never been tested in any method of administration other than oral (intravenous, subcutaneous, etc.). In our murine studies, we administered pyrvinium in corn oil intraperitoneally and observed anti-tumor effects, in addition to some toxicity. As pyrvinium is fat soluble, we noted that many of our smaller mice were most susceptible to treatment-induced toxicities, including seizures. Colons were collected following experiments and we did not observe any induction of colitis, though these studies were performed in immunocompromised mice.

There are many other Wnt inhibitors available, including one (SSTC3), that has a similar mechanism of action to pyrvinium (CK1a agonist). SSTC3 requires higher dosing to achieve similar effects, but it is believed to have higher oral bioavailability and a lower toxicity profile. Another lead Wnt inhibitor is LGK-974, a porcupine inhibitor. LGK-974 inhibits the release of Wnt ligand, which, given our data on Wnt ligands in the tumor microenvironment, is highly relevant. Due to the need for a complete and intact microenvironment to observe effects of Wnt ligand inhibition, we have had difficulty characterizing the therapeutic potential of LGK-974 in our models. We do not see significant inhibition of our spheroids, which do not have the fibroblasts that we believe are producing many of the critical Wnt ligands. Future work will need to utilize either fibroblast-spheroid co-cultures, organoids, or murine models to characterize this inhibitor.

Finally, we recognize that the level of Wnt induction in ATCs is variable, and as such, some tumors may not respond to Wnt inhibition. Future studies should utilize our patient sequencing data and corresponding patient-derived organoid cultures to identify characteristics of organoid lines that are Wnt-inhibitor responders or non-responders. I hypothesize that those with low basal Wnt signaling may not be susceptible to Wnt inhibitor treatment, and those tumors may have smaller stromal compartments. Poorly differentiated thyroid carcinoma (PDTC) is a similar de-differentiated thyroid cancer that does not have the large stromal content seen in ATCs, and PDTCs also lack the distinct Wnt profile of ATC. Currently ongoing work in the lab is examining the

relationship between the stroma and Wnt signaling, and I think this characterization will be important to keep in mind when we translate Wnt inhibitors to the clinic.

5.2.4. Tumor Microenvironment Studies

Given the increased Wnt ligands, positive β-catenin staining of the stroma in the murine xenografts of ATC, and immune exclusion seen in PTCs, it is clear that there is a relationship between the tumor microenvironment and the importance of Wnt to tumor behavior. We have many ongoing projects investigating cancer-associated fibroblasts (CAFs) and monocytes, as well as the significance of immune infiltrate in predicting future poor outcome in PTCs. Tumor-derived Wnt could be recruiting immune cells and/or fibroblasts to the tumor microenvironment to aid in immune evasion, and microenvironment derived Wnt could be promoting aberrant tumor behavior. While we focused on the latter for this study, Wnt has been shown to modulate cytokine production, and the effects of tumor Wnt ligand production on cellular recruitment would be very interesting.

5.2.5. Personalized Medicine Approaches for Thyroid Cancer

As mentioned in the introduction, while personalized medicine is quickly becoming the standard across many cancer types, there is no incorporation of personalized medicine into care for any thyroid cancer. As part of my work, we have now developed PDO cultures that have been shown to more accurately capture patient tumor responses and can be adapted to high-throughput growth formats and drug screening. While further work is needed to identify the ideal media conditions to allow for quick, non-selective growth of the organoids for rapid expansion to enable testing, we have laid the groundwork for personalized medicine in, at the least, PTC and ATC.

REFERENCES

1. Rahib L, Smith BD, Aizenberg R, Rosenzweig AB, Fleshman JM, Matrisian LM. (2014). Projecting cancer incidence and deaths to 2030: the unexpected burden of thyroid, liver, and pancreas cancers in the United States. Cancer Res 74: 2913-2921.

2. Howlader, N., Noone, A.M., Krapcho, M., Miller, D., Brest, A., et al. (eds). SEER Cancer Statistics Review, 1975-2016, National Cancer Institute. Bethesda, MD, https://seer.cancer.gov/csr/1975_2016/, based on November 2018 SEER data submission, posted to the SEER web site, April 2019.

3. Goldfarb, M., Casillas, J. (2014). Unmet information and support needs in newly diagnosed thyroid cancer: comparison of adolescents/young adults (AYA) and older patients. J Cancer Surviv 8(3):394-401.

4. Lubitz, C., Kong, C., McMahon, P., Daniels, G., Chen, Y., Economopoulos, K., Gazelle, G., Weinstein, M. (2014). Annual financial impact of well-differentiated thyroid cancer care in the United States. Cancer 120(9):1345-1352.

5. Wang, J., Liu, J., Pan, H., Jiang, C., Liu, S., Zhu, Z., Fang, J., Zheng, X., Hong, S., Wang, S. (2018). Young age increases the risk of lymph node positivity in papillary thyroid cancer patients: a SEER data-based study. Cancer Manag Res 10:3867-3873.

6. Abdullah, M., Junit, S., Ng, K., Jayapalan, J., Karikalan, Hashim, O. (2019). Papillary thyroid cancer: genetic alterations and molecular biomarker investigations. Int J Med Sci 16(3):450-460.

7. Bresciani, L., Orlandi, E., Piazza, C. (2019). Radiation-induced papillary thyroid cancer: is it a distinct clinical entity? Curr Opin in Otolaryngology and Head and Neck Surgery 27(2):117-122.

8. Iglesias, M., Schmidt, A., Al Ghuzlan, A., Lacroix, L., Vathaire, F., Chevillard, S., Schlumberger, M. (2017). Radiation exposure and thyroid cancer: a review. Arch Endocrinol Metab 61(2):180-187.

9. Lee, K., Anastaspoulou, C., Chandran, C., Cassaro, S. (2021). Thyroid Cancer. StatPearls. July 19, 2021 Update.

10. Xing, M. (2013). Molecular pathogenesis and mechanisms of thyroid cancer. Nat Rev Cancer 13(3): 184-199.

11. Tang, K., Lee, C. (2010). BRAF mutation in papillary thyroid carcinoma: pathogenic role and clinical implications. J Chin Med Assoc 73(3):113-128.

12. Howell, G., Hodak, S., Yip, L. (2013). RAS mutations in thyroid cancer. Oncologist 18(8):926-932.

13. Xing, M. (2016). Clinical utility of RAS mutations in thyroid cancer: a blurred picture now emerging clearer. BMC Medicine 14:12.

14. Hussein, O., Abdelwahab, K., Hamdy, O., Awny, S., Megahed, N., Hafez, M., Abdelaziz, M., Gaballah, K., Abdelkhalek, M. (2020). Thyroid cancer associated with Hashimoto thyroiditis: similarities and differences in an endemic area. J Egypt Natl Canc Inst 32:7.

15. Selek, A., Cetinarslan, B., Tarkun, I., Canturk, Z., Ustener, B., Akyay, Z. (2017). Thyroid autoimmunity: is really associated with papillary thyroid carcinoma? Head and Neck 274:1677-1681.

16. Fullmer, T., Cabanillas, M., Zagereo, M. (2021). Novel therapeutics in radioactive iodine-resistant thyroid cancer. Front Endocrinol 12:720-723.

17. Limaiem, F., Kashyap, S., Naing, P., Giwa, A. (2021). Anaplastic thyroid carcinoma. StatPearls July 20, 2021 Update.

18. Fearon, E., Vogelstein, B. (1990). A genetic model for colorectal tumorigenesis. Cell 61(5):759-767.

19. Nikitski, A., Rominski, S., Condello, V., Kaya, C., Wankhede, M., Panebianco, F., Yang, H., Altschuler, D., Nikiforov, Y. (2019). Mouse model of thyroid cancer progression and dedifferentiation driven by STRN-ALK expression and loss of p53: evidence for the existence of two types of poorly differentiated carcinoma. Thyroid 29(10):1425-1437.

20. Song, S., Lee, D., Kim, H., Jeong, W. (2020). Coexistent papillary thyroid carcinoma and its anaplastic transformation in a cervical lymph node metastasis. Int J Thyroidol 13(1):55-59.

21. Odate, T., Oishi, N., Kawai, M., Tahara, I., Mochizuki, K., Akaishi, J., Ito, K., Katoh, R., Kondo, T. (2021). Progression of papillary thyroid carcinoma to anaplastic thyroid carcinoma in metastatic lymph nodes: solid/insular growth and hobnail cell change in lymph nodes are predictors of subsequent anaplastic transformation. Endocr Pathol 32:347-356.

22. Smallridge, R., Ain, K., Asa, S., Bible, K., Brierley, J., Burman, K., Kebebew, E., Lee, N., Nikiforov, Y., Rosenthal, M., Shah, M., Shaha, A., Tuttle, R.-American Thyroid Association Anaplastic Thyroid Cancer Guidelines Taskforce. (2012). American Thyroid Association guidelines for management of patients with anaplastic thyroid cancer. Thyroid 22(11):1104-39.

23. Liu, R., Xing, M. (2017). TERT promoter mutations in thyroid cancer. Endocr Rel Cancer 23(3):R143-R155.

24. Lai, W., Liu, C., Lin, S., Chen, C., Hang, J. (2020). Characterization of driver mutations in anaplastic thyroid carcinoma identifies RAS and PIK3CA mutations as negative survival predictors. Cancers (Basel) 12(7):1973.

25. Garcia-Rostan, G., Tallini, G., Herrero, A., D'Aquila, T., Carcangiu, M., Rimm, D. (1999). Frequent mutation and nuclear localization of β-catenin in anaplastic thyroid carcinoma. Cancer Res 59(8):1811-1815.

26. Kurihara, T., Ikeda, S., Ishizaki, Y., Fujimori, M., Tokumoto, N., Hirata, Y., Ozaki, S., Okajima, M., Sugino, K., Asahara, T. (2004). Immunohistochemical and sequencing analyses of the Wnt signaling components in Japanese anaplastic thyroid cancers. Thyroid 14(12):1020-1029.

27. Zhan, T., Rindtorff, N., Boutros, M. (2017). Wnt signaling in cancer. Oncogene 36:1461-1473.

28. Subbiah, V., Kreitman, R., Wainberg, Z., Cho, J., Schellens, J., Soria, J., Wen, P., Zielinski, C., Cabanillas, M., Urbanowitz, G., Mookerjee, B., Wang, D., Rangwala, F., Keam, B. (2018). Dabrafenib and trametinib treatment in patients with locally ad-vanced or metastatic BRAF V600-mutant anaplastic thyroid cancer. J Clin Oncol 36(1):7-13.

29. Subbiah, V., Kreitman, R., Wainberg, Z., Cho, J., Schellens, J., Soria, J., Wen, P., Zielinski, C., Cabanillas, M., Boran, A., Palanichamy, I., Burgess, P., Romero Salas, T., Keam, B. (2022). Dabrafenib plus trametinib in patients with BRAF V600E-mutant anaplastic thyroid cancer: updated analysis from the phase II ROAR basket study. Ann Oncol (in press).

30. Cargnello M, Roux PP. (2011). Activation and function of the MAPKs and their substrates, the MAPK-activated protein kinases. Microbiol Mol Biol Rev. 75(1):50-83.

31. Tran NH, Wu X, Frost JA. (2005). B-Raf and Raf-1 are regulated by distinct autoregulatory mechanisms. J Biol Chem. 280(16):16244-16253.

32. Davies H, Bignell GR, Cox C, et al. (2002). Mutations of the BRAF gene in human cancer. Nature. 417(6892):949-954

33. Turski ML, Vidwans SJ, Janku F, et al. (2016). Genomically Driven Tumors and Actionability across Histologies: BRAF-Mutant Cancers as a Paradigm. Mol Cancer Ther. 15(4):533-547.

34. Tsimberidou AM, Iskander NG, Hong DS, et al. (2012). Personalized medicine in a phase I clinical trials program: the MD Anderson Cancer Center initiative. Clin Cancer Res. 18(22):6373-6383.

35. Nikiforova MN, Nikiforov YE. (2009). Molecular diagnostics and predictors in thyroid cancer. Thyroid. 19(12):1351-1361.

36. Adeniran AJ, Zhu Z, Gandhi M, et al. (2006). Correlation between genetic alterations and microscopic features, clinical manifestations, and prognostic characteristics of thyroid papillary carcinomas. Am J Surg Pathol. 30(2):216-222.

37.Torregrossa L, Viola D, Sensi E, et al. (2016). Papillary Thyroid Carcinoma With Rare Exon 15 BRAF Mutation Has Indolent Behavior: A Single-Institution Experience. J Clin Endocrinol Metab. 101(11):4413-4420.

38. Xing M. (2005). BRAF mutation in thyroid cancer. Endocr Relat Cancer. 12(2):245-262.

39. Lee SR, Yim H, Han JH, et al. (2015). VE1 antibody is not highly specific for the BRAF V600E mutation in thyroid cytology categories with the exception of malignant cases. Am J Clin Pathol. 143(3):437-444.

40. Gertz RJ, Nikiforov Y, Rehrauer W, McDaniel L, Lloyd RV. (2016). Mutation in BRAF and Other Members of the MAPK Pathway in Papillary Thyroid Carcinoma in the Pediatric Population. Arch Pathol Lab Med. 140(2):134-139.

41. Xing M, Alzahrani AS, Carson KA, et al. (2015). Association between BRAF V600E mutation and recurrence of papillary thyroid cancer. J Clin Oncol. 33(1):42-50.

42. National Comprehensive Cancer Network. Thyroid Carcinoma (Version 2.2019). https://www.nccn.org/professionals/physician_gls/pdf/thyroid.pdf. Accessed September 25, 2019.

43. National Comprehensive Cancer Network. Non-Small Cell Lung Cancer (Version 7.2019). https://www.nccn.org/professionals/physician_gls/pdf/nscl.pdf. Accessed September 25, 2019.

44. Faehling M, Schwenk B, Kramberg S, et al. (2017). Oncogenic driver mutations, treatment, and EGFR-TKI resistance in a Caucasian population with non-small cell lung cancer: survival in clinical practice. Oncotarget. 8(44):77897-77914

45. Planchard D, Besse B, Groen HJM, et al. (2016). Dabrafenib plus trametinib in patients with previously treated BRAF(V600E)-mutant metastatic non-small cell lung cancer: an open-label, multicentre phase 2 trial. Lancet Oncol. 17(7):984-993.

46. Colombino M, Capone M, Lissia A, et al. (2012). BRAF/NRAS mutation frequencies among primary tumors and metastases in patients with melanoma. J Clin Oncol. 30(20):2522-2529.

47. National Comprehensive Cancer Network. Uveal Melanoma (Version 1.2019). https://www.nccn.org/professionals/physician_gls/pdf/uveal.pdf. Accessed September 25, 2019.

48. National Comprehensive Cancer Network. Cutaneous Melanoma (Version 2.2019). https://www.nccn.org/professionals/physician_gls/pdf/cutaneous_melanoma.pdf. Accessed September 25, 2019.

49. Long GV, Hauschild A, Santinami M, et al. (2017). Adjuvant Dabrafenib plus Trametinib in Stage III BRAF-Mutated Melanoma. N Engl J Med. 377(19):1813-1823.

50. Long GV, Eroglu Z, Infante J, et al. (2018). Long-Term Outcomes in Patients With BRAF V600-Mutant Metastatic Melanoma Who Received Dabrafenib Combined With Trametinib. J Clin Oncol. 36(7):667-673.

51. Sepulveda AR, Hamilton SR, Allegra CJ, et al. (2017). Molecular Biomarkers for the Evaluation of Colorectal Cancer: Guideline From the American Society for Clinical Pathology, College of American Pathologists, Association for Molecular Pathology, and the American Society of Clinical Oncology. J Clin Oncol. 35(13):1453-1486.

52. McHugh KE, Dermawan JK, Cheng YW, Cruise M, Sohal DPS, Reynolds JP. (2019). Molecular testing in metastatic colorectal adenocarcinoma cytology cell pellets. Diagn Cytopathol.

53.. National Comprehensive Cancer Network. Colon Cancer (Version 2.2019). https://www.nccn.org/professionals/physician_gls/pdf/colon.pdf. Accessed September 25, 2019.

54.. Sharma SG, Gulley ML. (2010). BRAF mutation testing in colorectal cancer. Arch Pathol Lab Med. 134(8):1225-1228.

55. Samowitz WS, Sweeney C, Herrick J, et al. (2005). Poor survival associated with the BRAF V600E mutation in microsatellite-stable colon cancers. Cancer Res. 65(14):6063-6069.

56. Wang, Y., Li, W., Phay, J., Shen, R., Pellegata, N., Saji, M., Ringel, M., de la Chapelle, A., He, H. (2016). Primary cell culture systems for human thyroid studies. Thyroid 26(8):1131-1140.

57. Brose, M.S., C.M. Nutting, B. Jarzab, R. Elisei, S. Siena, L. Bastholt, C. de la Fouchardiere, F. Pacini, R. Paschke, Y.K. Shong, S.I. Sherman, J.W. Smit, J. Chung, C. Kappeler, C. Pena, I. Molnar, M.J. Schlumberger. (2014).

Sorafenib in radioactive iodine-refractory, locally advanced or metastatic differentiated thyroid cancer: a randomised, double-blind, phase 3 trial. Lancet. 384:319-328.

58. Gharib, H. (2004). Changing trends in thyroid practice: understanding nodular thyroid disease. Endocr Pract. 10:31-39.

59. Schlumberger, M. (1999). Papillary and follicular thyroid carcinoma. N Engl J Med 338(5):297-306.

60. Grebe, S.K., and I.D. Hay. (1996). Thyroid cancer nodal metastases: biologic significance and therapeutic considerations. Surg Oncol Clin N Am. 5:43-63

61. Anderson, R.T., J.E. Linnehan, V. Tongbram, K. Keating, and L.J. Wirth. (2013). Clinical, safety, and economic evidence in radioactive iodine-refractory differentiated thyroid cancer: a systematic literature review. Thyroid. 23:392-407.

62. McCain, J. (2013). The MAPK (ERK) Pathway: Investigational Combinations for the Treatment Of BRAF-Mutated Metastatic Melanoma. P T. 38:96-108.

63.. Cabanillas, M.E., A. Patel, B.P. Danysh, R. Dadu, S. Kopetz, and G. Falchook. (2015). BRAF inhibitors: experience in thyroid cancer and general review of toxicity. Horm Cancer. 6:21-36.

64. Lito, P., N. Rosen, and D.B. Solit. (2013). Tumor adaptation and resistance to RAF inhibitors. Nat Med. 19:1401-1409

65. Vlachogiannis, G., S. Hedayat, A. Vatsiou, Y. Jamin, J. Fernandez-Mateos, K. Khan, A. Lampis, K. Eason, I. Huntingford, R. Burke, M. Rata, D.M. Koh, N. Tunariu, D. Collins, S. Hulkki-Wilson, C. Ragulan, I. Spiteri, S.Y. Moorcraft, I. Chau, S. Rao, D. Watkins, N. Fotiadis, M. Bali, M. Darvish-Damavandi, H. Lote, Z. Eltahir, E.C. Smyth, R. Begum, P.A. Clarke, J.C. Hahne, M. Dowsett, J. de Bono, P. Workman, A. Sadanandam, M. Fassan, O.J. Sansom, S. Eccles, N. Starling, C. Braconi, A. Sottoriva, S.P. Robinson, D. Cunningham, and N. Valeri. (2018). Patient-derived organoids model treatment response of metastatic gastrointestinal cancers. Science. 359:920-926.

66. Linder, S., and P. Kopp. (2005). Podosomes at a glance. J Cell Sci. 118:2079-2082.

67. Saito-Diaz, K., T.W. Chen, X. Wang, C.A. Thorne, H.A. Wallace, A. Page-McCaw, and E. Lee. (2013). The way Wnt works: components and mechanism. Growth Factors. 31:1-31.

68. Takebe, T., and J.M. Wells. (2019). Organoids by design. Science. 364:956-959

69. Xu, H., X. Lyu, M. Yi, W. Zhao, Y. Song, and K. Wu. (2018). Organoid technology and applications in cancer research. J Hematol Oncol. 11:116.

70. Lamouille, S., J. Xu, and R. Derynck. (2014). Molecular mechanisms of epithelial-mesenchymal transition. Nat Rev Mol Cell Biol. 15:178-196.

71. Ely, K., Bischoff, L., Weiss, V. (2018). Wnt signaling in thyroid homeostasis and carcinogenesis. Genes (Basel) 9(4):204.

72. Sastre-Perona, A., Riesco-Eizaguirre, G., Zaballos, M., Santisteban, P. (2016). B-catenin signaling is required for RAS-driven thyroid cancer through PI3K activation. Oncotarget 7(31):49435-49449.

73. Saito, Y., T. Muramatsu, Y. Kanai, H. Ojima, A. Sukeda, N. Hiraoka, E. Arai, Y. Sugiyama, J. Matsuzaki, R. Uchida, N. Yoshikawa, R. Furukawa, and H. Saito. (2019). Establishment of Patient-Derived Organoids and Drug Screening for Biliary Tract Carcinoma. Cell Rep. 27:1265-1276 e1264.

74. Liu, R., Xing, M. (2015). Diagnostic and prognostic TERT promoter mutations in thyroid fine-needle aspiration biopsy. Endocrine-Related Cancer 21(5):825-830.

75. Xing, M., Liu, R., Liu, X., Murugan, A., Zhu, G., Zeiger, M., Pai, S., Bishop, J. (2014). BRAF V600E and TERT promoter mutations cooperatively identify the most aggressive papillary thyroid cancer with highest recurrence. J Clin Oncol 32(25):2718-2726.

76. Rottner, K., J. Faix, S. Bogdan, S. Linder, and E. Kerkhoff. (2017). Actin assembly mechanisms at a glance. J Cell Sci. 130:3427-3435.

77. Liang, C.C., A.Y. Park, and J.L. Guan. (2007). In vitro scratch assay: a convenient and inexpensive method for analysis of cell migration in vitro. Nat Protoc. 2:329-333.

78. Nusse, R., and H. Clevers. (2017). Wnt/beta-Catenin Signaling, Disease, and Emerging Therapeutic Modalities. Cell. 169:985-999.

79. Clevers, H. (2016). Modeling Development and Disease with Organoids. Cell. 165:1586-1597.

80. Neal JT, Li X, Zhu J, et al. (2018). Organoid Modeling of the Tumor Immune Microenvironment. Cell 175: 1972-1988 e16.

81. Lieu D. (1997). Fine-needle aspiration: technique and smear preparation. Am Fam Physician 55: 839-46, 53-54.

82. Eddyani M, Fraga AG, Schmitt F, et al. (2009). Fine-needle aspiration, an efficient sampling technique for bacteriological diagnosis of nonulcerative Buruli ulcer. J Clin Microbiol 47: 1700-1704.

83. Baatenburg de Jong RJ, Rongen RJ, Verwoerd CD, van Overhagen H, Lameris JS, Knegt P. (1991). Ultrasound-guided fine-needle aspiration biopsy of neck nodes. Arch Otolaryngol Head Neck Surg 117: 402-404.

84. Jain D, Allen TC, Aisner DL, et al. (2018). Rapid On-Site Evaluation of Endobronchial Ultrasound-Guided Transbronchial Needle Aspirations for the Diagnosis of Lung Cancer: A Perspective From Members of the Pulmonary Pathology Society. Arch Pathol Lab Med 142: 253-262.

85. Pitman MB, Abele J, Ali SZ, et al. (2008). Techniques for thyroid FNA: a synopsis of the National Cancer Institute Thyroid Fine-Needle Aspiration State of the Science Conference. Diagn Cytopathol 36: 407-424.

86. Austin RM, Birdsong GG, Sidawy MK, Kaminsky DB. (2005). Fine needle aspiration is a feasible and accurate technique in the diagnosis of lymphoma. J Clin Oncol 23: 9029-9030; author reply 30-1.

87. Conrad R, Yang SE, Chang S, et al. (2018). Comparison of Cytopathologist-Performed Ultrasound-Guided Fine-Needle Aspiration With Cytopathologist-Performed Palpation-Guided Fine-Needle Aspiration: A Single Institutional Experience. Arch Pathol Lab Med 142: 1260-1267.

88. Mazzucchelli S, Piccotti F, Allevi R, et al. (2019). Establishment and Morphological Characterization of Patient-Derived Organoids from Breast Cancer. Biol Proced Online 21: 12.

89. Choi SI, Jeon AR, Kim MK, et al. (2019). Development of Patient-Derived Preclinical Platform for Metastatic Pancreatic Cancer: PDOX and a Subsequent Organoid Model System Using Percutaneous Biopsy Samples. Front Oncol 9: 875.

90. Tsai S, McOlash L, Palen K, et al. (2018). Development of primary human pancreatic cancer organoids, matched stromal and immune cells and 3D tumor microenvironment models. BMC Cancer 18: 335.

91. Tiriac H, Bucobo JC, Tzimas D, et al. (2018). Successful creation of pancreatic cancer organoids by means of EUS-guided fine-needle biopsy sampling for personalized cancer treatment. Gastrointest Endosc 87: 1474-1480.

92. Boj SF, Hwang CI, Baker LA, et al. (2015). Organoid models of human and mouse ductal pancreatic cancer. Cell 160: 324-338.

93. Tiriac H, Belleau P, Engle DD, et al. (2018). Organoid Profiling Identifies Common Responders to Chemotherapy in Pancreatic Cancer. Cancer Discov 8: 1112-1129

94. Goldhoff PE, Vohra P, Kolli KP, Ljung BM. (2019). Fine-Needle Aspiration Biopsy of Liver Lesions Yields Higher Tumor Fraction for Molecular Studies: A Direct Comparison With Concurrent Core Needle Biopsy. J Natl Compr Canc Netw 17: 1075-1081.

95. Boyd JD, Smith GD, Hong H, Mageau R, Juskevicius R. (2015). Fine-needle aspiration is superior to needle core biopsy as a sample acquisition method for flow cytometric analysis in suspected hematologic neoplasms. Cytometry B Clin Cytom 88: 64-68.

96. Siska PJ, Beckermann KE, Mason FM, et al. (2017). Mitochondrial dysregulation and glycolytic insufficiency functionally impair CD8 T cells infiltrating human renal cell carcinoma. JCI Insight 2(12):e93411.

97. Ernst LM, Rimm DL. (2002). Quantitative examination of mechanophysical tumor cell enrichment in fine-needle aspiration specimens. Cancer 96: 275-279.

98. Cajulis RS, Sneige N. (1993). Objective comparison of cellular yield in fine-needle biopsy of lymph nodes with and without aspiration. Diagn Cytopathol 9: 43-45.

99. Bar-Ephraim YE, Kretzschmar K, Clevers H. (2019). Organoids in immunological research. Nat Rev Immunol. 20(5):279-293.

100. Finnberg NK, Gokare P, Lev A, et al. (2017). Application of 3D tumoroid systems to define immune and cytotoxic therapeutic responses based on tumoroid and tissue slice culture molecular signatures. Oncotarget 8: 66747-66757.

101. Jenkins RW, Aref AR, Lizotte PH, et al. (2018). Ex Vivo Profiling of PD-1 Blockade Using Organotypic Tumor Spheroids. Cancer Discov 8: 196-215.

102. Chakrabarti J, Holokai L, Syu L, et al. (2018). Mouse-Derived Gastric Organoid and Immune Cell Co-culture for the Study of the Tumor Microenvironment. Methods Mol Biol 1817: 157-168.

103. Dijkstra KK, Cattaneo CM, Weeber F, et al. (2018). Generation of Tumor-Reactive T Cells by Co-culture of Peripheral Blood Lymphocytes and Tumor Organoids. Cell 174: 1586-1598 e12.

104. Schnalzger TE, de Groot MH, Zhang C, et al. (2019). 3D model for CAR-mediated cytotoxicity using patient-derived colorectal cancer organoids. EMBO J 38.

105. Seino T, Kawasaki S, Shimokawa M, et al. Human Pancreatic Tumor Organoids Reveal Loss of Stem Cell Niche Factor Dependence during Disease Progression. Cell Stem Cell 2018: 22: 454-467 e6.

106. Long GV, Stroyakovskiy D, Gogas H, et al. (2014). Combined BRAF and MEK inhibition versus BRAF inhibition alone in melanoma. N Engl J Med 371: 1877-1888.

107. Vilgelm, A., Bergdorf, K., Wolf, M., Bharti, V., Shattuck-Brandt, R., Blevins, A., Jones, C., Phifer, C., Lee, M., Lowe, C., Hongo, R., Boyd, K., Netterville, J., Rohde, S., Idrees, K., Bauer, J., Westover, D., Reinfeld, B., Baregamian, N., Richmond, A., Rathmell, WK., Lee, E., McDonald, O., and Weiss, V. (2020). Fine-needle aspiration-based patient-derived cancer organoids. iScience 23(8):101408.

108. Ordóñez, N. (2013). Broad-spectrum immunohistochemical epithelial markers: a review. Human Pathology 44(7):1195-1215.

109. Pradniwat, K., Treetipsatit, J. (2013). A practical approach to undifferentiated tumors: a review on helpful markers and common pitfalls. Asian Archives of Pathology 9(4):123-136.

110. Kodack, D., Farago., Dastur, A., Held, M., Dardaei, L., et al. (2017). Primary patient-derived cancer cells and their potential for personalized cancer patient care. Cell Reports (21)11:3298-3309.

111.. Tamas, E.F. and Epstein J.I. (2007) Detection of residual tumor cells in bladder biopsy specimens: pitfalls in the interpretation of cytokeratin stains. Am J Surg Pathol (31)3:390-397.

112. Matsubayashi, S., Kawai, K., Matsumoto, Y., et al. (1995). The correlation between papillary thyroid carcinoma and lymphocytic infiltration in the thyroid gland. J Clin Endocrinol Metab, 80**,** 3421-3424.

113. Lundgren, C., Hall, P., Dickman, P, Zedenius, J. (2006). Clinically significant prognostic factors for differentiated thyroid carcinoma: a population-based, nested case-control study. Cancer, 106**,** 524-531.

114. French, J., Weber, Z., Fretwell, D., et al. (2010). Tumor-associated lymphocytes and increased FoxP3+ regulatory T cell frequency correlate with more aggressive papillary thyroid cancer. J Clin Endocrinol Metab, 95**,** 2325-2333.

115. Cuhna, L., Morari, E., Guihen, A., et al. (2012). Infiltration of a mixture of immune cells may be related to good prognosis in patients with differentiated thyroid carcinoma. Clin Endocrinol (Oxf), 77**,** 918-925.

116. Galdiero, M., Varricchi, G., Marone, G. (2016). The immune network in thyroid cancer. Oncoimmunology, 5**,** e1168556.

117. Yu, H., Huang, X., Liu, X., et al. (2013). Regulatory T cells and plasmacytoid dendritic cells contribute to the immune escape of papillary thyroid cancer coexisting with multinodular non-toxic goiter. Endocrine, 44**,** 172-181.

118. Uglioni, C., Elisei, R., Proietti, A., et al. (2014). FoxP3 expression in papillary thyroid carcinoma: a possible resistance biomarker to iodine 131 treatment. Thyroid, 24**,** 339-346.

119. Tsuge, K., Takeda, H., Kawada, S., et al. (2005). Characterization of dendritic cells in differentiated thyroid cancer. J Pathol, 205**,** 565-576.

120. Kim, B. (2013). The expression of tumor-associated macrophages in papillary thyroid carcinoma. Endocrinol Metab (Seoul), 28**,** 178-179.

121. Fang, W., Ye, L., Shen, L, et al. (2014). Tumor-associated macrophages promote the metastatic potential of thyroid papillary cancer by releasing CXCL8. Carcinogenesis, 35**,** 1780-1787.

122. Jung, K., Cho, S., Kim, Y., et al. (2015). Cancers with Higher Density of Tumor-Associated Macrophages Were Associated with Poor Survival Rates. J Pathol Transl Med, 49**,** 318-324.

123. Hiramatsu, S., Tanaka, H., Nicshimura, J., et al.. (2018). Neutrophils in primary gastric tumors are correlated with neutrophil infiltration in tumor-draining lymph nodes and the systemic inflammatory response. BMC Immunol, 19**,** 13.

124. Soler-Cardona, A., Forsthuber, A., Lipp, K., et al. (2018). CXCL5 Facilitates Melanoma Cell-Neutrophil Interaction and Lymph Node Metastasis. J Invest Dermatol, 138**,** 1627-1635.

125. Wculek, S., and Malanchi, I. (2015). Neutrophils support lung colonization of metastasis-initiating breast cancer cells. Nature, 528**,** 413-417.

126. Na, K., and Choi, H. (2018). Immune landscape of papillary thyroid cancer and immunotherapeutic implications. Endocr Relat Cancer, 25**,** 523-531

127. Kim, K., Jeon, S., Kim, T., & Jung, C. K. (2018). Immune Gene Signature Delineates a Subclass of Papillary Thyroid Cancer with Unfavorable Clinical Outcomes. Cancers (Basel), 10.

128. Newman, A., Liu, C., Green, M., Gentles, A., Feng, W., Xu, Y., Hoang, C., Diehn, M., Alizadeh, A. (2015). Robust enumeration of cell subsets from tissue expression profiles. Nat Methods, 12**,** 453-457.

129. Li, B., Severson, E., Pignon, J et al. (2016). Comprehensive analyses of tumor immunity: implications for cancer immunotherapy. Genome Biol, 17**,** 174.

130. Li, T., Fan, J., Wang, G, et al. (2017). TIMER: A Web Server for Comprehensive Analysis of Tumor-Infiltrating Immune Cells. Cancer Res, 77**,** e108-e110

131. Jiang, P., Gu, S., Pan, D. et al. (2018). Signatures of T cell dysfunction and exclusion predict cancer immunotherapy response. Nat Med, 24**,** 1550-1558.

132. Nikiforov, Y., Seethala, R., Tallini, G. et al. (2016). Nomenclature Revision for Encapsulated Follicular Variant of Papillary Thyroid Carcinoma: A Paradigm Shift to Reduce Overtreatment of Indolent Tumors. JAMA Oncol, 2**,** 1023-1029.

133. Ryder, M., Vhosserin, R., Ricarte-Filho, J. et al. (2008). Increased density of tumor-associated macrophages is associated with decreased survival in advanced thyroid cancer. Endocr Relat Cancer, 15**,** 1069-1074.

134. Qing, W., Fang, W., Ye, L., et al. (2012). Density of tumor-associated macrophages correlates with lymph node metastasis in papillary thyroid carcinoma. Thyroid, 22**,** 905-910.

135. Chiu, C., Strugnell, S., Griffith, O., et al. (2010). Diagnostic utility of galectin-3 in thyroid cancer. Am J Pathol, 176**,** 2067-2081.

136. Kouo, T., Huang, L., Pucsek, A, et al. (2015). Galectin-3 Shapes Antitumor Immune Responses by Suppressing CD8+ T Cells via LAG-3 and Inhibiting Expansion of Plasmacytoid Dendritic Cells. Cancer Immunol Res, 3**,** 412-423.

137. Tang, Z., Li, C., Kang, B., et al.. (2017). GEPIA: a web server for cancer and normal gene expression profiling and interactive analyses. Nucleic Acids Res, 45**,** W98-W102.

138. Galdiero, M., Varricchi, G., Lofredo, S., et al.. (2018). Potential involvement of neutrophils in human thyroid cancer. PLoS One, 13**,** e0199740.

139. Coffelt, S., Kersten, K., Boornebal, C, et al. (2015). IL-17-producing gammadelta T cells and neutrophils conspire to promote breast cancer metastasis. Nature, 522**,** 345-348.

140. Reilleux, I., Blay, J., Bendriss-Vermare, N., et al. (2004). Dendritic cell infiltration and prognosis of early stage breast cancer. Clin Cancer Res, 10**,** 7466-7474.

141. Curiel, T., Cheng P., Mottram, P., et al. (2004). Dendritic cell subsets differentially regulate angiogenesis in human ovarian cancer. Cancer Res, 64**,** 5535-5538.

142. Gu-Trantien, C., and Willard-Gallo, K. (2013). Tumor-infiltrating follicular helper T cells: The new kids on the block. Oncoimmunology, 2**,** e26066.

143. Vinuesa, C., and Cyster, J. (2011). How T cells earn the follicular rite of passage. Immunity, 35**,** 671-680.

144. Mcheyzer-Willaims, M., Okitsu, S., Wang, N., Mcheyzer-Williiams, L. (2011). Molecular programming of B cell memory. Nat Rev Immunol, 12**,** 24-34.

145. Dieu-Nosjean, M., Giraldo, N., Kaplon, H. et al. (2016). Tertiary lymphoid structures, drivers of the anti-tumor responses in human cancers. Immunol Rev, 271**,** 260-275.

146. Gu-Trantien, C., Loi, S., Garaud, S. et al. (2013). CD4(+) follicular helper T cell infiltration predicts breast cancer survival. J Clin Invest, 123**,** 2873-2892.

147. Bense, R., Sotiriou, C., Piccart-Gebhart , et al..(2017). Relevance of Tumor-Infiltrating Immune Cell Composition and Functionality for Disease Outcome in Breast Cancer. J Natl Cancer Inst, 109.

148. Ali, H., Chlon, L., Pharoah, P., et al. (2016). Patterns of Immune Infiltration in Breast Cancer and Their Clinical Implications: A Gene-Expression-Based Retrospective Study. PLoS Med, 13**,** e1002194.

149. Gordon-Alonso, M., Hirsch, T., Wildmann, C, and van der Bruggen, P. (2017). Galectin-3 captures interferon-gamma in the tumor matrix reducing chemokine gradient production and T-cell tumor infiltration. Nat Commun, 8**,** 793.

150. Karanikas, V., Speletas, M., Zamanakou, M., et al. (2008). Foxp3 expression in human cancer cells. J Transl Med, 6**,** 19.

151. Amin, M., Greene, F., Edge, S., et al. (2017). The Eighth Edition AJCC Cancer Staging Manual: Continuing to build a bridge from a population-based to a more "personalized" approach to cancer staging. CA Cancer J Clin 67:93-99.

152. Li, M., Datto, M., Duncavage, E., et al. (2017). 2017 Standards and Guidelines for the Interpretation and Reporting of Sequence Variants in Cancer: A Joint Consensus Recommendation of the Association for Molecular Pathology, American Society of Clinical Oncology, and College of American Pathologists. J Mol Diagn 19:4-23.

153. Dobin, A., Davis, C., Schlesinger, F., et al. (2013). STAR: ultrafast universal RNA-seq aligner. Bioinformatics 29(1):15-21.

154. Liao, Y., Smyth, G., Shi, W. (2014). featureCounts: an efficient general purpose program for assigning sequence reads to genomic features. Bioinformatics 30(7):923-930.

155. Subramanian, A., Tamayo, P., Mootha, V., et al. (2005). Gene set enrichment analysis: a knowledge-based approach for interpreting genome-wide expression profiles. Proc Natl Acad Sci 102(43):15545-15550.

156. Garcia-Rostan, G., Camp, R.L., Herrero, A., et al.(2001). Beta-catenin dysregulation in thyroid neoplasms: down-regulation, aberrant nuclear expression, and CTNNB1 exon 3 mutations are markers for aggressive tumor phenotypes and poor prognosis. Am J Pathol 158: 987-996.

157. Garcia-Rostan G., Tallini G., Herrero A., et al. (1999). Frequent mutation and nuclear localization of beta-catenin in anaplastic thyroid carcinoma. Cancer Res. 59, 1811–1815.

158. Kurihara, T., Ikeda, S., Ishizaki, Y., et al. (2004). Immunohistochemical and sequencing analyses of the Wnt signaling components in Japanese anaplastic thyroid cancers. Thyroid 14: 1020-1029.

159. Hunt JL, Tometsko M, LiVolsi VA, et al. (2003). Molecular evidence of anaplastic transformation in coexisting well-differentiated and anaplastic carcinomas of the thyroid. Am J Surg Pathol 27:1559–1564.

160. Smallridge, R., Marlow, L., Copland, J. (2008). Anaplastic thyroid cancer: molecular pathogenesis and emerging therapies. Endocr Relat Cancer 16(1): 17-44.

161. Lin, B., Ma, H., Ma, M., Zhang, Z., Sun, Z., Hsieh, I., Okenwa, O., Guan, H., Le, J., Lv, W. (2019). The incidence and survival analysis for anaplastic thyroid cancer: a SEER database analysis. Am J Transl Res 11(9): 5888-5896.

162. Maniakas, A., Dadu, R., Busaidy, N., Wang, J., Ferrarotto, R,. Lu, C., Williams, M., Gunn, G., Hofmann, M., Cote, G., Sperling, J., Gross, N., Sturgis, E., Goepfert, R., Lai, S., Cabanillas, M., Zafereo, M., (2020). Evaluation of overall survival in patients with anaplastic thyroid carcinoma, 2000-2019. JAMA Oncol 6(9): 1397-1404.

163. Chaicharoenaudomrung, N., Kunhorm, P., Noisa, P. (2019). Three-dimensional cell culture systems as an in vitro platform for cancer and stem cell modeling. World J Stem Cells 11(12):1065-1083.

164. Cirello, V., Vaira, V., Grassi, E., Vezzoli, V., Ricca, D., Colombo, C., Bosari, S., Vicentini, L., Persani, L., Ferrero, S., Fugazzola, L. (2017). Multicellular spheroids from normal and neoplastic thyroid tissues as a suitable model to test the effects of multikinase inhibitors. Oncotarget 8(6): 9752-9766.

165. Lagies, S., Schlimpert, M., Neumann, S., Waldin, A., Kammerer, B., Borner, C., Peintner, L. (2020). Cells grown in three-dimensional spheroids mirror in vivo metabolic response of epithelial cells. Comms Bio (2020)3:246.

166. Meyer, C., Wooten, D., Paudel, B., Bauer, J., Hardeman, K., Westover, D., Lovly, C., Harris, L., Tyson, D., Quaranta, V. (2019). Quantifying drug combination synergy along potency and efficacy axes. Cell Syst 8(2):97-108.e16139.

167. Lubbock, A., Harris, L., Quaranta, V., Tyson, D., Lopez, C. (2021). Thunor: visualization and analysis of high-throughput dose-response datasets. Nucleic Acids Res 49(W1): W633-W640.

168. Landa, I., Pozdeyev, N., Korch, C., Marlow, L., Smallridge, R., Copland, J., Henderson, Y., Lai, S., Clayman, G., Onoda, N., Tan, A., Garcin-Rendueles, M., Knauf, J., Haugen, B., Fagin, J., Schweppe, R. (2019). Comprehensive genetic characterization of human thyroid cancer cell lines: A validated panel for preclinical studies. Clin Canc Res 25(10): 3141-3151.

169. Marlow, L., D'Innocenze, J., Zhang, Y., Rohl, S., Cooper, S., Sebo, T., Grant, C., McIver, B., Kasperbauer, J., Wadsworth, J., Cas-let, J., Kennedy, P., Highsmith, W., Clark, O., Milosevic, D., Netzel, B., Cradic, K., Arora, S., Beaudry, C., Grebe, S., Silverberg, M., Azorsa, D., Smallridge, R., Copland, J. (2010). Detailed molecular fingerprinting of four new anaplastic thyroid carci-noma cell lines and their use for verification of RhoB as a molecular therapeutic target. J Clin Endocrinol Metab 95(12):5338-5347.

170. Adams, J. (2012). The Valley of Death in anticancer drug development: a re-assessment. Trends Pharmacol Sci 33(4):173-180.

171. Kola, I., Landis, J. (2004) Can the pharmaceutical industry reduce attrition rates? Nat Rev Drug Discov 3:711-716.

172. Moreno, L., Pearson, A. (2013). How can attrition rates be reduced in cancer drug discovery? Expert Opin Drug Discov 8(4):363-368.

173. Liu, R., Xiao, Z., Xu, H., Long, Z., Wei, F., Zhuang, S., Sun, X., Xie, L., Mu, J., Yang, A., Zhang, G., Fan, Y. (2016). Treatment and prognosis of anaplastic thyroid carcinoma; A clinical study of 50 cases. PLoS One 11(10): e0164840.

174. Wendler, J., Kroiss, M., Gast, K., Kreissi, M., Allelein, S., Lichtenauer, U., Blaser, R., Spitzweg, C., Fassnacht, M., Schott, M., Fuhrer, D., Tiedje, V. (2016). Clinical presentation, treatment and outcome of anaplastic thyroid carcinoma: results of a multicenter study in Germany. Euro J Endocrinol 175(6):521-529.

175. Adams, J., Palombella, V., Sausville, E., Johnson, J., Destree, A., Lazarus, D., Maas, J., Pien, C., Prakash, S., Elliott, P. (1999). Proteasome inhibitors: a novel class of potent and effective antitumor agents. Cancer Res 59(1):2615-2622.

176. Adams, J. (2003). The proteasome: structure, function, and role in the cell. Canc Treatment Rev 29(S1):3-9.

177. Tan, C., Abdul-Majeed, S., Cael, B., Barta, S. (2019). Clinical pharmacokinetics and pharmacodynamics of bortezomib. Clin Pharmacokinetics 58:157-168.

178. Scott, K., Hayden, P., Will, A., Wheatley, K., Coyne, I. (2016). Bortezomib for the treatment of multiple myeloma. Cochrane Database Syst Rev 4:CD010816.

179. Moreau, P., Pylypenko, H., Grosicki, S., Karamanesht, I., Leleu, X., Grishunina, M., Rekhyman, G., Masliak, Z., Robak, T, Shubina, A., Arnulf, B., Kropff, M., Cavet, J., Esseltine, D., Feng, H, Girgis, S., ven de Velde, H, Deraedt, W., Harousseau, J. (2011). Subcutaneous verses intravenous administration of bortezomib in patients with relapsed multiple myeloma: a randomized, phase 3, non-inferiority study. Lancet Oncol 12(5):431-440.

180. Tsumagari, K., Elmageed, Z., Sholl, A., Green, E., Sobti, S., Khan, A., Kandil, A., Murad, F., Friedlander, P., Boulares, A., Kandil, E. (2018). Bortezomib sensitizes thyroid cancer to BRAF inhibitor in vitro and in vivo. Endocrine-Related Canc 25:99-109.

181. Mitsiades, C., McMillin, D., Kotoula, V., Poulaki, V., McMullan, C., Negri, J., Fanourakis, G., Tseleni-Balafouta, S., Ain, K., Mitsiades, N. (2006). Antitumor effects of the proteasome inhibitor bortezomib in medullary and anaplastic thyroid carcinoma cells in vitro. J Clin Endocrinol Metab 91(10):4013-4021.

182. Altmann, A., Markert, A., Askoxylakis, V., Schoning, T., Jesenofsky, R., Eisenhut, M., Haberkorn, U. (2012). Antitumor effects of proteasome inhibition in anaplastic thyroid carcinoma. J Nucl Med 53(11):1764-1771.

183. Nachalon, Y., Stern-Shavit, S., Bachar, G., Shvero, J., Limon, D., Popovtzer, A. (2015). Aggressive palliation and survival in anaplastic thyroid carcinoma. JAMA Otolaryngol Head Neck Surg 141(12):1128-1132.

184. Abate, E., Smallridge, R. (2014). Managing anaplastic thyroid carcinoma. Exp Rev Endocrinol 6(6):793-809.

185. Duran, G., Derdau, V., Weitz, D., Phillippe, N., Blankenstein, J., Atzrodt, J., Semiond, D., Gianolio, D., Mace, S., Sikic, B. (2018). Cabazitaxel is more active than first-generation taxanes in ABCB1(+) cell lines due to its reduced affinity for P-glycoprotein. Canc Chemother Pharmacol 81(6):1095-1103.

186. Sugawara, I., Masunaga, A., Itoyama, S., Sumizawa, T., Akiyama, S., Yamashita, T. (1995). Expression of multidrug resistance-associated protein (MRP) in thyroid cancers. Cancer Lett 95(1-2):135-138.

187. Sternberg, C., Castellano, D., de Bono, J., Fizazi, K., Tombal, B., Wulfing, C., Kramer, G., Eymard, J., Bamias, A., Carles, J., Iacovelli, R., Melichar, B., Sverrisdottir, A., Theodore, C., Feyerabend, S., Helissey, C., Poole, E., Ozatilgan, A., Geffriaud-Ricouard, C., de Wit, R. (2021). Efficacy and safety of cabazitaxel versus abiraterone or enzalutamide in older patients with metastatic castration-resistant prostate cancer in the CARD study. Eur Urol 80(4):497-506.

188. Koutras, A., Zagouri, F., Koliou, G., Psoma, E., Chryssogonidis, I., Lazaridis, G., Tryfonopoulos, D., Kotsakis, A., Res, E., Kentepozidis, N., Razis, E., Psyrri, A., Koumakis, G., Kalofonos, H., Dimopoulos, M., Fountzilas, G. (2020). Phase 2 study of cabazitaxel as second-line treatment in patients with HER2-negative metastatic breast cancer previously treated with taxanes-a Hellenic Cooperative Oncology Group (HeCOG) trial. Br J Canc 123:355-361.

189. Nakahara, T., Takeuchi, M., Kinoyama, I., Minematsu, T., Shirasuna, K., Matsuhisa, A., Kita, A., Tominaga, F., Yamanaka, K., Kudoh, M., Sasamata, M. (2007). YM155, a novel small-molecular survivin suppressant, induces regression of established human hormone-refractory prostate tumor xenografts. Canc Res 67(17):8014-8021.

190. Waligorska-Stachura, J., Sawicka-Gutaj, N., Zabel, M., Andresiewicz, M., Gut, P., Czarnywojtek, A., Ruchala, M. (2017). Survivin DEx3 as a biomarker of thyroid cancers: A study at the mRNA and protein level. Oncol Lett 13(4):2437-2441.

191. Pannone, G., Santoro, A., Pasquali, D., Zamparese, R., Mattoni, M., Russo, G., Landrischina, M., Piscazzi, A., Toti, P., Cignarelli, M., Muzio, L., Bufo, P. (2014). The role of survivin in thyroid tumors: differences of expression in well-differentiated, non-well-differentiated, and anaplastic thyroid cancers. Thyroid 24(3):511-519.

192. Mehta, A., Zhang, L., Boufraqech, M., Liu-Chittenden, Y., Zhang, Y., Patel, D., Davis, S., Rosenberg, A., Ylaya, K., Aufforth, R., Li, Z., Shen, M., Kebebew, E. Inhibition of survivin with YM155 induces durable tumor response in anaplastic thyroid cancer. Clin Canc Res 21(18):4123-4132.

193. Xu, Q., Mackay, R., Xiao, A., Copland, J., Weinberger, P. (2021). YM155 induces oxidative stress-mediated DNA damage and cell cycle arrest, and causes programmed cell death in anaplastic thyroid cancer cells. Int J Mol Sci 22(4):1961.

194. Thorne, C., Hanson, A., Schneider, J., et al. (2010). Small-molecule inhibition of Wnt signaling through activation of casein kinase 1α. Nature Chemical Biology, 6(11), 829-836.